The Phloem Sieve Tube as a Dynamic Carrier of Water and Sugars

by

Ryan Stanfield

A thesis submitted in partial fulfillment of the requirements for the degree of

Doctor of Philosophy

in

Forest Biology and Management

Department of Renewable Resources
University of Alberta

ABSTRACT

This dissertation delves into the anatomy and physiology of the phloem plant vascular tissue. Two primary topics are investigated in this thesis: (1) The cellular localization and response of aquaporin protein water channels in phloem sieve tubes and (2) the mathematical modeling of phloem sieve plates and radial water flows on the hydraulic resistance and pressure profiles of sieve tubes in balsam poplar (*Populus balsamifera* L.).

In the first study, I use immunohistochemistry experiments to identify the distribution and cellular location of aquaporins in the phloem within different organs of the poplar tree. I found that throughout the entire transport pathway from source to sink, sieve tube plasma membranes contain two subfamilies of aquaporin proteins. The first type, PIP1, facilitates the transport of water and some uncharged molecules through the plasma membrane. The second type, PIP2, is the primary water carrying channel in plants. I found that PIP1 aquaporins are mostly found within internal cellular compartments of the sieve tube. This contrasts with PIP2 aquaporins which were found mostly in the plasma membrane. The second study followed the results of the first and looked at how the application of a cold block affected the expression of selected PIP1 and PIP2 genes in phloem tissue. It was found that cold block application transiently increased the abundance of PIP2 aquaporins in the plasma membrane of sieve tubes and altered the abundance of aquaporin mRNA transcript. Overall, aquaporins in sieve tubes may be an important regulator in supporting long distance sugar transport due to turgor pressure maintenance, especially in trees. The third study was a computational model assessing the impact of sieve plate pores as well as radial flows on the resistance of fluid flow through sieve tubes. It was found that non-circular pores add significant resistance to the sieve tube conduit, and that radial water flows may ease some of the resistance encountered due to sieve plates.

PREFACE

This thesis is an original work by Ryan Stanfield.

Chapter 2 of this thesis has been published as R. C. Stanfield, U.G. Hacke and J. Laur, "Are phloem sieve tubes leaky conduits supported by numerous aquaporins?" American Journal of Botany, vol. 104, 719-732. I equally shared contribution towards this manuscript with U.G. Hacke for the design, literature review, writing and planning of this work. J. Laur performed the Western Blot analysis. I performed all other experiments.

Chapter 3 of this thesis was by R. C. Stanfield, U.G. Hacke and J. Laur "Aquaporins Respond to Chilling in the Phloem by Increased Protein Abundance and Altered mRNA expression". I designed the experiment, performed the literature review and wrote the chapter. J. Laur performed the qrtPCR analysis. I performed all other experiments.

Chapter 4 of this thesis has been published as R.C. Stanfield, P. J. Schulte, K.E. Randolph and U.G. Hacke "Computational models evaluating the impact of sieve plates and radial water exchange on phloem pressure gradients." Plant, Cell and Environment. I shared equally the planning, literature review and writing with U.G. Hacke. P.J. Schulte did the computional modeling work and wrote significant portions of the manuscript. K.E. Randolph contributed sieve plate callose blockage models. I obtained all the images used for mathematical modeling.

Chapter 5 of this thesis has been submitted as a book chapter in Methods in Phloem Research as R.C. Stanfield and A. Schulz "Super-Resolution Microscopy of Phloem Proteins". I performed the experiments and troubleshooting to write the protocol. A. Schulz wrote the introduction. I collected the images.

“There's another disadvantage to the use of the flashlight: like many other mechanical gadgets it tends to separate a man from the world around him. If I switch it on my eyes adapt to it and I can see only the small pool of light it makes in front of me; I am isolated. Leaving the flashlight in my pocket where it belongs, I remain a part of the environment I walk through and my vision though limited has no sharp or definite boundary.”

— Edward Abbey

ACKNOWLEDGEMENTS

I would like to thank my supervisor Dr. Uwe Hacke for all the help given to me throughout the duration of my thesis. Through your guidance, I have significantly developed as a researcher over the past four years and owe a lot of my success to your dedication in mentoring the work that has gone into this dissertation. I will always have gratitude and respect for the work we did together.

I thank the members of my supervisory committee, Dr. Barb Thomas and Dr. Enrico Scarpella who helped with obtaining balsam poplar cuttings and imaging techniques on the confocal microscope, respectively. Thank you to Robert Turgeon and Janusz Zwiazek for being thesis committee examiners.

I have many people to thank that made this research possible. Thank you to Dr. Joan Laur for being my #1 tech support person for all my aquaporin labeling experiments (and failures). Thanks to Dr. Paul Schulte for the extremely valuable contribution towards the sieve plate modeling study, as well as all the great hospitality shown when I visited UNLV. Thanks to Arlene Oatway for the valuable tips and conversations in the microscopy lab. Thank you to Kelley Dunfield for making my T.A. appointments a whole lot of fun. Thank you to my lab mates Rachel Hillabrand, Jaime Azcona, Cayla Brocious, and Lauren Sinclair for helping to get through the tough times and celebrating during the best times.

TABLE OF CONTENTS

LIST OF TABLES

Chapter 2

Chapter 3

Chapter 4

LIST OF FIGURES

Chapter 1

Chapter 2

Chapter 3

Chapter 4

Chapter 5

I. General introduction and literature review

1. Phloem structure and function

a. Anatomy and cell biology

The vascular system of plants is composed of two major tissue types: xylem and phloem. Whereas xylem transports water from the roots to leaves, phloem transports sugars from where they are produced to where they are needed. Generally, it is believed that transport follows a concentration gradient of sugars (Milburn 1974). For example, sugars produced via photosynthesis in leaf tissue will enter the phloem and be transported long distance to a growing flower, fruit, or root tissue. Unlike the xylem vascular tissue, the cellular conduits through which photosynthates move are living, and typically require energy inputs to propagate sugars over a long distance (van Bel 2003).

The cell types of the phloem in angiosperms are parenchyma, phloem fibers, sieve elements (SE), and companion cells (CC). In conifers, the phloem is comprised of the sieve cells and albuminous or Strasburger cells (Esau 1939). The sieve elements are joined together by porous sieve plates to form the continuous sieve tube. These sieve tubes then act as the conduits by which sugars and other molecules are transported long distance. Since the sieve tube's primary role is for the long-distance transport of photosynthetic products and other macromolecules, its cytoplasmic interior is mostly empty of typical cellular contents. A mature sieve element will lack a nucleus, vacuole and ribosomes common in other plant cells (van Bel 2003; Fig. 1-1). Since the sieve element lacks these basic organelles, it is kept alive by neighboring companion cells, which form close physical links with the sieve elements. This allows the companion cells to deliver sugar for transport, as well as proteins and other essential molecules needed for sieve element function (van Bel & Knoblauch 2000).

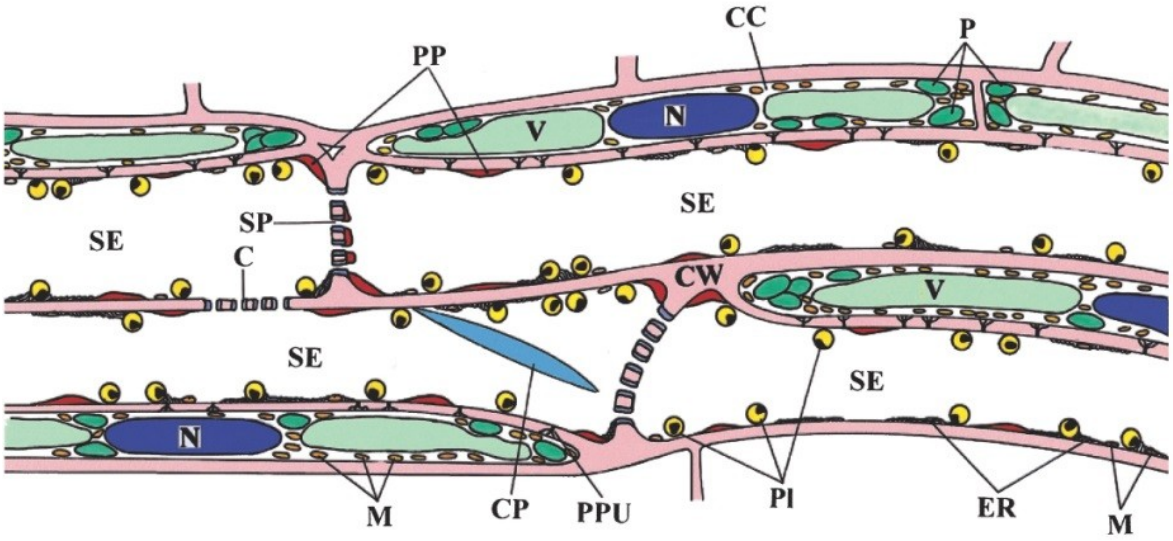

Figure 1-1: Sieve tube element (SE) and companion cells (CC) are in close association with each other. PPU = plasmodesmata pore unit, PP = parietal protein, SP = sieve plate, C = callose, V = vacuole, N = nucleus, CW = cell wall, M = mitochondria, CP = crystalline protein structure, PI = sieve element plastid, P = plastid (from Van Bel 2003).

The symplastic connection (i.e. cytoplasm sharing) between the sieve element and companion cell is made via plasmodesmata which are small openings in the cell wall (Esau 1939). These nanoscale passageways are lined continuously with the plasma membrane, and endoplasmic reticulum (ER) has been visualized to span their distance linking companion cell to sieve element (Fitzgibbon et al. 2010). Also associated with phloem tissue are parenchyma cells that may or may not be directly connected with the symplast of neighboring companion cells and are also metabolically active in support of companion cells or sieve elements (Zhang et al. 2014, Cayla et al. 2015).

Developmentally, phloem arises from meristematic tissue called the procambium or vascular cambium within vascular tissues (Esau 1939). These cambium types will also give rise to the xylem vascular tissue. The procambium divides to produce new phloem cells within minor veins of leaves or within a central vascular cylinder or stele within fine roots. For organs that grow in girth via secondary growth, secondary phloem arises from the vascular cambium. The sieve tube and companion cell derive from the same mother cell early in their development.

The connectivity between the sugar producing leaf mesophyll cell and the companion cell/sieve element complex varies from species to species (Schulz 2015, Rennie & Turgeon 2009). In some plant groups (such as *Populus* Sp. and *Cucurbita* Sp.), there is a direct symplastic connection between mesophyll cells all the way to the companion cell/sieve element complex (Russin & Evert 1985, Turgeon & Helper 1989). In other species (ex: *Vicia faba* and *Nicotiana tabacum*), symplastic connectivity may span from the mesophyll cell but end at the bundle sheath (Liesche & Schulz 2012). For these species, sugars would have to move into the apoplast before entering a vein and eventually into the phloem. Overall, it has been shown that the interconnection of cells of the pre-phloem pathway via plasmodesmata vary by taxonomic

class and likely determine the way each plant handles how it delivers sugar from the mesophyll to the phloem (Gamalei 1991). In any of these systems, the plasmodesmata pathway may become closed (Turgeon and Helper 1989) due to callose blockage or adjustment of channel size via protein modifications and/or cytoskeletal elements (Maul, Benitez-Alfonso and Faulkner 2011; van Bel 2019). Alternatively, roots have their own unique connectivity of symplastic connections used for unloading, and have recently been documented with funnel shaped plasmodesmata connections between protophloem and pericycle cells in *Arabidopsis* (Ross-Elliott et al. 2017).

b. Movement of sap through the phloem and the cycling of water

The currently accepted mechanism by which sugar or other solutes move through the phloem has been theoretically described by Münch (1930). The route which sugars take to get to the phloem is outside of the Münch pressure flow hypothesis but is described in detail in recent work (Rennie & Turgeon 2009, Rockwell, Gersony & Holbrook 2018, Liesche & Schulz 2012, Schulz 2015). Once sugars make it inside the sieve element/companion cell complex, the pressure flow mechanism begins (Fig. 1-2). The high concentration of sugars inside the phloem conduit drive the movement of water in via osmosis past the semi-permeable plasma membrane. This influx of water elevates the pressure inside the conduit. Now under high pressure, the sugars contained at the starting sieve element are then pushed along through other sieve elements within the sieve tube. At the end of the pathway (e.g. in roots), where turgor pressure and sugar concentration are reduced, water exits the sieve tube. Thus, according to the pressure flow hypothesis, it is the difference in pressure between the source and sink ends of the conduit which drives sugar movement. Note that the experimental apparatus created by Münch was outside the framework of living tissue and is therefore simplified. However, the most recent experimental evidence still

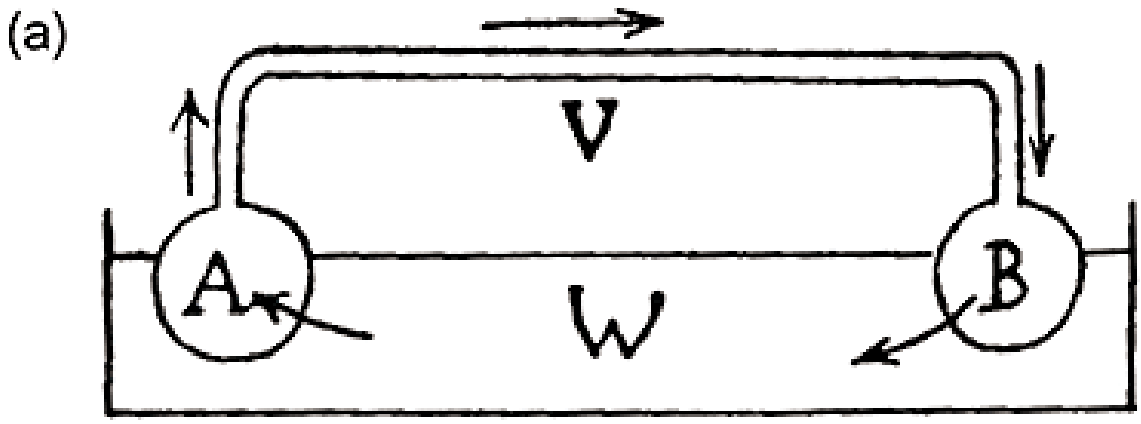

Figure 1-2: The original model of phloem transport as experimentally recreated by Münch (1927). In this diagram, two regions representing a source (A) and sink (B) are submerged in a water bath (W). The source and sink region are bound by a semipermeable membrane. Solutes in the source drive the movement of water from the surrounding bath into (A). This increases the pressure in this container and drives the solution in the direction of the arrows, through the transport conduit (V). Once at the sink (B), the remaining pressure in the vessel is adequate to drive the water back into the water bath through the semipermeable membrane. Image from E. Münch (1927) as shown in Knoblauch & Peters (2010).

points to these pressure gradients as the main driving force behind phloem translocation (Savage et al. 2017, Knoblauch et al. 2016).

Outside of the sieve tube water circulates between the xylem and phloem. The xylem carries water from the roots towards the leaves, using the cohesion of water molecules linked together (Dixon 1914). The xylem sap solution fed from the root organs is delivered to the shoot system, pulled by a gradient of water potential created between the moist soil and dry atmosphere. Once reaching the end of the xylem conduit in the leaves, the water and solubilized soil nutrients can then nourish mesophyll tissue needed in photosynthesis, or simply evaporate from leaves. At this point the third option for water is to be delivered to the phloem tissue, via the process of osmosis. The fate of where water ends up is dictated by the water potential gradient.

Water potential ($\Psi_{w;}$ in units Mega Pascal- MPa) is the potential energy of water to move through a direction in space (Kramer & Boyer 1995). The equation that governs water potential is as follows:

$$\Psi_W = \Psi_s + \Psi_p + \Psi_m + \Psi_g \quad \text{(Eqn 1-1)},$$

where Ψ_s is the solute potential, Ψ_p is the pressure potential, Ψ_m is the matric potential and Ψ_g is the gravitational potential. In the context of a cell, if the water potential inside the cell is more negative than outside the cell, water will enter the cell. As the number of solutes increase inside a cell, the solute potential decreases and is a negative value (anything except pure water is less than 0). Matric potentials are often associated with the particles in the soil and will be omitted from our current discussion on the phloem. Pressure potential is applied via water entering/exiting cells and can either cause a pushing (positive value in the case of phloem) or a

sucking (negative value in the case of xylem) force. Gravitational potential exerts itself on a column of fluid and is reported as a positive value; this value may be significant for phloem transport in trees > 1m in height. Since phloem transport in growing trees is usually from top to bottom, phloem flow will be facilitated by gravity.

The cycling of water from the xylem and phloem thus follows a water potential gradient (Fig. 1-3). At source tissue with high levels of sugars inside the phloem, the solute potential makes the sieve tube conduit have an overall more negative water potential than the xylem. This in turn causes water to enter the phloem. At a sink site, sugar has been released from the sieve tube throughout the pathway, decreasing its final solute potential while simultaneously reducing its pressure potential. The negative water potential of the xylem at this location causes water to leave the phloem and enter back into the xylem.

Due to the difficulty in measuring phloem transport directly, plant biologists often model sap flow using mathematical equations. To assess the amount of fluid that can be moved per unit time, a *volume flow* measurement can be taken. There are many ways in which volume flow can be measured, such as hydraulic conductance, conductivity and specific conductivity (Tyree & Ewers 1991). For example, a common unit for conductivity is mmol s^{-1} MPa^{-1} m^{-1} (Sperry et al. 1998). Alternatively, fluid movement can also be described in terms of *velocity* which is how quickly a particle can move through a conduit and can be expressed as units such as mm s^{-1}. One technique used for solving volume flow through a pipe (like phloem or xylem) is by using Poiseuille's Law. Although several assumptions are made, such as cylindrical tubes and sealed side walls (Phillips & Dungan 1993), this Law is often used as a way to approximate volume flow through a sieve tube system (Mullendore et al. 2010, Savage et al. 2017).

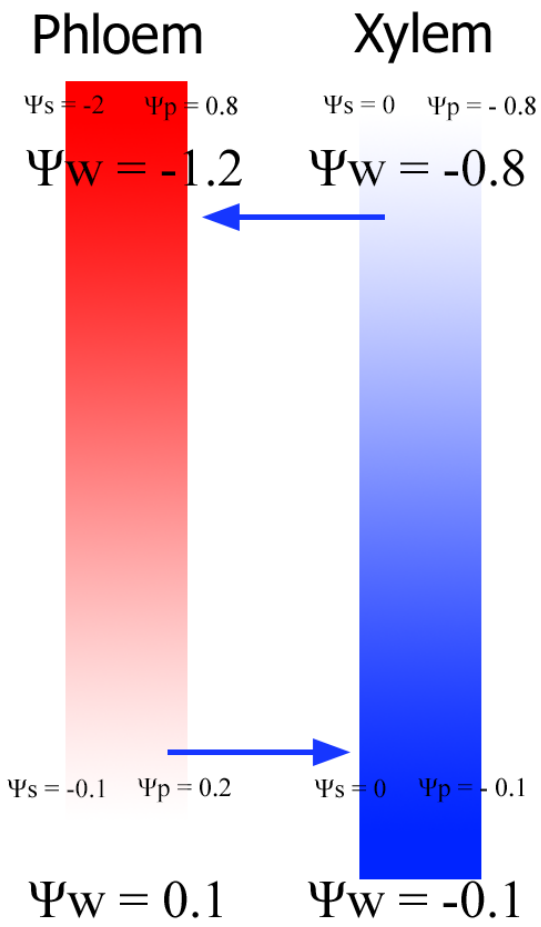

Figure 1-3: A diagram showing how water movement between the phloem and xylem follows a water potential gradient. Starting from the top (source region), the solute potential in the phloem is -2 while the pressure potential is 0.8, equaling to an overall water potential of -1.2. In the xylem the solute potential is 0 while the pressure potential is -0.8, making the overall water potential -0.8. Water at the top will thus favor going to the more negative water potential in the phloem. At the bottom of the graphic (sink region), the solute potential in the phloem is -0.1 while the pressure potential is 0.2, making for a total water potential of 0.1. For the xylem, the solute potential is 0 while the pressure potential is -0.1, making for a total water potential of -0.1. This will favor water to move from the phloem tissue to the xylem. Symbols: Ψw = water potential, Ψs = solute potential, Ψp = pressure potential. All units are in Megapascals (MPa). Note that the values used in this figure are not representative of what might be experienced *in vivo* and are purely for the sake of discussion. Figure loosely based from Nobel (2009), Fig. 9-18.

When looking at individual phloem sieve tube elements, the volume flow of phloem sap can be modeled using the Poeseuille's Law equation (Mullendore et al. 2010):

$V = \frac{\pi \Delta p r^4}{8 \eta l}$, (Eqn 1-2)

where r is the radius of the sieve tube, Δp is pressure difference between the start and end of the tube, η is the viscosity of the phloem sap and l is the length of the tube. When looking at *velocity*, or simply, the speed at which a solute particle in the sap can move, it can be described by:

$(2)\ U = \frac{k \Delta p}{\eta l}$, (Eqn 1-3)

where *k* is the specific conductivity. Therefore, an increase in radius should theoretically increase both volume flow and velocity of the phloem sap substantially. This relationship between the radius of the tube and flow has been used to describe how the tapering of conduit diameter allows flow to continue despite drops in pressure gradients experienced in a tall tree (Savage et al. 2017).

c. The analysis and complications associated with sampling phloem sap

The mathematical modeling of fluid movement through the sieve tube conduit depending upon structural features is a practical way to validate the Münch hypothesis. However, obtaining experimental validation using *in vivo* measurements has been extremely difficult. Since the phloem is a living tissue, a cellular response will be made to any damage done from sectioning or probing, which makes minimizing the invasiveness of collecting data on phloem sap critical (Windt et al. 2006). Although velocity can be measured using imaging techniques, measuring phloem pressure directly requires the invasive use of probes. Since validating the pressure driven

flow hypothesis of Münch (1930) is one of the central questions to phloem biologists at present (Turgeon 2010), these pressure gradients must be tested directly.

Many methods have been tested to non-invasively track the movement of phloem sap (Truernit 2014). Pulse labeling can be used whereby radioactive CO_2 isotopes (using Carbon 11) are exposed to leaves, then the plant is radio-autographed at different time points to track the progress of the carbon isotope; another non-invasive measurement strategy is the use of Positron Emission Tomography, although the resolution is still constrained to a few millimeters. The major issue with using these isotope tracers is that only the radioactive particle is being tracked, which may possess a different flow rate than other molecules in the highly viscous phloem sap (Windt et al. 2006). Unlike the first two methods which require application of a radioactive tracer, Nuclear Magnetic Resonance (NMR) flow imaging does not require the introduction of exogenous radioactive particles, making it suitable for long duration measurements. Perhaps the most practical method of tracing phloem flow is the use of fluorescent labels that can be viewed in living tissue using confocal microscopy, although this technique can only view tissue that is relatively thin (developing roots of *Arabidopsis*, for instance). This method exposes leaf tissue to dyes, which are then photo-bleached and detected by camera to measure velocity (e.g. Jensen et al. 2011). However, this method still requires scoring the leaf to introduce the dye, so the potential still exists for downstream damage responses. Last, microfluidic bio-mimicking devices that recreate the properties of sieve elements can be used to verify the results of photo-bleaching techniques, although the micro-capillaries used are simplistic compared to the actual biological system (Comtet et al. 2017).

To gain a more direct measure of the pressure of phloem sap or to analyze sap contents, the sieve element must be punctured. One method uses aphid stylets to penetrate the sieve

element, after which a pressure probe is attached that applies a positive pressure until that sap movement stops from the stylet (Gould, Minchin & Thorpe 2004). A pressure transducer attached to the probe measures the amount of pressure that needs to be applied for the flow to stop. The obtained pressure value can then be applied to the Poiseuille equation (eqn 1-2) to estimate flow (as performed in Knoblauch et al. 2016). However, this method could be erroneous since it encourages build-up of callose on sieve pores and around the entry point of the stylet due to the perturbation of the cytoplasm. This method may also cause the sieve tube to express defensive compounds creating callose reactions on sieve plates (Moran et al. 2002). In theory, pressure probe analysis using glass micro-capillary tubes could be a valuable alternative to using aphid probes and has been used previously to measure turgor pressure in the sieve element (Tomos & Leigh 1999, Knoblauch et al. 2016). One disadvantages of using this method is that it is technically very challenging to perform. In addition, although the capillaries can have a similar diameter as aphid stylets (~10μm), they differ in that aphids can sense a route through intercellular spaces to avoid excessive damage to non-sieve element cells (Tjallingii & Hogen Esch 1993).

2. Aquaporins

a. Aquaporin structure and function

Aquaporins are intrinsic membrane proteins primarily responsible for the facilitated delivery of water across the plasma membrane or tonoplast. They have been described to occur in many branches of life, including bacteria, animals and plants (Maurel et al. 2008). Since their discovery in plants (Maurel et al. 1993, Kammerloher et al. 1994), a wide range of other functions have been demonstrated such as the passive transport of solutes such as urea, boric

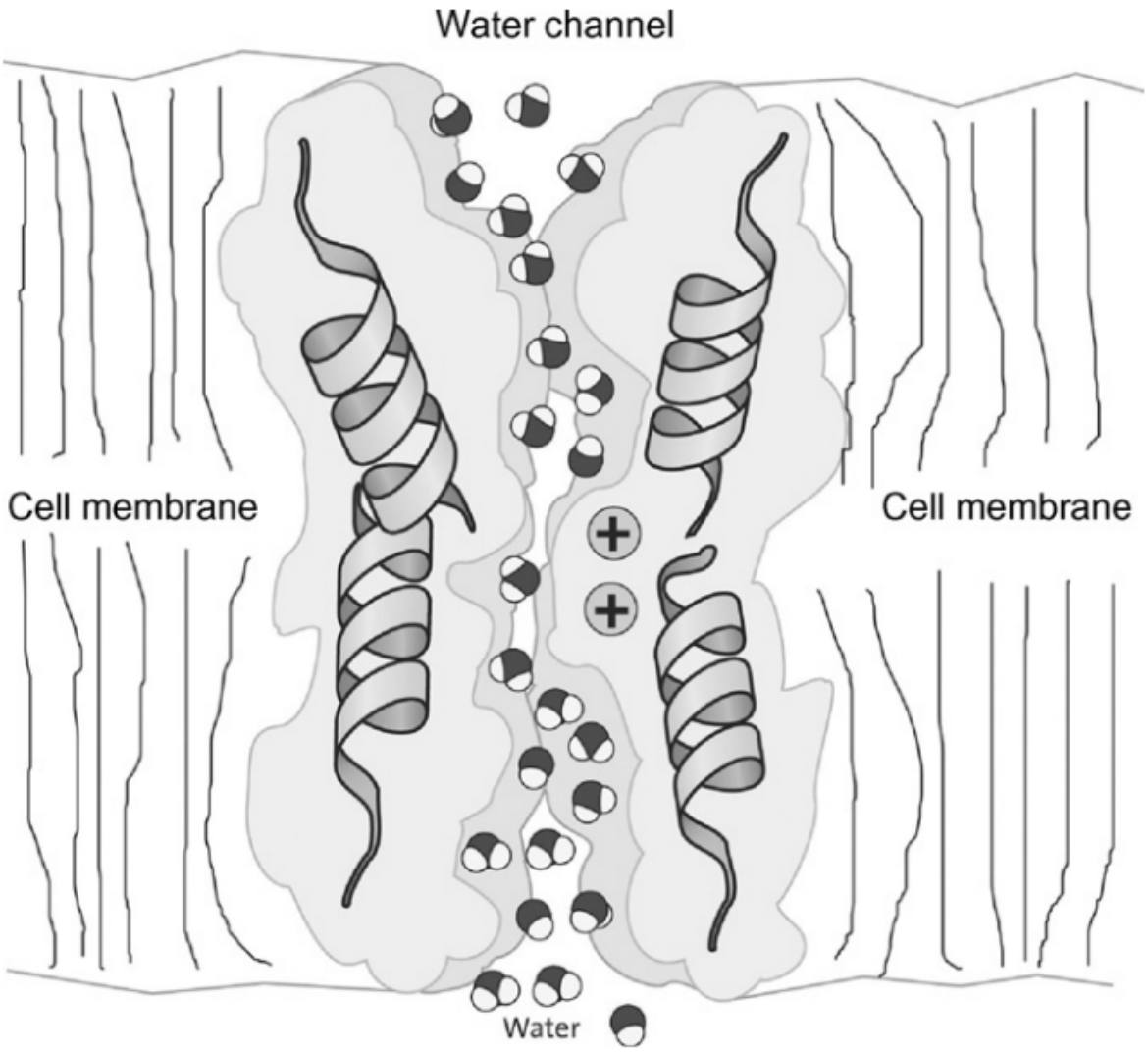

Figure 1-4: Diagram of an aquaporin water channel embedded into a cell membrane. The centrally located channel in the aquaporin subunit is specifically designed to allow water molecules to pass through. A three-sequence conserved amino acid structure (asparagine–proline–alanine) is included in the central pore region of the aquaporin. This sequence contains a constriction point which forces water molecules into a single file line, and through electrostatic changes, flips each water molecule in the correct orientation for it to pass through this gap. Image from Zhao et al. (2008).

acid, and silicic acid (Maurel et al. 2008). In addition, gases such as CO_2 (Mori et al. 2014, Uehlein et al. 2008), ammonia or oxygen (Zwiazek et al. 2017) may also pass through these channels. However, their most noted role is in the delivery of water which significantly aides in hydraulic functionality of the plant body.

Aquaporins have an interesting array of structural characteristics which facilitate their functionality. Structurally, a completed aquaporin unit is assembled in a quaternary protein folding arrangement. In the case of a completed aquaporin unit, this means four individual protein subunits are joined together (Chaumont & Tyerman 2014). Each subunit of aquaporin contains a pore by which water may pass (Zhao, Shao & Chu 2008, Fig. 1-4). Each channel has a conserved region which is just big enough for a water molecule to pass through. The asparagine–proline–alanine amino acid sequence makes up this central pore region. Another specialized region called the aromatic/Arginine (a/R region) constricts the passage of water molecules into a single file line. Electrostatic charges at this point then flip the polar water molecules on their side which allows them to fit through the pore. X-ray crystallography images reveal the pore structure to be 2 Angstroms for a closed configuration and up to 3.9 Angstroms in diameter in its open configuration (Fischer et al. 2009, Törnroth-Horsefield et al. 2006). In comparison, the full diameter of the water molecule is about 2.75 Angstroms, making clear why this molecular flip is needed.

Apart from a conserved aquaporin pore region, the protein has evolved over the eons into a variety of subfamilies in plants. A high diversity of these water carrying proteins exists in the different branches of life. Aquaporins are a subclass of the Major Intrinsic Protein (MIPs) family of integral proteins which are found in all classifications of life (Maurel et al. 2008). The MIP

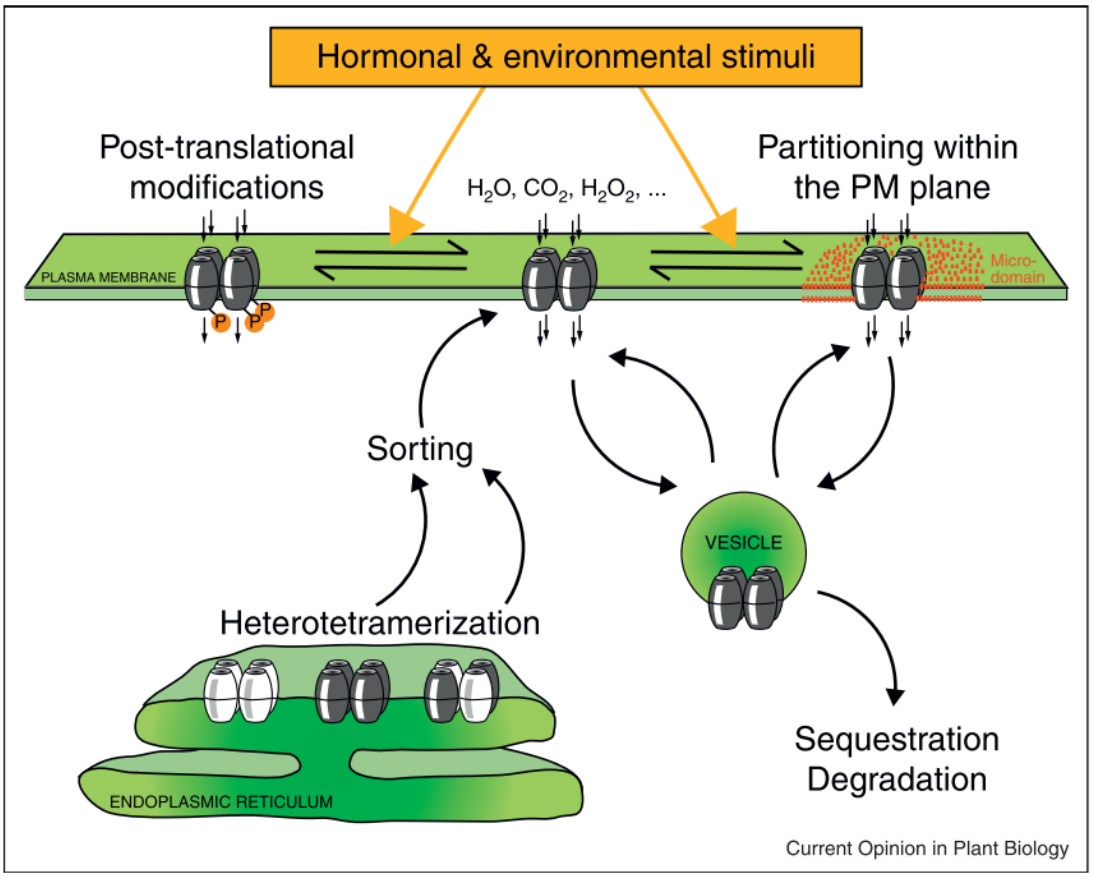

Figure 1-5: Schematic of post-translational modification, heterotetramerization, and cycling of aquaporins to and from the plasma membrane. In response to environmental stimuli aquaporin protein expression can be heavily modified at the cellular level. Aquaporin units in the plasma membrane may be opened via phosphorylation or closed via dephosphorylation (post-translational modification). In addition, aquaporins may move in location along the plasma membrane in response to stress or bud off into a vesicle to be degraded in a lysosome. Finally, aquaporin heterotetramers can have an assortment of protein subfamily combinations to adjust the functionality of the aquaporin unit. This sorting is done in the endoplasmic reticulum (ER). For example, combinations of PIP1 (white) or PIP2 (grey) subunits will be arranged in the ER for eventual export to the plasma membrane. Schematic shown from Verdoucq et al. (2014).

channel is broad in category and includes membrane channel proteins that carry many molecules besides water. In plants, aquaporin proteins can be divided into four major families including, (1) Plasma membrane Intrinsic Proteins (PIPs), Tonoplast Intrinsic Proteins (TIPs), Nodulin-26-like Intrinsic Proteins (NIPs) and Small basic Intrinsic Proteins (SIPs). Each species of plant contains different numbers of isoforms, or subgroups within each family of aquaporin. For example, in *Populus trichocarpa*, 15 PIPs, 17 TIPS, 11 NIPs and 6 SIPs isomers have been identified (Almedia-Rodriguez et al. 2010, Gupta & Sankararamakrishnan 2009). For the purposes of this discussion, concentration will be focused on the PIPs since they are the main water channels used in plant cells.

The functionality of aquaporins can be heavily regulated based upon their interactions with other aquaporin isoforms, bindings with regulatory molecules, and cycling to and from the membrane (Maurel et al. 2015, Verdoucq et al. 2014, Fig. 1-5). Individual aquaporin molecules can either bind identical subunits to form homotetramers or use a combination of unidentical subunits to form a heterotetramer. This process of hetero- or homo- tetramerization occurs in the ER (Verdoucq et al. 2014). For example, 2 PIP1 protein subunits can combine with 2 PIP2 subunits to form a heterotetramer. This ability to shuffle these aquaporin isoforms modulates their ability to transport water across the cell membrane. Thus, when particular subgroups of PIP2 are expressed in conjunction with particular PIP1 subgroups as a heterotetramer, the water transport ability may increase more than if PIP2 was expressed as a homotetramer (Fetter et al. 2004). This may be due in part, to the reliance of PIP2 on PIP1 to shuttle to the plasma membrane. Another feature of aquaporins that modulates their water transport capacity is their ability to be gated via their interaction with other molecules (post-translational modification) (Verdoucq et al. 2014). When a specific amino acid residue is phosphorylated, this opens the

water channel (Törnroth-Horsefield et al. 2006). Conversely, if the channel is protonated, the pore is closed. Finally, aquaporins may be shuttled in and out of the membrane to modulate the overall ability of the cell to transport water. In response to stressful conditions, aquaporins may bud away from the plasma membrane to form endosomes, and subsequently be destroyed in lytic vesicles (Maurel et al. 2015).

b. Aquaporin response to environmental stress

Increasingly it is becoming clear that aquaporins play a large role in controlling the movement of water throughout the entire plant body (Maurel et al. 2008). This is due to the scenario in which water cannot move apoplastically between cells, and instead must transverse the plasma membrane. For example, in roots, a suberized casparian strip located in the cell wall of endodermal cells forces water entry through the plasma membrane. An abundance of aquaporins have been isolated here which strengthens the role of the endodermis in water uptake and in regulating water flow into the root vascular cylinder (Maurel et al. 2008). Once inside the vascular system, aquaporins have been documented generally in the vascular tissue (Maurel et al. 2002), and on through to leaf bundle sheath cells (Sade et al. 2014) and guard cells (Maurel, Verdoucq & Rodrigues 2016).

Aquaporins respond throughout the whole plant to environmental disturbances such as root salinity, drought stress and nutrient deprivation (Maurel et al. 2008). In response to nutrient stress, aquaporins may be downregulated to prevent water loss in times where soil nutrients would disallow efficient plant growth. Likewise, roots will respond to drought through the downregulation of their aquaporins (Maurel et al. 2015, Laur & Hacke 2013) to prevent water from leaving the root into the surrounding dry soil. Aquaporins have also been shown to be important drivers of the reduction of root cell hydraulic conductivity upon salt stress (Lee &

Zwiazek 2015) as well as cold (Lee et al. 2012); overexpressing aquaporin genes in mutant *Arabidopsis* plants helped to ameliorate reduced hydraulic conductivity due to these stresses. This shows that aquaporins act to buffer against temporary disturbances to whole plant hydraulics in drought conditions.

At the cellular level, aquaporins respond to challenging conditions in numerous ways. In roots of *Arabidopsis*, salt stress induced the formation of aquaporins to bud into vesicles and relocate into intracellular compartments (Boursiac et al. 2005). Concomitantly in the same species, protein abundance of aquaporins declines in the plasma membrane of root cortical cells following salt treatment (Verdoucq et al. 2014). Aquaporins that are sent away from the plasma membrane may be temporarily relocated into the tonoplast or be destroyed in a lytic vesicle (Luu & Maurel 2005).

3. Characteristics of study species: balsam poplar

The focal species of this study was balsam poplar, *Populus balsamifera* L. of the willow family (Salicaceae). Etymologically, the genus *Populus* is derived from the Romans, which translates to "tree of the people" as they often would plant these species along major boulevards (Peterson & Peterson 1992). The species was chosen for the following reasons: 1) balsam poplar is a close relative of the model tree species, cottonwood (*Populus trichocarpa)*, 2) the species is easy to propagate clones via cuttings, 3) investigating the phloem in a tree species is less common than in herbs, thus giving poplar an edge when it comes to tackling research questions and 4) this species is readily abundant in the province of Alberta, and occurs close to where the research was conducted in the River Valley of Edmonton adjacent to the University of Alberta.

The geographic range of balsam poplar spans across much of Canada and also some areas of the United States (Peterson & Peterson 1992). In terms of overall geography, they tend to occur in the cooler regions of the continental boreal forest and avoid the warmer maritime climes (on the West Coast). In particular, balsam poplar occurs in (from West to East): Alaska, Yukon Territories, British Colombia, Northwest Territories, Alberta, Saskatchewan, Manitoba, Ontario, Quebec, New Brunswick, Nova Scotia, Newfoundland and Labrador as well as the Northern States of New England. Within Alberta, species have been recorded to grow to a mean height of 13.5 m, with a maximum height of 23.2 m (Peterson & Peterson 1992). Economically balsams (and other poplars) are important, especially for their relatively small crown area which limits the debranching operation required of foresters prior to harvest. In addition, poplars are quick growing for a tree species due to their high photosynthetic output. However, pure balsam poplars are typically not selected for their wood products due to the resins produced in their buds and wood, and instead are chosen to hybridize with other poplars to improve their growth rate (Larchevêque et al. 2011).

Although balsam poplar can reproduce via seed, like aspen, they are known to propagate clonally via root suckers. Therefore, balsam poplars in close proximity of one another may be clones spawned from lateral root runners, which sporadically send up aerial shoots to produce new trunks. Interestingly, poplars are diecious and occur as male or female plants, the latter of which have been documented to reproduce clonally at a greater rate (Peterson & Peterson 1992).

The balsam poplar is shade intolerant and an inhabitant of upland sites as well as river adjacent bottomland and alluvial plains (Peterson & Peterson 1992). In terms of preferred soil, they thrive in loamy, well drained and deep soils. Among boreal dwelling species, balsam poplar is known to be one of the most tolerant to flooding, making their occupation of riverbanks

common. The species is considered rather drought intolerant, and its stomatal behavior considered to be anisohydric; this means that under drought conditions, the stomatal pores of the leaf will remain open to maintain high gas exchange rates (Larchevêque et al. 2011). This higher gas exchange rate may come at the cost of potentially being more vulnerable to drought induced mortality, if the drought in question is severe enough (McDowell et al. 2008).

4. Summary

The phloem is the vascular tissue responsible for the translocation of sugars and signaling molecules throughout the plant body. Anatomically the heart of the phloem consists of the companion cell - sieve element complex. The companion cell provides essential services to the adjoined sieve element via specialized plasmodesmata connections. Lacking many of the organelles of a typical living plant cell, the sieve element has a mostly open cytoplasm that is used to transport sugar over long distances. Joined at their end walls via a sieve plate, sieve elements join to form a long and continuous sieve tube to deliver sugars from source to sink.

In terms of mechanism of action, the Münch (1930) hypothesis is the best supported idea of how sugars translocate through sieve tubes. Briefly, sugars are loaded into the sieve tube which decreases solute potential locally. Water then flows into the tube via osmosis which increases the pressure. This pressure is then used to push sugars along to areas of the plant in need of sucrose for metabolism and growth. At the sugar exit point, water will leave and recirculate back into the xylem. Although the Münch hypothesis is the most accepted view of how sugars are transported, validating it experimentally remains exceedingly difficult. Probing the phloem to indicate source – sink pressure gradients is work that is difficult to perform, although it has been assessed recently in a vine species (Knoblauch et al. 2016) and a tree species (Savage et al. 2017). These works have validated the source – sink pressure gradients predicted

to occur in the Münch pressure – flow hypothesis, however the magnitude of the gradients is the opposite of what was expected between vine and tree species. Pressure gradients in the tree were lower than in the vine. Looking back to eqn (1-2), volume flow increases with additional source-sink pressure differential. This raises the question of how trees support efficient long-distance flow while maintaining a low-pressure gradient? To assess how this could be, mathematical modeling can be used as an important tool to assess if the pressure flow hypothesis is feasible in tall trees, and if the mechanism can be applied equally to a variety of species.

Aquaporin protein water channels are ubiquitous throughout the three domains of life and provide important physiological roles for maintaining cell water balance. Water moves through tiny channels within the center of the protein, and in addition, other molecules such as CO_2 and O_2 may also enter through the central pore of the aquaporin unit. In response to environmental stress such as drought, aquaporins can be regulated in numerous ways. Through post-translational modification, aquaporins can close through such mechanisms as dephosphorylation. They can also be removed from membranes entirely through endocytosis, to be stored in the endoplasmic reticulum or simply destroyed. All these regulatory mechanisms impact the ability of the cell and containing tissue to transport water over long distance through organs.

5. Research Objectives

As outlined above, the mechanism of how the phloem translocates sugar was hypothesized over 85 years ago by Münch (1930). However the hypothesis needs to be tested further within the plant and especially in trees, as it has been questioned if the pressures generated via osmosis is enough to drive transport over very long distances (Turgeon 2010). Testing to see if the necessary pressure gradients exist at all are a difficult undertaking that requires sophisticated equipment (e.g. Knoblauch et al. 2016, Savage et al. 2017) or the patient use of aphids to probe

the phloem (e.g. Gould, Minchin & Thorpe 2004). In any event, the physiological paradigm that has been set since the time of Münch has been to focus attention at the loading portion of phloem at source tissue (e.g., leaf tissue) or unloading of phloem at sink tissue (e.g., roots). This is to determine if the underlying pressure difference between the two regions is adequate to provide the driving force for sugar movement. However, the intervening pathway between source and sink, the transport phloem, has often been understudied due to the difficulty in reaching this tissue. In fact, even Münch's original diagram (Fig. 1-2) shows the transport pathway raised above water level, suggesting that this portion of the transport pathway is physiologically isolated from the surrounding tissue. At the time, Münch could not have known the functionality and control aquaporins gave to plant membranes. With the likely occurrence of aquaporins in the phloem (van Bel 2003, Thompson 2006), it can now be hypothesized that the sieve tube supports a dynamic regulation of water exchange from the entire pathway from source to sink. This ability to continually exchange water with surrounding tissue has been hypothesized, but not confirmed, to play a crucial role in maintaining the long-distance transport of sugars in sieve tubes.

To date, there has only been one study to systemically define the *cellular* location of aquaporins in sieve tubes. Fraysse et al. (2005) documented PIP1 aquaporins at the cellular level in the sieve tubes of spinach leaves, petioles and roots (but see Laur and Hacke 2014, Almeida and Hacke 2012 for phloem general labeling). Although this study did point out the novelty of aquaporins in sieve tubes, the link between aquaporins and long distance translocation in sieve tubes was not made. In addition, no study has systemically looked at the aquaporins found in the phloem of trees. This is despite one of the biggest questions in phloem transport biology is how trees are able to transport sap in the phloem over distances greater than 100 meters (Ryan & Asao 2014).

Thus, one objective of this thesis is documenting the presence of aquaporin water channels in the phloem of balsam poplar using immunolabeling techniques (**Chapter 2**). This includes documenting which cell types of the phloem have aquaporins, as well as their cellular location. The next objective (**Chapter 3**) is determining if an environmental disturbance causes changes to the aquaporins of sieve tubes. This will be tested by subjecting a portion of transport phloem located in the stem to a chilling event provided by a cold block. An interesting legacy of tests over the past 100 years have shown the temporary halt of phloem transport due to chilling (e.g. Geiger & Sovonick 1975, Minchin & Thorpe 1983, Lang & Minchin 1986, Gould, Minchin & Thorpe 2004), yet the mechanism of its action remains elusive. Thus, the secondary objective of this chapter is to investigate if aquaporins are responsible for this rapid response to chilling. Finally, (**Chapter 4**) looks at a major structural unit of the sieve tube, the sieve plate. The sieve plate was viewed to possess a variety of interesting characteristics that could alter flow: sieve pores that may become blocked, and that occur in various shapes and sizes as well as plates that occur at different angles. Using the Comsol modeling software, it was determined how these different plate characteristics impact the resistivity of the sieve tube to try and answer the question: how much does varying sieve plate traits impact flow? Also integrated in this model are the impacts of radial water flows on axial transport, which ties in the ideas of Chapters 2 and 3 concerning aquaporins. The last chapter (**Chapter 5**) is a methods chapter documenting the technique of using super resolution microscopy (3D-SIM) to view phloem tagged with antibodies in unprecedented detail. Super resolution microscopy allows for twice the resolution over standard confocal microscopy, which combined with immunolabeling will allow future researchers to uncover new subcellular features of the phloem.

6. References

Almeida-Rodriguez A. M., Cooke, J. E., Yeh, F., & Zwiazek, J. J. (2010). Functional characterization of drought-responsive aquaporins in *Populus balsamifera* and *Populus simonii*× *balsamifera* clones with different drought resistance strategies. *Physiologia Plantarum 140*, 321-333.

Almeida-Rodriguez A. M., & Hacke, U. G. (2012). Cellular localization of aquaporin mRNA in hybrid poplar stems. *American Journal of Botany 99*, 1249-1254.

Boursiac Y., Chen S., Luu D., Sorieul M., van den Dries N. & Maurel C. (2005) Early effects of salinity on water transport in arabidopsis roots. molecular and cellular features of aquaporin expression. *Plant Physiology* 139, 790-805.

Cayla T., Batailler B., Le Hir R., Revers F., Anstead J.A., Thompson G.A., Grandjean O. & Dinant S. (2015) Live imaging of companion cells and sieve elements in arabidopsis leaves. *PloS One 10*, e0118122.

Chaumont F. & Tyerman S.D. (2014) Aquaporins: Highly regulated channels controlling plant water relations. *Plant Physiology 164,* 1600-1618.

Comtet J., Jensen K.H., Turgeon R., Stroock A.D. & Hosoi A.E. (2017) Passive phloem loading and long-distance transport in a synthetic tree-on-a-chip. *Nature plants 3*, 17032

Dixon H.H. (1914) Transpiration and the ascent of sap in plants. *In: plants*. Macmillan and Company, limited.

Esau K. (1939) Development and structure of the phloem tissue. *Botanical Review* 5, 373-432.

Fetter K., Van Wilder V., Moshelion M. & Chaumont F. (2004) Interactions between plasma membrane aquaporins modulate their water channel activity. *The Plant Cell 16*, 215-228.

Fischer G., Kosinska-Eriksson U., Aponte-Santamaría C., Palmgren M., Geijer C., Hedfalk K., Hohmann S., De Groot B.L., Neutze R. & Lindkvist-Petersson K. (2009) Crystal structure of a yeast aquaporin at 1.15 Å reveals a novel gating mechanism. *PLoS Biology 7*, e1000130.

Fitzgibbon J., Bell K., King E. & Oparka K. (2010) Super-resolution imaging of plasmodesmata using three-dimensional structured illumination microscopy. *Plant Physiology 153*, 1453-1463.

Fraysse L.C., Wells B., McCann M.C. & Kjellbom P. (2005) Specific plasma membrane aquaporins of the PIP1 subfamily are expressed in sieve elements and guard cells. *Biology of the Cell 97*, 519-534.

Gamalei Y. (1991) Phloem loading and its development related to plant evolution from trees to herbs. *Trees 5,* 50-64.

Geiger D.R. & Sovonick S.A. (1975) Effects of temperature, anoxia and other metabolic inhibitors on translocation. In: *Transport in Plants 1,* pp- 256-286.

Gould N., Minchin P.E.H. & Thorpe M.R. (2004) Direct measurements of sieve element hydrostatic pressure reveal strong regulation after pathway blockage. *Functional Plant Biology 31*, 987-993.

Gupta A.B. & Sankararamakrishnan R. (2009) Genome-wide analysis of major intrinsic proteins in the tree plant populus trichocarpa: Characterization of XIP subfamily of aquaporins from evolutionary perspective. *BMC Plant Biology 9*, 134.

Jensen K.H., Lee J., Bohr T., Bruus H., Holbrook N.M. & Zwieniecki M.A. (2011) Optimality of the münch mechanism for translocation of sugars in plants. *Journal of the Royal Society Interface 8*, 1155-1165.

Kammerloher W., Fischer U., Piechottka G.P. & Schäffner A.R. (1994) Water channels in the plant plasma membrane cloned by immunoselection from a mammalian expression system. *The Plant Journal : For Cell and Molecular Biology 6*, 187-199.

Knoblauch M., Knoblauch J., Mullendore D.L., Savage J.A., Babst B.A., Beecher S.D., Dodgen A.C., Jensen K.H. & Holbrook N.M. (2016) Testing the münch hypothesis of long distance phloem transport in plants. *Elife 5*, e15341.

Knoblauch M. & Peters W.S. (2010) Münch, morphology, microfluidics - our structural problem with the phloem. *Plant, Cell & Environment 33*, 1439-1452.

Kramer P.J. & Boyer J.S. (1995) Water relations of plants and soils. Academic Press, New York.

Larchevêque M., Maurel M., Desrochers A., & Larocque, G. R. (2011). How does drought tolerance compare between two improved hybrids of balsam poplar and an unimproved native species? *Tree Physiology 31*, 240-249.

Laur J. & Hacke U.G. (2013) Transpirational demand affects aquaporin expression in poplar roots. *Journal of Experimental Botany 64*, 2283-2293.

Laur, J., & Hacke, U. G. (2014). Exploring Picea glauca aquaporins in the context of needle water uptake and xylem refilling. *New Phytologist*, *203*, 388-400.

Lang A. & Minchin P. (1986) Phylogenetic distribution and mechanism of translocation inhibition by chilling. *Journal of Experimental Botany 37*, 389-398.

Lee, S. H., Chung, G. C., Jiang, J. Y., Ahn, S. J., & Zwiazek, J. J. (2012). Overexpression of PIP2; 5 aquaporin alleviates effects of low root temperature on cell hydraulic conductivity and growth in Arabidopsis thaliana. *Plant Physiology 159,* 479-488.

Lee, S. H., & Zwiazek, J. J. (2015). Regulation of aquaporin-mediated water transport in Arabidopsis roots exposed to NaCl. *Plant and Cell Physiology 56*, 750-758.

Liesche J. & Schulz A. (2012) In vivo quantification of cell coupling in plants with different phloem loading strategies. *Plant Physiology 159*, 355-365.

Luu D. & Maurel C. (2005) Aquaporins in a challenging environment: Molecular gears for adjusting plant water status. *Plant, Cell & Environment* 28, 85-96.

Maule, A. J., Benitez-Alfonso, Y., & Faulkner, C. (2011). Plasmodesmata–membrane tunnels with attitude. *Current Opinion in Plant Biology 14*, 683-690.

Maurel C., Javot H., Lauvergeat V., Gerbeau P., Tournaire C., Santoni V. & Heyes J. (2002) Molecular physiology of aquaporins in plants. In *International Review of Cytology,* Molecular physiology of aquaporins in plants. pp. 105-148. Elsevier Science & Technology, United States.

Maurel C., Boursiac Y., Luu D., Santoni V., Shahzad Z. & Verdoucq L. (2015) Aquaporins in plants. *Physiological Reviews* 95, 1321-58.

Maurel C., Lionel Verdoucq, Doan-Trung Luu & Véronique Santoni. (2008) Plant aquaporins: Membrane channels with multiple integrated functions. *Annual Review of Plant Biology* 59, 595-624.

Maurel C., Reizer J., Schroeder J.I. & Chrispeels M.J. (1993) The vacuolar membrane protein gamma-TIP creates water specific channels in *Xenopus* oocytes. *The EMBO Journal 12*, 2241-2247.

Maurel C., Verdoucq L. & Rodrigues O. (2016) Aquaporins and plant transpiration. *Plant, Cell & Environment 39*, 2580-2587.

McDowell N., Pockman W. T., Allen C. D., Breshears D. D., Cobb N., Kolb T. & Yepez E. A. (2008). Mechanisms of plant survival and mortality during drought: why do some plants survive while others succumb to drought?. *New phytologist 178*, 719-739.

Milburn J.A. (1974) Phloem transport in ricinus: Concentration gradients between source and sink. *Planta 117*, 303-319.

Minchin P. & Thorpe M.R. (1983) A rate of cooling response in phloem translocation. *Journal of Experimental Botany 34*, 529-536.

Moran P.J., Cheng Y., Cassell J.L. & Thompson G.A. (2002) Gene expression profiling of *Arabidopsis thaliana* in compatible plant-aphid interactions. *Archives of Insect Biochemistry and Physiology 51*, 182-203.

Mori I.C., Rhee J., Shibasaka M., Sasano S., Kaneko T., Horie T. & Katsuhara M. (2014) CO2 transport by PIP2 aquaporins of barley. *Plant & Cell Physiology 55*, 251-257.

Mullendore D.L., Windt C.W., Van As H. & Knoblauch M. (2010) Sieve tube geometry in relation to phloem flow. *The Plant Cell 22*, 579-593.

Münch E. (1927) Versuche über den Saftkreislauf. Berichte der Deutschen Botanischen Gesellschaft 45: 340-356.

Münch E. (1930) Die stoffbewegungen in der pflanze. *Gustav Fischer Verlagsb.Jena, Germany* 234.

Nobel, P. S. (2009). Physicochemical & environmental plant physiology. Academic press, New York. p. 481.

Peterson E. B., & Peterson N. M. (1992). Ecology, management, and use of aspen and balsam poplar in the prairie provinces. Northwest Region, Northern Forestry Centre, Edmonton, Alberta, Canada: Forestry Canada.

Phillips R.J. & Dungan S.R. (1993) Asymptotic analysis of flow in sieve tubes with semi-permeable walls. *Journal of Theoretical Biology 162*, 465-485.

Rennie E.A. & Turgeon R. (2009) A comprehensive picture of phloem loading strategies. *Proceedings of the National Academy of Sciences 106*, 14162-14167.

Rockwell F.E., Gersony J.T. & Holbrook N.M. (2018) Where does münch flow begin? sucrose transport in the pre-phloem path. *Current Opinion in Plant Biology 43*, 101-107.

Ross-Elliott T.J., Jensen K.H., Haaning K.S., Wager B.M., Knoblauch J., Howell A.H., Mullendore D.L., Monteith A.G., Paultre D. & Yan D. (2017) Phloem unloading in arabidopsis roots is convective and regulated by the phloem-pole pericycle. *Elife 6*, e24125.

Russin W.A. & Evert R.F. (1985) Studies on the leaf of populus deltoides (salicaceae): Quantitative aspects, and solute concentrations of the sieve-tube members. *American Journal of Botany 72*, 487-500.

Ryan M.G. & Asao S. (2014) Phloem transport in trees. *Tree Physiology 34*, 1-4.

Sade N., Shatil-Cohen A., Attia Z., Maurel C., Boursiac Y., Kelly G., Granot D., Yaaran A., Lerner S. & Moshelion M. (2014) The role of plasma membrane aquaporins in regulating the bundle sheath-mesophyll continuum and leaf hydraulics. *Plant Physiology 166*, 1609-1620.

Savage J.A., Beecher S.D., Clerx L., Gersony J.T., Knoblauch J., Losada J.M., Jensen K.H., Knoblauch M. & Holbrook N.M. (2017) Maintenance of carbohydrate transport in tall trees. *Nature Plants 3*, 965.

Schulz A. (2015) Diffusion or bulk flow: How plasmodesmata facilitate pre-phloem transport of assimilates. *Journal of Plant Research 128*, 49-61.

Sperry J.S., Adler F.R., Campbell G.S. & Comstock J.P. (1998) Limitation of plant water use by rhizosphere and xylem conductance: Results from a model. *Plant, Cell & Environment 21*, 347-359.

Thompson M.V. (2006) Phloem: The long and the short of it. *Trends in Plant Science 11*, 26-32.

Tjallingii W.F. & Hogen Esch T. (1993) Fine structure of aphid stylet routes in plant tissues in correlation with EPG signals. *Physiological Entomology 18*, 317-328.

Tomos A.D. & Leigh R.A. (1999) The pressure probe: A versatile tool in plant cell physiology. *Annual Review of Plant Biology 50*, 447-472.

Törnroth-Horsefield S., Wang Y., Hedfalk K., Johanson U., Karlsson M., Tajkhorshid E., Neutze R. & Kjellbom P. (2006) Structural mechanism of plant aquaporin gating. *Nature 439*, 688.

Truernit E. (2014) Phloem imaging. *Journal of Experimental Botany 65*, 1681-1688.

Turgeon R. (2010) The puzzle of phloem pressure. *Plant Physiology 154*, 578-581.

Turgeon, R., & Hepler, P. K. (1989). Symplastic continuity between mesophyll and companion cells in minor veins of mature *Cucurbita pepo* L. leaves. *Planta*, *179*, 24-31.

Tyree M.T. & Ewers F.W. (1991) The hydraulic architecture of trees and other woody plants. *New Phytologist 119*, 345-360.

Uehlein N., Otto B., Hanson D.T., Fischer M., McDowell N. & Kaldenhoff R. (2008) Function of nicotiana tabacum aquaporins as chloroplast gas pores challenges the concept of membrane CO2 permeability. *The Plant Cell 20*, 648-657.

van Bel A.J.E. (2019) Sieve Elements: The Favourite Habitat of Phytoplasmas. In: Musetti R., Pagliari L. (eds) Phytoplasmas. Methods in Molecular Biology, vol 1875. Humana Press, New York, NY.

van Bel A.J. & Knoblauch M. (2000) Sieve element and companion cell: The story of the comatose patient and the hyperactive nurse. *Functional Plant Biology 27*, 477-487.

van Bel A. (2003) The phloem, a miracle of ingenuity. *Plant, Cell & Environment 26*, 125-149.

Verdoucq L., Rodrigues O., Martinière A., Luu D.T. & Maurel C. (2014) Plant aquaporins on the move: Reversible phosphorylation, lateral motion and cycling. *Current Opinion in Plant Biology 22*, 101-107.

Windt C.W., Vergeldt F.J., Jager d., P.A & As v., H. (2006) MRI of long-distance water transport: A comparison of the phloem and xylem flow characteristics and dynamics in poplar, castor bean, tomato and tobacco. *Plant, Cell & Environment 29*, 1715-1729.

Zhang C., Lu Han, Thomas L. Slewinski, Jianlei Sun, Jing Zhang, Zeng-Yu Wang & Robert Turgeon. (2014) Symplastic phloem loading in poplar. *Plant Physiology 166*, 306-313.

Zhao C., Shao H. & Chu L. (2008) Aquaporin structure–function relationships: Water flow through plant living cells. *Colloids and Surfaces B: Biointerfaces 62*, 163-172.

Zwiazek J.J., Xu H., Tan X., Navarro-Ródenas A. & Morte A. (2017) Significance of oxygen transport through aquaporins. *Scientific Reports 7*, 40411.

II. Are phloem sieve tubes leaky conduits supported by numerous aquaporins?

1. Introduction

Since the pioneering work of Maurel et al. (1993) and Kammerloher et al. (1994) in discovering the first plant aquaporins, a new era of understanding the passage of water through plant membranes began. These protein water channels are noted to regulate hydraulics from roots to leaves (Postaire et al. 2010), providing exciting new opportunities to connect whole-plant water relations to molecular biology. Aquaporins have been preferentially expressed in vascular tissue suggesting "a general role of aquaporins in sap transport" (Maurel et al. 2008). Vascular tissue distributes the essential ingredients of life throughout the plant body: water, sugars, mineral nutrients, and other resources. The tissue that delivers many of these products is the phloem (van Bel 2003), wherein lies a continuous pipeline of sugar conducting sieve tubes.

The phloem is vitally important to maintain whole plant vigor as it is the tissue by which photosynthetic products are distributed (Evert 2006). In addition, the phloem propagates signals (as predicted by Münch 1927) in such forms as proteins, RNA, phytohormones (Lucas et al. 2013) and even action potentials (Fromm and Bauer 1994). Recent work has begun to elucidate the mechanisms of phloem flow (Knoblauch et al. 2016), wound response (Knoblauch et al. 2014), loading strategies (Rennie and Turgeon 2009, Turgeon 2010b, Liesche and Schulz 2012, Comtet et al. 2017, Ross-Elliott et al. 2017), as well as whole-plant physiology and eco-physiology (Woodruff 2013, Savage et al. 2015). However, despite these advances, many questions remain unresolved as to phloem cell biology, function and regulation (e.g., van Bel 2003, Turgeon 2010a, Cayla et al. 2015). This is complicated by the difficulty of studying phloem in vivo as artifacts are common when probing or making histological sections. Since the tissue is notoriously difficult to study, there has been a widening gap between theory and empirical evidence in support of phloem function (Knoblauch and Peters 2013).

Münch (1930) proposed an elegant mechanism for sugar transport through the phloem. In this "pressure-flow" hypothesis, sugars are concentrated into phloem cells adjacent to sites of photosynthesis. The high sugar concentration allows for the import of water via osmosis, pressurizing the system and leading to mass flow. At the sink, sugars are released, and water follows, thus maintaining a source to sink gradient. Although the proposed mechanism is simple, its validation in vivo has proved to be exceedingly difficult (Turgeon 2010a). Alternatively, as opposed to being a simple pipe with one entry and one exit for sugars and water, the entire pathway has been likened to dialysis tubing (Thompson 2006); in this analogy, the phloem is 'leaky' in support of delivering nutrients (Minchin and Thorpe 1987) and water to tissues encountered along the length of the pathway. This model is consistent with sucrose transporters aiding in the loading and retrieval of sucrose in both collection and transport phloem (Ayre 2011, Payyavula et al. 2011, Gould et al. 2012). The cycling of solutes and water paints a picture that the phloem, far from being a sealed pipe, is a dynamic system in constant flux with its surrounding tissues (van Bel 2003, Pfautsch et al. 2015b).

The phloem is in constant exchange and competition with water from the xylem (Münch 1927, Hölttä et al. 2006, Sevanto et al. 2011, Pfautsch et al. 2015a, Savage et al. 2015). Water deficiency may severely affect phloem translocation, possibly leading to mortality (Woodruff 2013, Sevanto et al. 2014). Thus, having tight control over the permeability of the sieve tube plasma membrane would be beneficial in accordance to the hydraulic demands of phloem and xylem conduits. Aquaporins can be gated (Törnroth-Horsefield et al. 2006) as well as cycle in and out of the plasma membrane (Conner et al. 2010; Chaumont and Tyerman 2014); these tendencies of water channels provide a logical mechanism for how they are able to regulate membrane permeability, leading to the dynamic adjustment of cellular pressure.

Aquaporin families exist throughout representatives of all terrestrial plant lineages (Chaumont and Tyerman 2014). Along with being taxonomically widespread, aquaporins maintain high expression levels in plant tissue, and may account for up to 15% of plasma membrane proteins in spinach (Monneuse et al. 2011). Further, their importance in cellular water exchange and CO_2 diffusion (Uehlein et al. 2008) equates to their wide tissue distribution (Fraysse et al. 2005). Despite their importance, documentation of aquaporins in the phloem is sparse (Jones 1995, Barrieu et al. 1998, Kirch et al. 2000, Otto and Kaldenhoff 2000, Fraysse et al. 2005) with few studies suggesting a role in phloem loading (Fraysse et al., 2005; Hachez et al., 2008) and unloading (Zhou et al. 2007). However, according to Patrick et al. (2001) and Fraysse et al. (2005), the regulation of water channels in sieve elements may be a necessary adjustment to fluctuations in xylem pressure due to variations in transpiration. Since the generation of solute and pressure gradients in sieve tubes are inherently coupled to water flow across the sieve element plasma membrane, these ideas deserve further study.

As a first step toward exploring whether aquaporins are involved in regulating the permeability of sieve element plasma membranes, we characterized the cellular and subcellular localization of PIP1 and PIP2 subfamilies in the phloem of balsam poplar (*Populus balsamifera* L.). In support of assessing hypotheses related to radial water exchange between xylem and phloem, we studied mostly transport phloem, particularly the phloem of petioles. To assess the hypothesis that aquaporins are helping to maintain pressure homeostasis throughout the sieve tube conduit, we measured the internalization of PIP1s over a diurnal cycle.

2. Materials and methods

a. Plant material

Dormant balsam poplar (*Populus balsamifera* L.) stem cuttings were obtained from Alberta-Pacific Forest Industries (AlPac) Inc., Boyle, AB, Canada in February of 2015 and 2016. The clones were from root stock at least ten years old, and the stems collected for cuttings were one year old. The specific clone reference numbers from AlPac were AP 940 (male clone) or AP 3024 (female clone). Ten-centimeter stem segments were collected and sealed in a plastic bag until ready to be rooted. Cuttings were propagated following specifications used to maximize rooting success in hybrid poplars (DesRochers and Thomas 2003): Segments were soaked in tap water for two days at room temperature prior to transplantation into an equal parts perlite/vermiculite/Sunshine soil mixture #4 (Sun Gro Horticulture, Agawam, MA, USA). Cuttings were established in a controlled growth chamber (21°C / 18°C and photoperiod 16h: 8h, light: dark, respectively) for 93 and 51 days for plants grown in 2015, and 2016, respectively. Plants were then transferred to a greenhouse (15 - 32°C) for 88 (2015) and 112 (2016) days until organ collection.

b. Tissue sampling and fixation

Root, stem, petiole, and leaf lamina samples were harvested from four plants of balsam poplar on August 10, 2015 for aquaporin antibody labeling. A fresh razor blade was used to cut 1cm long samples, which were immediately placed into individual vials of 4°C Formalin- Acidic acid – Alcohol (FAA), and then placed on ice. After 30 minutes, the FAA within each vial was discarded, and replaced with fresh FAA. The FAA was again replaced and vials were kept in a 4°C refrigerator overnight. The following day, the FAA was replaced with 50%, and then 70% ethanol.

c. Sectioning, staining, and immuno-labeling

Organ samples were embedded in paraffin using a Leica TP 1020 tissue processor (Leica Microsystems Inc., Wetzlar, Germany). Organs were oriented within wax blocks to obtain either longitudinal or transverse sections of 7µm thickness, using a rotary microtome. Superfrost® or Probe On™ Plus slides (Fisher Scientific, Pittsburgh, PA, USA) were used for light or confocal laser scanning microscopy (CLSM), respectively. Slides were flooded with warm deionized water and the cut sections were suspended on the fluid; slides were then allowed to dry on a hotplate overnight. This preparation technique allowed for a greater adherence of the tissue to the slide following immuno-labeling.

For bright field microscopy, a modified staining procedure (Clark 1981) was used with 1% Safranin O and 2% aniline blue to stain lignin and callose, respectively. After staining, slides were mounted in DPX (Sigma-Aldrich, Oakville, Ontario, USA) and Fisher Brand® #1.5 coverslips applied.

The anti-PIP1 antibodies used in this study were affinity purified from an anti-plasma membrane antiserum against the targets of the 42 N-terminal amino acids of *At*PIP1;3 (Kammerloher et al., 1994; see Supplemental Data: Appendix 2-1A for sequence alignment). The conserved 10 amino acid C-terminus of the PIP2 aquaporins were used to raise the serum of the anti-PIP2 antibodies (following Daniels et al. 1994, Kammerloher et al. 1994, Appendix 2-1B for sequence alignment). The specificity of the two antibodies was verified by Western Blot analysis (Appendix 2-2). Briefly, 5-10 µg of *P. balsamifera* shoot microsomal fraction obtained per the method described by Abas and Luschnig (2010) were denatured at 65°C for 30 min with 200mM dithiothreitol (DTT) and then separated by 12% SDS-PAGE. After transfer to a nitrocellulose membrane, they were incubated at 4°C overnight with either anti-PIP1 or anti-PIP2 primary antibodies [1/500] followed by 2h incubation at room temperature with secondary

horse-radish peroxidase antibodies [1/2000; Biorad, Canada]. An Immun-Blot Opti-4CN kit (Biorad, Canada) was used for detection.

Following a previously described method (Gong et al. 2006), immuno-labeling was performed on prepared slides to localize plasma membrane intrinsic proteins (PIPs). After dewaxing and rehydrating tissue, 80-100 µl of PIP1 or PIP2 primary antibodies [1/80] (Laur and Hacke, 2014b) were applied. The slides were covered in Parafilm® (Bemis Company Inc., Neenah, Wisconsin, USA) and kept overnight in a 4°C refrigerator. The following day, samples were rinsed using a low salt washing buffer. Alexa Fluor 488®-conjugated [goat] anti-mouse or 568®-conjugated [goat] anti-chicken secondary antibody ([1/100], Fisher Scientific) was then applied for PIP1- and PIP2-labeling, respectively, for two hours at 37°C before a final wash. Finally, slides were mounted using Slow Fade™ Gold or Slow Fade™ Gold with DAPI (Fisher Scientific) and coverslips applied. Nail polish was used to seal in the water-soluble media.

d. Super-Resolution microscopy

For super resolution light microscopy, organ samples were fixed and immuno-labeled as above. However, tissue was adhered directly to #1.5 22x22mm glass cover slips instead of glass slides. The cover slips were coated with 0.01% poly-l-lysine (Sigma-Aldrich) to improve tissue adherence. Once dewaxed, 50 µl of [1/80] PIP1/PIP2 antibody was applied and allowed to incubate overnight in a 4°C refrigerator; after, 50 µl of [1/100] PIP1/PIP2 secondary antibody were applied to the cover slips, and they were allowed to incubate at room temperature for four hours.

3D-Structured Illumination Microscopy (3D-SIM) was carried out as described previously (Fitzgibbon et al. 2010). Samples were imaged using a Deltavision OMX V4

microscope (Applied Precision Inc., Issaquah, WA, USA). Delta Vision OMX software version 3.6 (G.E. Healthcare Limited, Little Chalfont, UK) was used for capturing images; 468 and 568nm lasers were used to excite PIP2 and PIP1, respectively. Laser power was set at 1%, and exposure times were adjusted between 100 – 200ms in order to achieve intensity counts of 2000 – 4000. The 3D-SIM technique relies on achieving a balance between signal intensity and sample integrity. Too much laser exposure will result in photo bleaching, whereas not enough exposure will diminish the signal too greatly for image reconstruction. Deltavision softWoRx 6.5.1 (G.E. Healthcare) software was used for structured illumination image reconstruction using a Wiener filter of 0.001 for noise smoothing.

e. Confocal Laser Scanning Microscopy (CLSM)

A Zeiss LSM 700 (Carl Zeiss AG, Oberkochen, Germany) confocal microscope was used for aquaporin antibody imaging. For secondary immuno-labeling of PIP1 and PIP2, Alexa Fluor 488® was used, and then excited using a 488nm laser. Zeiss Zen 2011 Black Edition software was used for image processing. Laser power was set to 2%, and pinhole diameter set to 1 Airy unit. The 488nm laser was set to a camera gain of 650 and a rainbow coarse color channel applied; in addition, the 555nm laser was activated to detect background fluorescence; this channel was set to a camera gain of 800 and a grey color channel used. Digital offset and gain were set to one for both laser channels.

f. Light microscopy and Image analysis

For brightfield imaging, a Leica DM 3000 microscope fitted with a Leica DFC 420c camera was used. Images were captured using Leica Application Suite version 4.2. Image-Pro® Premier Version 9.1 (Media Cybernetics®, Inc., Rockville, MD, USA) was used for image processing

and analysis for CLSM, 3D-SIM and brightfield microscopy. The tiling function was used to stitch several smaller images together into one seamless mosaic. For the diurnal experiment, sieve tubes were identified and categorized using CLSM images of petiole phloem taken with the rainbow coarse color scale. Images were enhanced using the HDR technique in the Zeiss ZEN Black software package.

g. Diurnal experiment

Petioles were collected to determine if PIP1 aquaporins were cycling from plasma membrane to internal membrane spaces on a diurnal cycle. Petioles were collected from a random selection of 12 well-watered greenhouse grown AlPac plants (clone AP 940 or AP 3024) on August 4, 2016. Care was taken not to agitate plants physically for a 24h period prior to sample collection. One petiole was collected from the seventh youngest leaf from four different plants at each of the following sampling times: 7:30, 15:30 and 24:00. Conditions during this experiment were partly cloudy to mostly sunny with light intensity varying between 137 and 1190 mol $m^{-2}s^{-1}$ during the day.

After fixation, petiole samples were prepared as described for the labeling of PIP1 aquaporins. Sieve elements labeled with the PIP1 antibody were traced using Image Pro® software. Sieve elements within two cell layers of the cambium were omitted from the study, so as not to confound their labeling pattern with their developmental state. Intensity of antibody signal, margination, and heterogeneity tools were used to classify sieve elements into two categories: (1) sieve elements with mostly PIP1 labeling of the plasma membrane, or (2) sieve elements with mostly internalized labeling of PIP1. Generally, sieve elements would be put into the plasma membrane category if their margination value was under 0.45 (more signal closer to

the margin of the cell). In all, a total of 1240, 1041, and 1225 sieve elements were categorized from the 7:30, 15:30, and 24:00 sampled petioles, respectively.

A one factor ANOVA was used to determine differences in the fraction of sieve elements categorized with internalized PIP1. A contingency table (Chi-squared analysis) was used to determine if aquaporin distribution was independent of petioles sampled. Sigma Plot Version 13 (Systat Software Inc., San Jose, CA, USA) was used for analysis.

h. Sieve Element Dimensions

Sieve element length and diameter were measured using ImagePro® software for both 2015 and 2016 plants. For each cell membrane traced, the software calculated numerous diameters across the centroid of the cell, and then averaged these values to achieve a final diameter. Diameter and length measurements were made on confocal micrographs labeled with PIP1 or PIP2 antibodies.

3. Results

a. Detecting PIP1 aquaporins in the phloem and xylem using CLSM

Petiole (Fig. 2-1), leaf lamina (Appendix 2-3) and stem (Fig. 2-2) organs showed a similar pattern of aquaporin labeling, and their cell types were categorized together (Table 2-1). In transverse section, sieve elements could positively be identified through their agglomerations (slime plugs) at the sieve plate (Fig. 2-1A, C, *). PIP1s labeled a majority of cell types in the phloem as well as xylem rays (Fig. 2-1B). Phloem cell labeling included phloem parenchyma, companion cells, and sieve elements (Fig 2-2A, B). The cellular distribution of PIP1 had a high degree of variability; some sieve elements had a consistent internal signal throughout their length, whereas others had areas devoid of any signal prior to the slime plug (Fig 2-2B,

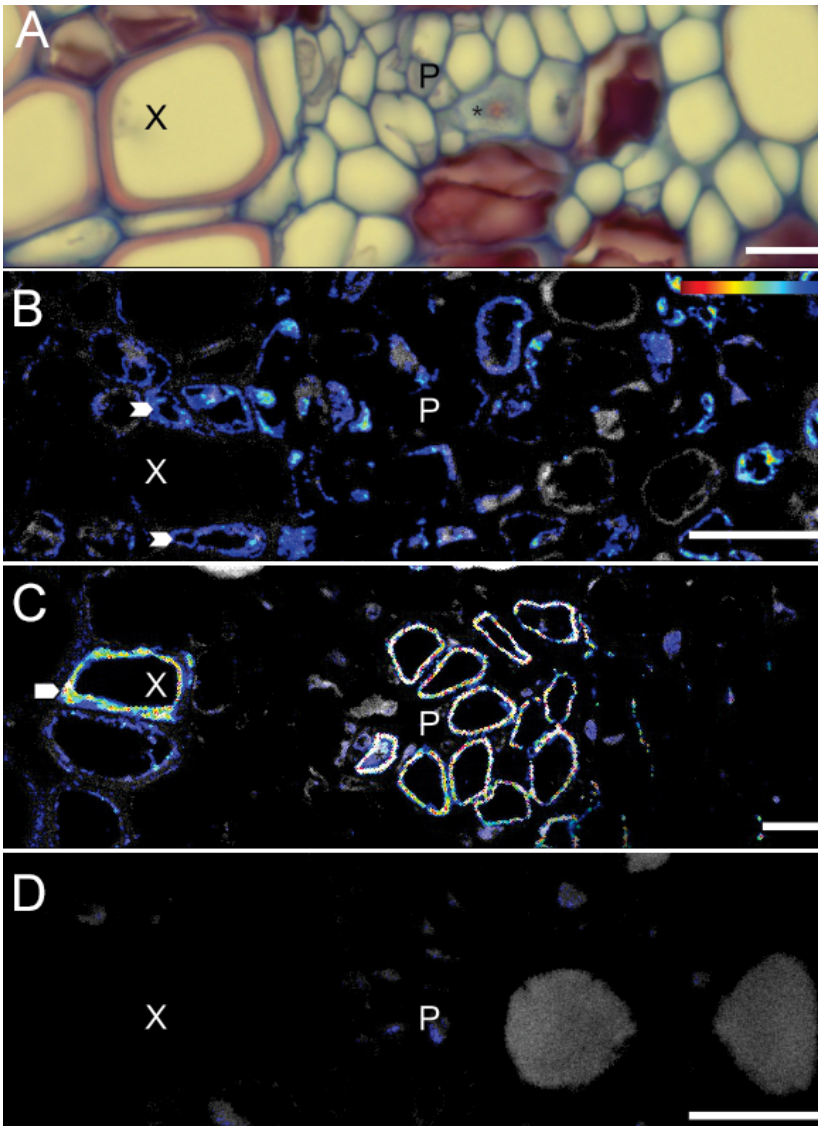

Figure 2-1: Petiole transverse section showing phloem of balsam poplar. Images are representative from four tree samples of the same genetic origin. (A) Brightfield micrograph of petiole phloem stained with aniline blue and safranin O. (B) Confocal laser scanning micrograph (CLSM) of phloem with PIP1 aquaporin antibody, arrowheads indicate xylem ray cells with PIP1 plasma membrane labeling. (C) A CLSM with PIP2 aquaporin antibody labeling of sieve elements; note the developing xylem vessel (arrowhead) with PIP2 membrane labeling. (D) A CLSM negative control (no PIP2 primary-antibody applied). Colors closer to red on the rainbow color scale represent greater fluorescence intensities; greyscale represents background fluorescence (no antibody signal). Symbols: * = sieve plate, P = phloem, X = xylem. Bars = 10µm.

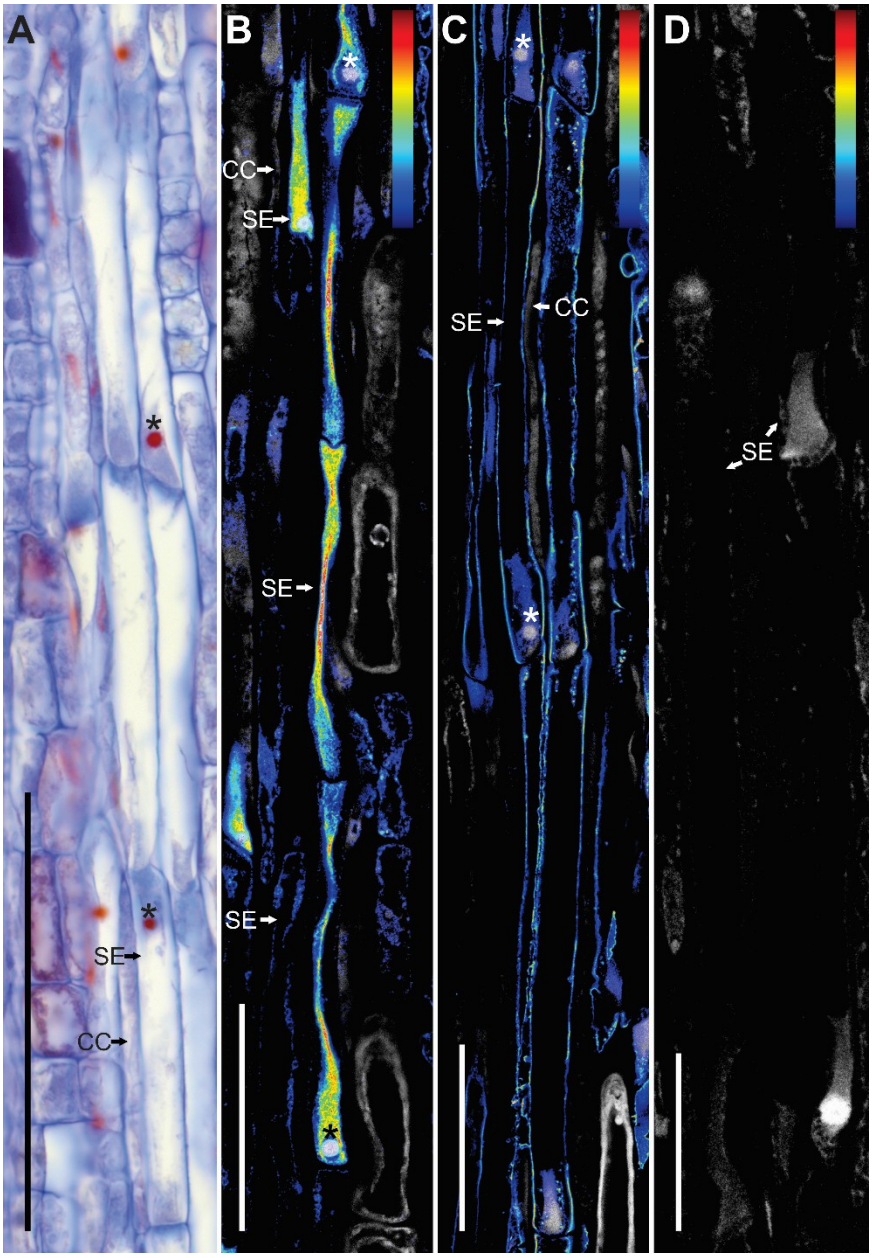

Figure 2-2: Longitudinal sections of balsam poplar stem phloem. (A) Brightfield view of two sieve tubes. (B) Confocal laser scanning micrograph of PIP1 labeling within the internal membranes of two sieve tubes. (C) PIP2 labeling in the plasma membrane of two sieve tubes. (D) Negative control (no primary and no secondary antibody) showing background fluorescence. Colors closer to red on the rainbow color scale represent greater fluorescence intensities; greyscale represents background fluorescence (no antibody signal). Symbols: * = sieve plate, arrowhead = slime plug with associated aquaporin signal, CC = companion cell, PP = phloem parenchyma, SE = sieve element. Bar = (A) 50µm, (B-C) 30µm, (D) 25µm.

Table 2-1: A summary of the observed labeling patterns in balsam poplar. The symbols in the table represent the presence of specific aquaporin subfamily localization; PM = present in plasma membrane, IM = present in internal membranes, IM + PM = present in both internal and plasma membrane.

	Aquaporin Subfamily	
Cell	PIP1	PIP2
Sieve Element	IM + PM	PM*
Companion Cell	IM	
Phloem Parenchyma	IM + PM	
Developing Vessel Element	PM	PM
Xylem Ray Cell	IM + PM	
Bundle Sheath Cell	IM + PM	PM
Spongy Mesophyll Cell	IM + PM	

Note: *The typical pattern of PIP2 was labeling in the plasma membrane only. However, there was some occasional localization in internal membranes, especially if near a sieve plate.

arrowhead). From this longitudinal perspective, we note that cross sectional views of sieve elements will sometimes have high internal membrane signaling, or sometimes none at all. Overall, PIP1s had a weaker presence of plasma membrane labeling than PIP2s (see below) and were found in higher qualitative intensities within internal compartments, if present.

In transverse view, the morphology of sieve elements was circular to oblong and of an intermediate size in comparison to other phloem cells (see Appendix 2-4 for measured sieve element diameters); the companion cells either exhibited a tooth or dumbbell shape (see Appendix 2-5 for DAPI labeled companion cells) and were the smallest of the phloem cells. As confirmed in longitudinal sections (Fig. 2-2A - C), sieve elements often occurred in pairs along the same plane. In addition, a relatively higher intensity of labeling was found throughout the length of some sieve elements (Fig. 2-2B) in comparison to surrounding cells, especially when viewed close to sieve plates. These longitudinal patterns provided clarity in the identification of sieve elements in transverse section.

b. Detecting PIP2 aquaporins in the phloem and xylem using CLSM

The distribution of PIP2 aquaporins was distinct from PIP1s in terms of phloem labeling (Table 2-1). Within the vascular cylinder, PIP2s were only found in bundle sheath cells (Appendix 2-6), phloem fibers, developing xylem vessels (Fig. 2-1C) and sieve elements (Fig. 2-1C; Fig. 2-2C). Labeling was confined to the plasma membrane, unless the section hit a sieve plate (Fig. 2-2C); sieve plates (Fig. 2-1A, Fig. 2-2A-D; asterisk) could be identified from their characteristic agglomerations accompanied by an accumulation of antibody signal. From transverse section, sieve elements grouped in distributions of 2 – 3 (Fig. 2-1C; Fig. 2-2C). They either abutted directly against each other, or were separated from one another by companion cells.

c. Characterizing cellular distribution of sieve element aquaporins using 3D-SIM

Double labeled, super resolution 3D-SIM images were obtained to verify the cell level labeling of PIP1s and PIP2s (Figs. 2-3, 2-4). In agreement with CLSM, 3D-SIM longitudinal section rotations showed distinct labeling patterns between PIP1s and PIP2s; the discernment of individual aquaporin protein groups or units can be made out in 3D-view, localized to either the plasma membrane or internal membranes in sieve elements. The two aquaporin types were seen associated with one another and their distribution clumped as opposed to scattered throughout the intracellular space.

Double-labeled transverse (Fig. 2-3B) and longitudinal (Fig. 2-3C) sections showed a strong fluorescence signal for PIP2s primarily in the plasma membrane and to a lesser extent in internal membranes of sieve elements (Fig. 2-3B, arrowheads). Alternatively, PIP1s primarily associated with internal membranes (Fig. 2-3B-D). In agreement with CLSM images, the antibody signal within internal membranes was heavily accumulated near slime plugs of sieve plates (Fig. 2-3D). PIP1s did not always show a strict internal membrane distribution (Fig. 2-4); within the same tissue section, labeling of PIP1s occurred in internal membranes only (Fig. 2-4, line i), primarily in the plasma membrane (Fig. 2-4, line ii), or both plasma membrane and internal membranes simultaneously (Fig. 2-4, line iii).

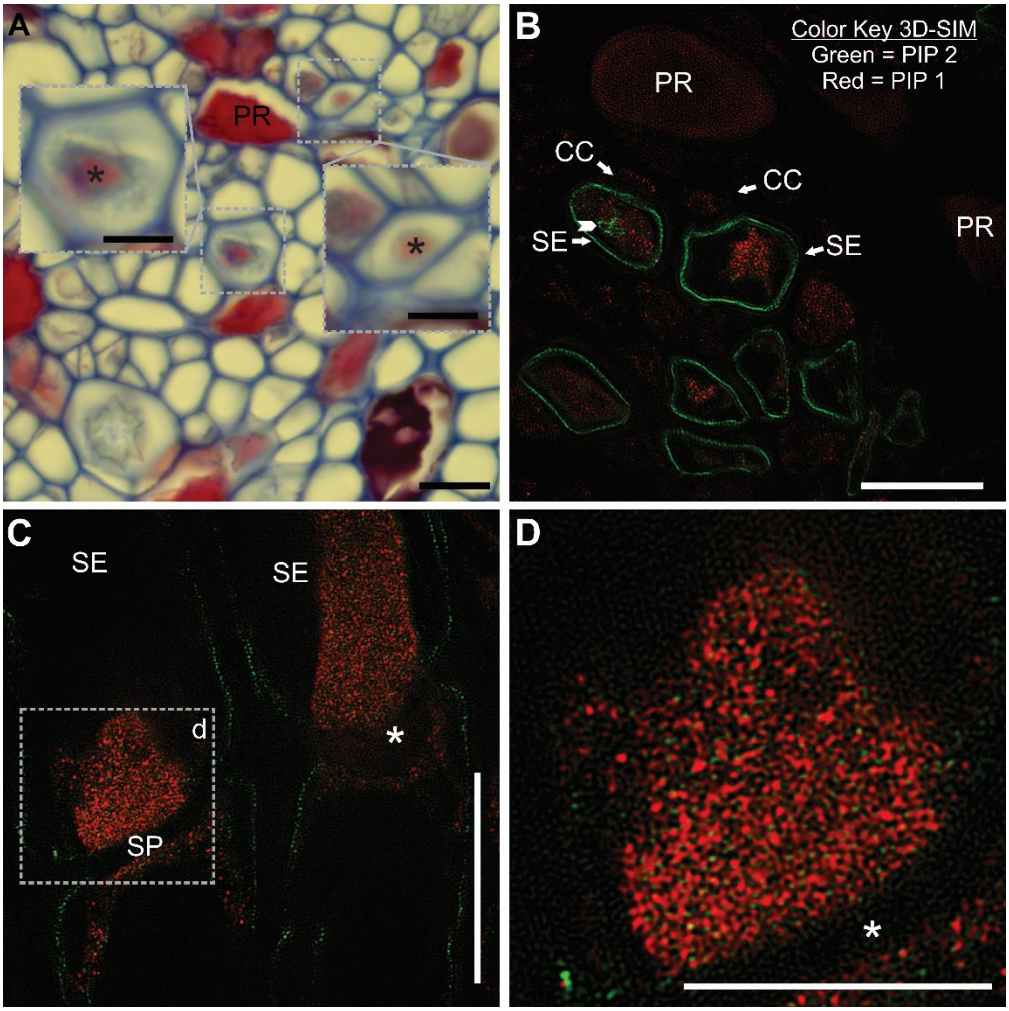

Figure 2-3: Transverse sections of leaf midvein phloem and longitudinal section of stem sieve elements. (A) Brightfield view of aniline blue and safranin O stained midvein phloem; the labeled sieve element shows a sieve plate (*) with a red safranin-stained agglomeration. (B) Double-labeled 3D-Structured Illumination Microscopy (3D-SIM) showing plasma membrane labeling of midvein sieve elements for PIP2s (green) and internal membrane labeling for PIP1s (red). The arrowhead shows PIP2 labeling within the internal membranes of the sieve element. (C) A longitudinal section of two sieve tubes in the stem tissue of balsam poplar imaged using 3D-SIM. The PIP1 aquaporin labeling (red) shows a mostly internal membrane distribution within the slime plug region (arrowhead) adjacent to the sieve plate (*). The PIP2 signal (green) was mostly detected in the plasma membrane, although weak labeling also occurred in internal membranes. (D) Enlargement of boxed area in (C). Symbols: * = sieve plate, CC = companion cell, PR = phloem ray, SE = sieve element. Bar = (A - C) 10µm, (D) 5µm.

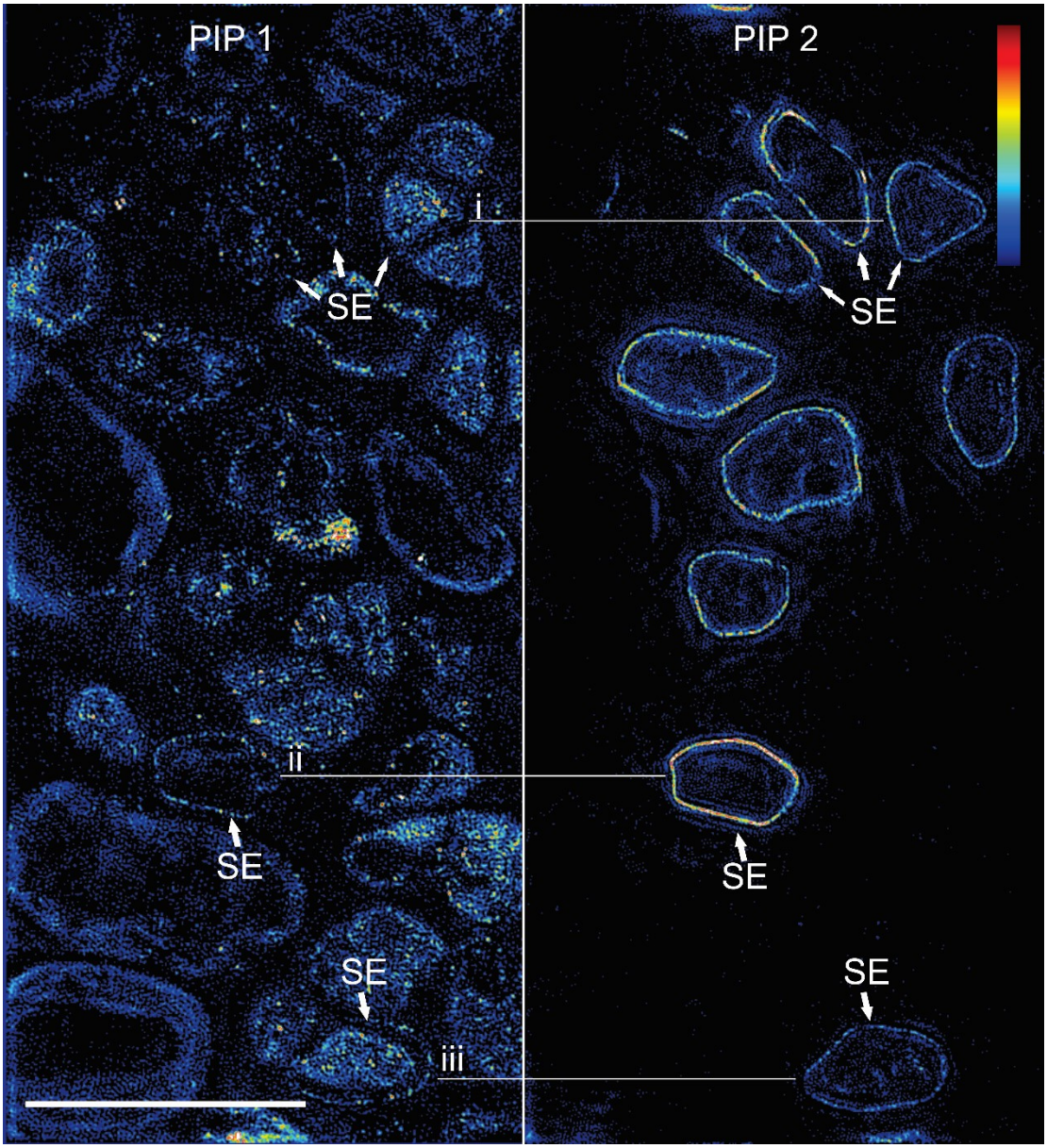

Figure 2-4: A 3D-Structured Illumination Microscopy (3D-SIM) view of phloem in a balsam poplar leaf midvein with PIP1 (left) and PIP2 labeling (right). The left and right panes are of the same exact tissue region, with different excitation wavelengths applied. The PIP2 signals are found in high intensity within the plasma membrane of sieve elements (SE). The PIP1s show more complex and variable distributions in the same tissue section; an internal membrane distribution (line i), plasma membrane distribution (line ii), or both plasma membrane and endomembrane distribution (line iii) within SEs. Colors closer to red on the scale represent greater antibody fluorescence. Bar = 10µm.

d. Diurnal cycling PIP1 aquaporins in sieve elements

To test a potential physiological response behind the cycling of PIP1 aquaporins, petioles ($N = 4$ plants per time) were sampled from three time periods within a 24-hour cycle. No significant difference was found between time periods in terms of the proportion of sieve elements showing an internalized localization of PIP1 aquaporins ($F_{2, 9} = 0.816$, $P = 0.47$; Fig. 2-5). Further, the proportion of sieve elements showing internalization of PIP1s varied significantly by petiole for the 7:30h sampling ($\chi^2 = 10.019$, df = 3, $P = 0.02$), 15:30h sampling ($\chi^2 = 72.142$, df = 3, $P < 0.001$) and 24:00h sampling ($\chi^2 = 21.935$, df = 3, $P < 0.001$) (see Appendix 2-7 for contingency tables). In sum, there was more variability between individual petioles within each treatment than between times petioles were sampled.

4. Discussion

a. PIP2s are markers of sieve tubes in poplar

Although aquaporins have been observed in the phloem of previous studies (Otto and Kaldenhoff 2000, Fraysse et al. 2005, Hachez et al. 2008, Laur and Hacke 2014b) details about the physiological significance of their presence are largely missing. Here we show that PIP2s are prominent features of sieve tubes in poplar. What are the physiological implications of this

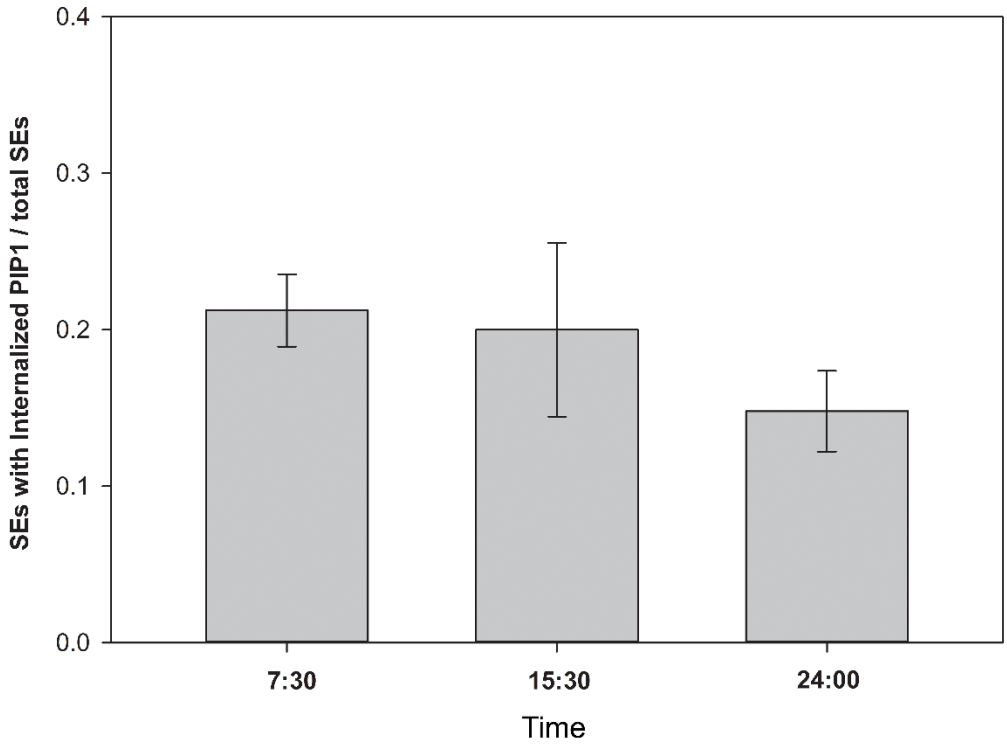

Figure 2-5: Effects of time period on the proportion of sieve elements (SEs) with PIP1 labeling in internalized membrane areas within sampled petioles (*N* = 4 plants per time of day). Data is presented as mean ratio +/- standard error.

finding? While we did not measure actual water fluxes, we offer some hypotheses that may be useful in developing more realistic phloem flow models.

The control of hydrostatic pressure is at the heart of Münch flow (Smith and Milburn 1980). From that perspective, it is hardly surprising to see close anatomical (and presumably functional) integration of sieve elements and water channels. The highly specific and consistent PIP2 labeling pattern observed suggests that the plasma membrane of sieve elements is highly permeable to water across the transport pathway in leaves, petioles and stems (Fig. 2-6). This pattern is in agreement with models of phloem flow that emphasize the duality of phloem function: long-distance transport coupled to the local exchange of solutes and water with surrounding tissues (van Bel 2003; Thompson 2006). van Bel (2003) hypothesized that "pressure is continuously lost and built up, sustained by countless aquaporins…along the sieve tube path". Linking turgor pressures in sieve elements (e.g. Knoblauch et al. 2016) as it relates to aquaporin expression would be an exciting next step in this research. Of particular interest may also be the radial water exchange between xylem and phloem. The xylem represents an important water source needed for phloem loading. Conversely, as water and solutes are unloaded in sinks, water is circulating back to the xylem. Water 'unloading' in sinks is an important aspect of the pressure-flow model (Turgeon and Medville 1998, Patrick et al. 2001, Zhou et al. 2007).

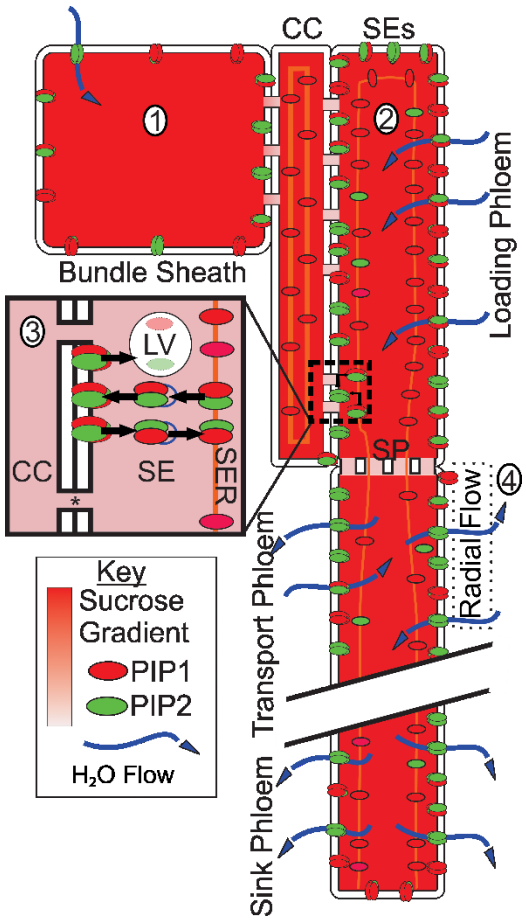

Figure 2-6: A conceptual diagram of the cellular pathway of photosynthates and water in balsam poplar, including newly discovered aquaporin water channels. Each number represents a step in the pathway: 1) Sucrose diffuses into bundle sheath cells via plasmodesmata; both PIP1s and PIP2s are found in the plasma membrane. 2) Companion cells show labeling of PIP1s in internal membranes, whereas both PIP1s and PIP2s are found in internal membranes and in the plasma membrane of sieve elements. 3) As sucrose enters sieve elements from companion cells, PIP2 aquaporins transport water in an osmotically favorable direction. 4) A close-up view of the sieve element membrane, showing cycling of PIP1s and PIP2s (Chaumont and Tyerman, 2014). PIP1s travel with PIP2s from the Sieve Element Reticulum (SER), where they are shuttled to the plasma membrane. From there, PIPs can relocate to the SER, or be destroyed in lytic vesicles (LV). 5) Radial flow may occur along the transport pathway, where water is exchanged between the xylem and phloem. Symbols: CC = Companion Cells, LV = Lytic Vesicle, SE = Sieve Elements, SER = Sieve element Endoplasmic Reticulum, * = Sieve Plate, PD = plasmodesmata.

While it is difficult to quantify radial water exchange between xylem and phloem, recent studies provide evidence for a tight hydraulic coupling between the two vascular systems (Sevanto et al. 2011, Pfautsch et al. 2015a). Since water molecules traveling between xylem and phloem will pass membranes, future models of phloem transport could include radial water flow through aquaporins as a variable and influential component of the phloem transport system.

b. The striking differences between PIP1s and PIP2s

While PIP2s were consistently observed in the plasma membrane of sieve elements, PIP1s exhibited a more complex and variable labeling pattern. One striking difference was that they labeled multiple cell types as opposed to just a few for PIP2s (Table 2-1). Why was such a difference observed? One hypothesis is that unlike PIP2s, PIP1s have multiple functions, including CO_2 (Uehlein et al. 2008), urea (Gaspar 2003) and glycerol (Biela et al. 1999) transport. PIP2s are also the major water transporting aquaporins (Yaneff et al. 2015) and PIP1s may play a supporting role in enhancing their permeability; the PIP2 distribution may therefore be targeted to cells in need of rapid water exchange (e.g. developing vessel elements). A previous study found a similar wide distribution of labeling in leaf mesophyll and vascular tissue in cottonwood (Laur and Hacke 2014a) using the same antibodies as the current study. Using different antibodies also yielded a widespread mesophyll labeling pattern in rice (Sakurai et al. 2008) for both PIP1s and PIP2s. Thus, the two subfamilies often occur together, but their roles and cellular distribution may differ.

The other striking difference between the PIP subfamilies was of their cellular distribution. Although we did not stain internal membranes, previous reports localize aquaporins to the endoplasmic reticulum (ER) (Zelazny et al. 2007, Zelazny et al. 2009, Chevalier and Chaumont 2015). PIP1s localized to either internal membranes or the plasma membrane within

sieve tubes (Fig. 2-6). These results are in contrast to the previous report of PIP1 aquaporins found only in the plasma membranes of sieve tubes in spinach (Fraysse et al. 2005). However, the presence of PIP1s in internal membranes is consistent with numerous previous observations (Robinson et al. 1996, Boursiac et al. 2005, Zelazny et al. 2007, Boursiac et al. 2008, Zelazny et al. 2009, Heinen et al. 2014, Laur and Hacke 2014b) and with our current understanding of PIP1 biology. From experiments in maize, we know that PIP1 proteins remain in the ER, and that they only relocate to the plasma membrane when they interact with PIP2 proteins (Chevalier and Chaumont 2015). In the present study, 3D-SIM microscopy revealed the presence of PIP2s in close proximity to PIP1s within internal membranes of sieve elements (Fig. 2-3D); hence, this proposed trafficking mechanism appears feasible.

One anomaly however, is the homogenous pattern of the PIP1 antibody labeling within some sieve elements. Given that aquaporins are membrane proteins, why do they often appear so diffuse inside the cell (e.g., Fig. 2-2B, Fig. 2-3B-D)? Although sieve elements lack many organelles of other living plant cells, they still possess an extensive ER network along their margin (van Bel 2003). The ER network appears amorphous when resolved with light microscopy, but is revealed as strands using electron microscopy (Evert and Murmanis 1965). After cutting, the loss of pressure is thought to cause the accumulation of parietal proteins and potentially ER against the sieve plate (van Bel 2003). Immuno-gold labeling of aquaporins using electron microscopy has shown the presence of aquaporins near ER filaments (Bilska-Kos et al. 2016), providing support to our observations of high aquaporin signal intensity within these so-called “slime bodies”. However, this still begs the question of why there are so many PIP1s within internal compartments of sieve elements in the first place?

c. Do PIP1s have a regulatory role in phloem transport?

Intra-cellular trafficking of PIPs seem to respond to hormonal and environmental stimuli, including osmotic stress (Luu et al. 2012, Ueda et al. 2016). In mammals, trafficking of AQP1 to and from the plasma membrane also occurs in response to changing osmotic environments (Conner et al. 2010). In poplar, co-expression of a PIP1 protein with proteins from the PIP2 subfamily resulted in an increase in membrane permeability beyond the level observed with PIP2 alone in seven out of eight tested interactions (Secchi and Zwieniecki 2010). Thus, changes in the localization pattern of PIP1 may respond according to environmental factors, which coincides with an adjustment of water flow into or out of the cell.

We therefore hypothesize that PIP1s support PIP2s in acting as dynamic regulators of membrane permeability and hydrostatic pressure in sieve elements. To maintain phloem pressure homeostasis, PIP1s may enter or leave the plasma membrane to increase or decrease membrane permeability. The hypothesis could be tested by combining immuno-localization experiments with the blockage treatments described by Gould et al. (2004); in this study, workers subjected stems to a sudden phloem blockage (via cooling), and then recorded sieve tube pressures up and downstream of the cold block. A steep transient increase of hydrostatic pressure was observed upstream of the cold block, but pressures returned to normal within two minutes. This result suggests a tight regulation of sieve tube pressure via changes in radial flows of water and solutes across the plasma membrane.

The living sieve tube may also respond to subtle changes in its environment. To further explore this idea, we observed patterns of PIP1 localization throughout a 24h cycle. Given that aquaporin transcript abundance has been shown to fluctuate on a diurnal cycle in *Samanea saman* leaves (Moshelion et al. 2002), it would follow that localization patterns could change as well to regulate conduit pressure. While we found no diurnal effect on the internalization of these

aquaporins (Fig. 2-5), our results do not necessarily contradict the pressure homeostasis hypothesis.

It is possible that our standard confocal microscopy technique did not provide the necessary resolution to discern fine-scale trafficking of water channels. Advanced detection methods such as FRET imaging (Zelazny et al. 2007, Besserer et al. 2012) may enhance our view of intracellular location. Another complication is that localization patterns showed a high degree of variability, at both the tissue (Fig. 2-1B) and cellular level (Figs. 2-2-4). Previous reports indicate internalization of PIP1 due to salt (Boursiac et al. 2005) and oxidative (Boursiac et al. 2008) stress. Application of more extreme abiotic stresses than diurnal cycling may thus be used in future experiments in order to detect clear differences in immuno-localization patterns. However, diurnal changes in aquaporin localization and activity would be consistent with observed changes in phloem volume (Windt et al. 2006). The phloem expands at night, and contracts during the day (Hölttä et al. 2006, Sevanto et al. 2011), which corresponds to diurnal changes in modeled phloem turgor (Mencuccini et al. 2013) and photo-assimilate concentration (Mitchell and Madore 1992).

d. Why was the PIP2 signal exclusively found in sieve elements?

While we expected to find aquaporin labeling in phloem cells of poplar based on previous reports (Almeida-Rodriguez and Hacke 2012, Laur and Hacke 2014a, Hacke and Laur 2016), we were surprised that PIP2s exclusively labeled sieve elements. Given that sieve elements and companion cells represent a functional unit and that the PIP2 transcripts must be produced in companion cells, one may wonder why these cells were not labeled? In apoplastic loaders, aquaporins in companion cells have been hypothesized to support the activity of sucrose pumps (Schulz 2015) by facilitating water movement into sieve elements. However, poplar is a

symplastic loader (Zhang et al. 2014), having a continuous connection via plasmodesmata between mesophyll and sieve elements (Russin and Evert 1985). Thus, it makes sense that the apoplastic loaders need an additional pressure boost from aquaporins to begin the flow of assimilates into the sieve tube conduit.

How is sucrose moved along in the pre-phloem pathway of a symplastic loading species? Schulz (2015) suggested that this process may be via bulk flow. This idea is supported by the calculations of Fricke (2016) who reasoned that plasmodesmata pores are large enough to sustain pressure driven flow, although this has not yet been tested. Alternatively, van Bel (2003) argued that immense pressures are needed to transport fluids through narrow glass capillary tips, and that the pressure drop may be even greater when sap moves through even narrower plasmodesmata. Integrating our results into this quandary, we tentatively distinguish a symplastic high resistance pre-sieve element pathway in which sucrose and water diffuse through plasmodesmata, and a low resistance, longer-distance pathway consisting of sieve tubes. Münch flow is restricted to sieve tubes; hence, it is here where water channels ought to contribute to maintaining favorable pressures.

5. References

Abas L. & Luschnig C. (2010) Maximum yields of microsomal-type membranes from small amounts of plant material without requiring ultracentrifugation. *Analytical Biochemistry 401*, 217-227.

Almeida-Rodriguez A. M., & Hacke, U. G. (2012). Cellular localization of aquaporin mRNA in hybrid poplar stems. *American Journal of Botany 99*, 1249-1254.

Ayre B. G. (2011). Membrane-transport systems for sucrose in relation to whole-plant carbon partitioning. *Molecular Plant 4*, 377-394.

Barrieu F., Chaumont F. & Chrispeels M.J. (1998) High expression of the tonoplast aquaporin ZmTIP1 in epidermal and conducting tissues of maize. *Plant Physiology 117*, 1153-1163.

Besserer A., Burnotte E., Beinert G.P., Chevalier A.S., Errachid A., Grefen C., Blatt M.R. & Chaumont F. (2012) Selective Regulation of Maize Plasma Membrane Aquaporin Trafficking and Activity by the SNARE SYP121. *The Plant Cell 24*, 3463-3481.

Biela A., Grote K., Otto B., Hoth S., Hedrich R. & Kaldenhoff R. (1999) The Nicotiana tabacum plasma membrane aquaporin NtAQP1 is mercury-insensitive and permeable for glycerol. *Plant Journal 18*, 565-570.

Bilska-Kos A., Grzybowski M., Jończyk M. & Sowiński P. (2016) In situ localization and changes in the expression level of transcripts related to intercellular transport and phloem loading in leaves of maize (Zea mays L.) treated with low temperature. *Acta Physiologiae Plantarum 38*, 123.

Boursiac Y., Chen S., Luu D., Sorieul M., van den Dries N. & Maurel C. (2005) Early effects of salinity on water transport in arabidopsis roots. molecular and cellular features of aquaporin expression. *Plant Physiology 139*, 790-805.

Boursiac Y., Boudet J., Postaire O., Luu D.T., Tournaire-Roux C. & Maurel C. (2008) Stimulus-induced downregulation of root water transport involves reactive oxygen species-activated cell signalling and plasma membrane intrinsic protein internalization. *The Plant Journal 56*, 207-218.

Cayla T., Batailler B., Le Hir R., Revers F., Anstead J.A., Thompson G.A., Grandjean O. & Dinant S. (2015) Live imaging of companion cells and sieve elements in arabidopsis leaves. *PloS One 10*, e0118122.

Chaumont F. & Tyerman S.D. (2014) Aquaporins: Highly regulated channels controlling plant water relations. *Plant Physiology 164*, 1600-1618.

Chevalier A.S. & Chaumont F. (2015) The LxxxA motif in the third transmembrane helix of the maize aquaporin ZmPIP2;5 acts as an ER export signal. *Plant Signaling & Behavior 10*, e990845.

Clark G. (1981) Staining procedures. In Staining Procedures Staining procedures. William & Wilkins.

Comtet J., Jensen K.H., Turgeon R., Stroock A.D. & Hosoi A.E. (2017) Passive phloem loading and long-distance transport in a synthetic tree-on-a-chip. *Nature Plants 3*, 17032.

Conner M.T., Conner A.C., Brown J.E.P. & Bill R.M. (2010) Membrane Trafficking of Aquaporin 1 Is Mediated by Protein Kinase C via Microtubules and Regulated by Tonicity. *Biochemistry 49*, 821-823.

Daniels M.J., Mirkov T.E., Chrispeels M.J. (1994) The plasma membrane of Arabidopsis thaliana contains a mercury-insensitive aquaporin that is a homolog of the tonoplast water channel protein TIP. *Plant Physiology 106*, 1325-1333.

DesRochers A. & Thomas B. (2003) A comparison of pre-planting treatments on hardwood cuttings of four hybrid poplar clones. *New Forests* 26, 17-32.

Evert R.F. (2006) Esau's Plant anatomy: meristems, cells, and tissues of the plant body: their structure, function, and development. 3rd ed. Wiley-Interscience, Hoboken, N.J.

Evert R.F. & Murmanis. 1965. Ultrastructure of Secondary Phloem of Tilia americana. *American Journal of Botany 52*, 95-106.

Fitzgibbon J, Bell K, King E, Oparka K (2010) Super-Resolution Imaging of Plasmodesmata Using Three-Dimensional Structured Illumination Microscopy. *Plant Physiol 153*, 1453-1463.

Fraysse L.C., Wells B., McCann M.C. & Kjellbom P. (2005) Specific plasma membrane aquaporins of the PIP1 subfamily are expressed in sieve elements and guard cells. Biology of the *Cell 97*, 519-534.

Fricke W. (2016). Water transport and energy. *Plant, Cell & Environment 40*, 977-994.

Gaspar, M. (2003) Cloning and characterization of ZmPIP1-5b, an aquaporin transporting water and urea. *Plant Science 165*, 21-31.

Gong H., Peng Y., Zou C., Wang D., Xu Z. & Bai S. (2006) A simple treatment to significantly increase signal specificity in immunohistochemistry. *Plant Molecular Biology Reporter 24*, 93-101.

Gould N., Minchin P.E.H. & Thorpe M.R. (2004) Direct measurements of sieve element hydrostatic pressure reveal strong regulation after pathway blockage. *Functional Plant Biology 31*, 987-993.

Gould N., Thorpe M.R., Pritchard J.T., Christeller L.E, Williams G., Roeb U., Schurr U. & Minchin P.E.H. (2012) AtSUC2 has a role for sucrose retrieval along the phloem pathway: Evidence from carbon-11 tracer studies. *Plant Science 188*, 97-101.

Hachez C., Heinen R.B., Draye X. & Chaumont F. (2008) The expression pattern of plasma membrane aquaporins in maize leaf highlights their role in hydraulic regulation. *Plant Molecular Biology 68*, 337-353.

Hacke U.G. & Laur J. (2016) Aquaporins: Channels for the Molecule of Life. *eLS*, 1-6.

Heinen R.B., Beinert G.P., Cohen D., Chevalier N., Uehlein C., Hachez R., Kaldenhoff R. et al. (2014) Expression and characterization of plasma membrane aquaporins in stomatal complexes of Zea mays. *Plant Molecular Biology 86*, 335-350.

Hölttä T., Mencuccini M. & Nikinmaa E. (2009) Linking phloem function to structure: Analysis with a coupled xylem–phloem transport model. *Journal of Theoretical Biology 259*, 325-337.

Jones J.M. (1995) Developmental expression of a turgor-responsive gene that encodes an intrinsic membrane protein. *Plant Molecular Biology 28*, 983-996.

Kammerloher W., Fischer U., Piechottka G.P. & Schäffner A.R. (1994) Water channels in the plant plasma membrane cloned by immunoselection from a mammalian expression system. The Plant Journal : *For Cell and Molecular Biology 6*, 187-199.

Kirch, H. H., Vera-Estrella, R., Golldack, D., Quigley, F., Michalowski, C. B., Barkla, B. J., & Bohnert, H. J. (2000) Expression of water channel proteins in Mesembryanthemum crystallinum. *Plant Physiology 123*, 111-124.

Knoblauch, M., & Peters, W. S. (2013) Long-distance translocation of photosynthates: a primer. *Photosynthesis research 117*, 189-196.

Knoblauch M., Froelich D.R., Pickard W.F. & Peters W.S. (2014) SEORious business: Structural proteins in sieve tubes and their involvement in sieve element occlusion. *Journal of Experimental Botany 65*, 1879-1893.

Knoblauch M., Knoblauch J., Mullendore D.L., Savage J.A., Babst B.A., Beecher S.D., Dodgen A.C., Jensen K.H. & Holbrook N.M. (2016) Testing the münch hypothesis of long distance phloem transport in plants. *Elife 5*, e15341.

Laur, J., & Hacke, U. G. (2014) The role of water channel proteins in facilitating recovery of leaf hydraulic conductance from water stress in *Populus trichocarpa*. *PloS one 9*, e111751.

Laur J & Hacke UG (2014) Exploring Picea glauca aquaporins in the context of needle water uptake and xylem refilling. *New Phytol 203*, 388-400.

Liesche J. & Schulz A. (2012) In vivo quantification of cell coupling in plants with different phloem loading strategies. *Plant Physiology 159*, 355-365.

Lucas W.J., Groover A., Lichtenberger R., Furuta K., Yadav S., Helariutta Y., He X., Fukuda H., Kang J., Brady S.M., Patrick J.W., Sperry J., Yoshida A., López-Millán A., Grusak M.A. & Kachroo P. (2013) The plant vascular system: Evolution, development and FunctionsF. *Journal of Integrative Plant Biology 55*, 294-388.

Luu D. & Maurel C. (2005) Aquaporins in a challenging environment: Molecular gears for adjusting plant water status. *Plant, Cell & Environment 28*, 85-96.

Maurel C., Reizer J., Schroeder J.I. & Chrispeels M.J. (1993) The vacuolar membrane protein gamma-TIP creates water specific channels in xenopus oocytes. *The EMBO Journal 12*, 2241-2247.

Maurel C., Lionel Verdoucq, Doan-Trung Luu & Véronique Santoni. (2008) Plant aquaporins: Membrane channels with multiple integrated functions. *Annual Review of Plant Biology 59*, 595-624.

Moshelion, M., Becker, D., Biela, A., Uehlein, N., Hedrich, R., Otto, B., ... & Kaldenhoff, R. (2002) Plasma membrane aquaporins in the motor cells of *Samanea saman*: diurnal and circadian regulation. *The Plant Cell 14*, 727-739.

Mencuccini, M., Hölttä, T., Sevanto, S., & Nikinmaa, E. (2013) Concurrent measurements of change in the bark and xylem diameters of trees reveal a phloem-generated turgor signal. *New phytologist 198*, 1143-1154.

Minchin P. & Thorpe M.R. (1987) Measurement of unloading and reloading of photo-assimilate within the stem of bean. *Journal of Experimental Botany 38*, 211-220.

Mitchell, D. E., & Madore, M. A. (1992) Patterns of assimilate production and translocation in muskmelon (Cucumis melo L.): II. Low temperature effects. *Plant Physiology 99*, 966-971.

Monneuse, J. M., Sugano, M., Becue, T., Santoni, V., Hem, S., & Rossignol, M. (2011) Towards the profiling of the Arabidopsis thaliana plasma membrane transportome by targeted proteomics. *Proteomics 11*, 1789-1797.

Münch E. (1927) Versuche über den Saftkreislauf. Berichte der Deutschen Botanischen Gesellschaft *45*, 340-356.

Münch E. (1930) Die stoffbewegungen in der pflanze. Gustav Fischer Verlagsb. Jena, Germany, p. 234.

Otto, B., & Kaldenhoff, R. (2000) Cell-specific expression of the mercury-insensitive plasma-membrane aquaporin NtAQP1 from *Nicotiana tabacum*. *Planta 211*, 167-172.

Patrick, J. W., Zhang, W., Tyerman, S. D., Offler, C. E., & Walker, N. A. (2001). Role of membrane transport in phloem translocation of assimilates and water. *Functional Plant Biology 28*, 697-709.

Payyavula R.S., Tay K.H.C., Tsai C. & Harding S.A. (2011) The sucrose transporter family in populus: The importance of a tonoplast PtaSUT4 to biomass and carbon partitioning. *The Plant Journal 65*, 757-770.

Pfautsch, S., Renard, J., Tjoelker, M., & Salih, A. (2015a) Phloem as capacitor-radial transfer of water into xylem of tree stems occurs via symplastic transport in ray parenchyma. *Plant Physiology 167*, 963-971.

Pfautsch, S., Hölttä, T., & Mencuccini, M. (2015b) Hydraulic functioning of tree stems—fusing ray anatomy, radial transfer and capacitance. *Tree Physiology 35*, 706-722.

Postaire, O., Tournaire-Roux, C., Grondin, A., Boursiac, Y., Morillon, R., Schäffner, A. R., & Maurel, C. (2010). A PIP1 aquaporin contributes to hydrostatic pressure-induced water transport in both the root and rosette of Arabidopsis. *Plant Physiology 152*, 1418-1430.

Rennie E.A. & Turgeon R. (2009) A comprehensive picture of phloem loading strategies. *Proceedings of the National Academy of Sciences 106*, 14162-14167.

Robinson, D. G., Sieber, H., Kammerloher, W., & Schaffner, A. R. (1996) PIP1 aquaporins are concentrated in plasmalemmasomes of Arabidopsis thaliana mesophyll. *Plant Physiology 111*, 645-649.

Ross-Elliott T.J., Jensen K.H., Haaning K.S., Wager B.M., Knoblauch J., Howell A.H., Mullendore D.L., Monteith A.G., Paultre D. & Yan D. (2017) Phloem unloading in arabidopsis roots is convective and regulated by the phloem-pole pericycle. *Elife 6*, e24125.

Russin W.A. & Evert R.F. (1985) Studies on the leaf of populus deltoides (salicaceae): Quantitative aspects, and solute concentrations of the sieve-tube members. *American Journal of Botany 72*, 487-500.

Sakurai, J., Ahamed, A., Murai, M., Maeshima, M., & Uemura, M. (2008) Tissue and cell-specific localization of rice aquaporins and their water transport activities. *Plant and Cell Physiology 49*, 30-39.

Savage, J. A., Clearwater, M. J., Haines, D. F., Klein, T., Mencuccini, M., Sevanto, S., ... & Zhang, C. (2015). Allocation, stress tolerance and carbon transport in plants: how does phloem physiology affect plant ecology? *Plant, Cell & Environment 39*, 709-725.

Schulz A. (2015) Diffusion or bulk flow: How plasmodesmata facilitate pre-phloem transport of assimilates. *Journal of Plant Research 128*, 49-61.

Secchi, F., & Zwieniecki, M. A. (2010) Patterns of PIP gene expression in Populus trichocarpa during recovery from xylem embolism suggest a major role for the PIP1 aquaporin subfamily as moderators of refilling process. *Plant, Cell & Environment 33*, 1285-1297.

Sevanto, S., Hölttä, T., & Holbrook, N. M. (2011) Effects of the hydraulic coupling between xylem and phloem on diurnal phloem diameter variation. *Plant, Cell & Environment 34*, 690-703.

Sevanto S., McDowell N.G., Dickman L.T., Pangle R. & Pockman W.T. (2014) How do trees die? A test of the hydraulic failure and carbon starvation hypotheses. *Plant, Cell & Environment 37*, 153-161.

Smith, J. A. C., & Milburn, J. A. (1980) Phloem turgor and the regulation of sucrose loading in *Ricinus communis* L. *Planta 148*, 42-48.

Thompson M.V. (2006) Phloem: The long and the short of it. *Trends in Plant Science 11*, 26-32.

Törnroth-Horsefield S., Wang Y., Hedfalk K., Johanson U., Karlsson M., Tajkhorshid E., Neutze R. & Kjellbom P. (2006) Structural mechanism of plant aquaporin gating. *Nature 439*, 688.

Turgeon R. (2010a) The puzzle of phloem pressure. *Plant Physiology 154*, 578-581.

Turgeon, R. (2010b) The role of phloem loading reconsidered. *Plant Physiology 152*, 1817-1823.

Turgeon, R., & Medville, R. (1998) The absence of phloem loading in willow leaves. *Proceedings of the National Academy of Sciences 95*, 12055-12060.

Ueda, M., Tsutsumi, N., & Fujimoto, M. (2016). Salt stress induces internalization of plasma membrane aquaporin into the vacuole in Arabidopsis thaliana. *Biochemical and biophysical research communications 474*, 742-746.

Uehlein N., Otto B., Hanson D.T., Fischer M., McDowell N. & Kaldenhoff R. (2008) Function of nicotiana tabacum aquaporins as chloroplast gas pores challenges the concept of membrane CO2 permeability. *The Plant Cell 20*, 648-657.

van Bel A. (2003) The phloem, a miracle of ingenuity. *Plant, Cell & Environment 26*, 125-149.

Windt C.W., Vergeldt F.J., Jager d., P.A & As v., H. (2006) MRI of long-distance water transport: A comparison of the phloem and xylem flow characteristics and dynamics in poplar, castor bean, tomato and tobacco. *Plant, Cell & Environment 29*, 1715-1729.

Woodruff D. R. (2013) The impacts of water stress on phloem transport in Douglas-fir trees. *Tree Physiology 34*, 5-14.

Yaneff, A., Vitali, V., & Amodeo, G. (2015) PIP1 aquaporins: Intrinsic water channels or PIP2 aquaporin modulators?. *FEBS letters 589*, 3508-3515.

Zelazny, E., Miecielica, U., Borst, J. W., Hemminga, M. A., & Chaumont, F. (2009) An N-terminal diacidic motif is required for the trafficking of maize aquaporins ZmPIP2; 4 and ZmPIP2; 5 to the plasma membrane. *The Plant Journal 57*, 346-355.

Zelazny, E., Borst, J. W., Muylaert, M., Batoko, H., Hemminga, M. A., & Chaumont, F. (2007) FRET imaging in living maize cells reveals that plasma membrane aquaporins interact to regulate their subcellular localization. *Proceedings of the National Academy of Sciences 104*, 12359-12364.

Zhang C., Lu Han, Thomas L. Slewinski, Jianlei Sun, Jing Zhang, Zeng-Yu Wang & Robert Turgeon. (2014) Symplastic phloem loading in poplar. *Plant Physiology 166*, 306-313.

Zhou, Y., Setz, N., Niemietz, C., Qu, H., Offler, C. E., Tyerman, S. D., & Patrick, J. W. (2007) Aquaporins and unloading of phloem-imported water in coats of developing bean seeds. *Plant, Cell & Environment 30*, 1566-1577.

III. Aquaporins Respond to Chilling in the Phloem by Increased Protein Abundance and Altered mRNA Expression

1. Introduction

The phloem vascular tissue is the predominant passageway for photosynthetically derived nutrients to be propagated around the body of the plant. Within the phloem lies the sieve tube conduit which is responsible for the transport of not only sugars, but also the transmission of signals in the form of mRNA (Sasaki et al. 1998), amino acids (Mittler 1953) and electrical action potentials (Sibaoka 1962). Thus the phloem is the critical pipeline for energy transmission needed for overall plant homeostasis, as well as the coordination of defenses in such events as insect attack (Muday & Brown-Harding 2018), viral outbreak (Chisholm et al. 2001), or drought stress (Walz et al. 2002). Although we are gaining a better understanding about both the control and motive force behind fluid movement within phloem sieve tubes, many questions remained unresolved in terms of its mechanism of action. Previous research for sugar translocation is often focused on loading near source tissue (e.g. leaves) (Comtet, Turgeon & Stroock 2017, Comtet et al. 2017, Rennie & Turgeon 2009) or unloading near sink tissue (e.g., roots) (Ross-Elliott et al. 2017). However, the intervening transport phloem which connects source and sink is often neglected due to the difficulty of accessing this deeply embedded tissue. The importance of the transport phloem for influencing long distance translocation cannot be understated, as it may act as an exchange point for water and nutrients (van Bel 2003) which has been modeled to significantly influence pressure profiles (Stanfield et al. 2018).

An important set of experiments that have been performed on transport phloem has used the application of a heat exchanger, or cold block, to rapidly cool a section of stem. As early as 1912, experiments have been performed which demonstrated the inhibitory effect on phloem transport by applying cold to a small section of stem (Geiger & Sovonick 1975). The inhibitory effect on translocation via stem cooling has been measured via carbon isotope tracing of the

phloem in a variety of species (Lang & Minchin 1986). While testing 86 species of angiosperms, all dicots and 30% of monocots experienced a cold-induced inhibition of translocation. Upon cooling a 10mm section of stem, chilling sensitive plants showed an immediate halt of translocation, but then recovered within 3-5 mins of rewarming; previously, morning glory was shown to recover after warming within seconds (Minchin & Thorpe 1983). A more recent study showed that in cow thistle, not only does translocation stop, but a pressure builds up in the sieve tube which occurs upstream of the cold block (Gould et al. 2004). This pressure begins to decline to pre-chill levels within 10 mins of chilling. The reversibility of the cold response while the cold treatment is still being applied warrants many hypotheses as to the cause of temporary cold induced phloem blockage.

One mechanism of cold induced blockage is that the sieve plates within each sieve tube become blocked after a chilling due to the dispersion of p-protein filaments which clog sieve plate pores (Giaquinta & Geiger 1973). The dispersion of these so called forisome p-proteins have been demonstrated to disperse rapidly following cooling due to a depolarization of the sieve element membrane in bean plants (Thorpe et al. 2010). However, this explanation does not fully explain why translocation stops in species which do not possess dispersive p-proteins commonly found in legumes (Lang & Minchin 1986) or in poplar (Mullendore et al. 2018). In addition, forisomes in *Arabidopsis* that appeared to cover sieve plates did not seem to inhibit phloem transport according to in vivo imaging (Froelich et al. 2011). An alternative explanation is that the plasma membrane of sieve elements is somehow disrupted due to the chilling (Lang & Minchin 1986, Minchin & Thorpe 1983). This in turn may hinder the ability of the sieve element membrane to retrieve assimilates and water that passively leak out along the transport pathway. Since the retrieval of water and solutes is hypothesized to be essential in maintaining mass flow

(Thompson 2006), it is plausible that a cold induced disruption of the plasma membrane may impact flow. In addition, it is hypothesized that the specific element of the membrane disrupted by cold could be solute and aquaporin water transporters (Gould, Minchin & Thorpe 2004).

Aquaporins are intrinsic membrane bound proteins primarily responsible for the passage of water across the plasmalemma or tonoplast (Kammerloher et al. 1994, Maurel et al. 1993). A variety of protein isoforms exist (Chaumont & Tyerman 2014), with their role in transporting not only water, but also CO_2 (Uehlein et al. 2008) and O_2 (Zwiazek et al. 2017). They occur in a variety of sub-types (isoforms), including the PIPs (Plasma Membrane Intrinsic Proteins) which are the major water transporting isoforms found in plants (Chaumont & Tyerman 2014). In response to environmental stress such as cold, aquaporins may react in multiple ways to counteract the loss of hydraulic conductivity of the tissue that is chilled (Luu & Maurel 2005). The effect of chilling on aquaporins has been shown by a down regulation of mRNA transcript, but an upregulation in protein expression in maize roots (Aroca et al. 2005). In addition, aquaporins are more likely to be phosphorylated when exposed to a chilling event, which is a gating mechanism to open the water channel (Törnroth-Horsefield et al. 2006). Aquaporins play an important role in mediating the hydraulic conductivity of roots is tree species of poplar (Marjanovic´ et al. 2005), and likewise respond to chilling through altered transcript abundance (Lee et al. 2012). However, it is important to note that both the mRNA expression and protein expression of aquaporins in response to cold may depend on the chilling tolerance of the species tested, as well as the duration of the chilling treatment (Ahamed et al. 2012, Bilska-Kos, Szczepanik & Sowiński 2016).

Previous cold block experiments on phloem transport have mainly focused on translocation rates using isotope tracing (Minchin & Thorpe 1983, Minchin & Thorpe 1987,

Lang & Minchin 1986, Pickard & Minchin 1990) or pressure (Gould, Minchin & Thorpe 2004). However, no studies to date have shown the effect of aquaporin cold response within sieve tubes. Despite work that shows how aquaporin cellular location, protein and mRNA transcript abundance change in accordance to environmental stress such as cold (Maurel et al. 2015) it is unknown how these parameters change within phloem sieve tubes. Previous work on aquaporins show that a different pattern of localization occurs between the PIP1 and PIP2 isoforms (Stanfield et al. 2017). Whereas PIP1 predominately are found within internal compartments, PIP2 is found to occur mainly in the plasma membrane of sieve tubes in poplar. This shows that aquaporins may dynamically change within sieve tubes to compensate for changes in water potential. Thus, the first objective of this study was to ascertain if localization patterns and protein abundance changed in accordance to cold block treatment using immunohistochemistry. Next, we sought to determine mRNA transcript abundance using reverse transcription polymerase chain reaction (qrtPCR) and how this was changed according to cold block treatment. According to the work of Gould et al. (2004), there was a transient increase in sieve tube pressure immediately after cold block treatment began in cow thistle. In this previous work, after 2 mins of chilling, the sieve tube pressure began recovering to pre-chill levels. The location of these previously studied effects was upstream (towards the photosynthetic source) of the coldblock. Thus, we hypothesize that aquaporins increase in protein abundance at the cold block site as well as mobilize in greater quantities in the plasma membrane to release water quickly from sieve tubes following a chilling event. In addition, we expect mRNA transcript abundance to increase as well from stem tissue located around the site of cold block application.

2. Materials and Methods

a. Plant materials

Initial dormant balsam poplar (*Populus balsamifera* L.) cuttings were taken from the river valley, adjacent to the University of Alberta, Edmonton, Canada (53°31'45.06"N, 113°31'2.88"W) on March 29th, 2017. Cuttings of 10cm length were prepared as described by DesRochers & Thomas (2003). Cuttings originated from the separate branches of trees connected to the same root stock (thus, the genetic origin was from a single parent plant). Briefly, cuttings were soaked in tap water for two days (water was replaced between each day). Cuttings were then transferred to an equal part perlite, vermiculite, Sunshine soil mix #4 (Sun Gro Horticulture, Agawam, Massachusetts, USA). Plants were allowed to break bud within a growth chamber set at 18 - 21°C and a 16h photo period for 54 days before being transferred to a greenhouse (18 - 30°C) for the rest of the growing season. On August 31st, 2017, plants of approximately 1.3M height were transferred to an outside growing area for their overwintering dormancy period. On January 15th, 2018 these overwintered plants were re-potted in fresh Sunshine Soil Mix #4 and transferred to a temperature-controlled growth chamber with 19° and 21°C night/day temperatures, respectively, and a 16hr photoperiod. Photosynthetic photon flux was 363 umol $m^{-2}s^{-1}$.Trees were well watered on a daily basis, and a 20-8-8 NPK fertilizer at 200ppm was applied on a biweekly basis. Experimental sampling began on April 26th, 2018.

b. Cold block experiment

An aluminum cold block 10mm x 10mm x 13mm (l x w x h) was fabricated from the University of Alberta Physics Machine Shop to encapsulate a small section of stem (Fig. 3-1a). The block was divided into two symmetrical pieces so that it could be easily placed and removed from the intact test stem. Each side of the block had 5mm holes drilled out for the passage of room temperature or cold water to pass through. Three blocks in total were designed to accommodate 3, 4 or 5mm diameter stems. The block was fastened in the middle of the internode region (Fig.

3-1b) of the stem. Thermal paste (Céramique, Arctic Silver Inc.,Visalia, California, USA) was applied to the stem to allow for good thermal contact between the stem and cold block. To ascertain the temperature experienced at the cold block, a thermocouple wire was inserted into the cold block contacting both the stem and block (blue wire, Fig. 3-1b). Two small screws were used to tighten the block to the stem. Inlet and outlet plastic tubing was used to deliver water to and from the cold block. A submersible pump (Algreen Products, Cambrige, Ontario, Canada) with a rate of 757 liters per hour was used to pump water into the block from a small reservoir of either room temperature or ice water. Temperature values were recorded for the warm and ice water reservoirs as well as cold block (Table 3-1). A stop-cock was used to quickly change water flow from room to ice water reservoirs or visa-versa.

Cold block measurements were carefully undertaken to minimize the chance that phloem tissue would change because of disturbance. Of crucial importance was the minimization of phloem induced disturbance via vibration. Even minor shaking may cause the cessation of phloem transport (Jaeger et al. 1988a). Thus, any measurements taken in the subsequent experiments were allowed to settle 60 minutes after the cold block was fastened to the stem to allow the translocation system to equilibrate to vibrational disturbance, as suggested by Pickard & Minchin (1990). During the time the cold block was fastened to the stem, care was taken that the plant was not moved or shook. To make the plant accustomed to the vibration of water moving through the cold block, room temperature water was ran through the cold block for the initial 60 minute equilibration time. After this time, cold water was run through the cold block. As the xylem and phloem are believed to be hydraulically linked, stomatal conductance measurements were taken before and after cold water was run through the block to determine best sampling times for subsequent experiments.

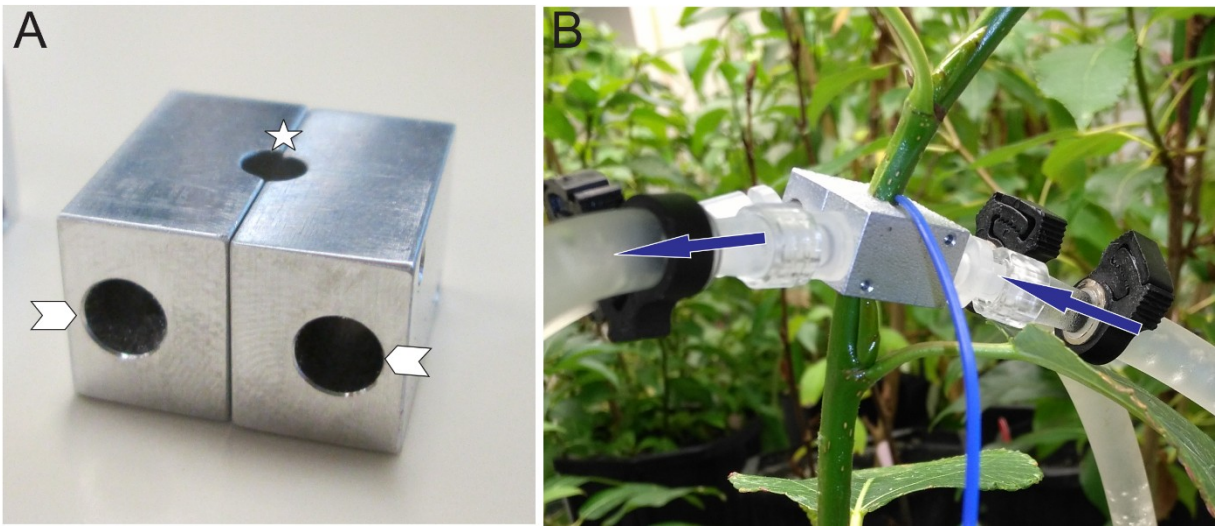

Figure 3-1: Aluminum cold block used in experiments. (A) The block was designed in two symmetrical pieces for easy removal from plant stems of diameters 3, 4, or 5mm (location of stem insertion, star). Two holes on each subunit were connected to plastic tubing to allow for either room temperature or chilled water to pass through (arrowheads). (B) The cold block was inserted between the internode region on the stem of the test plant. A thermocouple wire was interested between the cold block and stem to assess the temperature of the cold block which was in direct contact with the stem (blue wire). The plastic tubing would deliver water to each subunit of the block (blue arrows, direction of water flow).

Table 3-1: Overall mean temperatures +/- Standard Error (SE) recorded for cold block experiments. Averages are from stomatal conductance, mRNA and immunohistochemistry experiment collections. N = 1242.

	Room Temp. Reservoir (°C)	Ice Water Reservoir (°C)	Room Temp. Block (°C)	Chilled Cold Block (°C)
Mean +/- SE	20.76 +/- 0.06	2.40 +/- 0.08	21.07 +/- 0.06	4.98 +/- 0.06

Stomatal conductance measurements were taken using a SC-1 Porometer (Decagon Devices, Pullman, Washington, United States) for N = 24 test plants. For each plant, conductance measurements were taken every five minutes on the distal leaf located closest to the cold block (Fig. 3-1b). A total of 12 measurements were taken during the initial 60 min equilibration time (room temperature), after which cold water was run through the block. Another 12 measurements were taken for 55 mins after cold block application. The data for these measurements is summarized (Fig. 3-2). The average stomatal conductance was calculated for each plant prior to cold application. The conductance value for each time sampled after cold application was then subtracted by this average pre-cold conductance value and converted to an absolute value. These stomatal conductance measurements, in addition to phloem pressure response times generated from the Gould et al. (2004) study were used to justify sampling times for immuno-labeling and mRNA analysis. Our results indicated that deviation of stomatal conductance relative to pre-pretreatment levels peaked after 5 mins of cold application. In addition, pressure drop measurements from Gould et al. (2004) showed that a phloem translocation stoppage occurred during the first two minutes of cold block application. According to our results, after 10 mins of stem cooling, stomatal conductance fell closer to pre-chilled levels, and according to Gould et al. (2004), so did pressure. Previous cold block studies also have shown a recovery of translocation after the stem was rewarmed to pre-chill temperatures. Therefore, four temperature treatments were established for use in immunolabeling and mRNA expression sampling. These treatments were, (1) control treatment: 60 min room temperature water, (2) 2 min chill: 60 min room temperature followed by 2 min cold water, (3) 10 min chill: 60 min room temperature followed by 10 min cold water and (4)

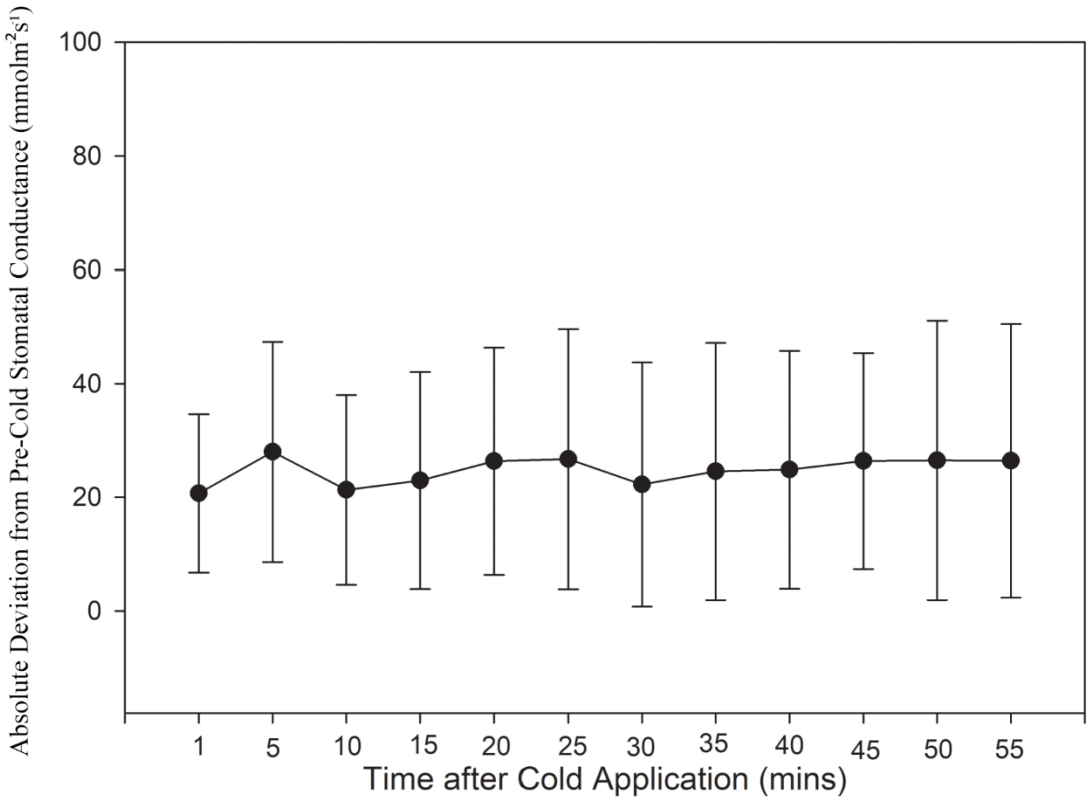

Figure 3-2: Stomatal conductance measurements after application of cold block. Each point within the series represents the absolute difference between the average pre-chilled and post-chilled stomatal conductance at each time. The time of 5 mins after cold application was observed to have the largest absolute deviation of stomatal conductance from pre-cold stomatal conductance. Bars represent Standard Deviation (SD). N = 24 plants.

rewarm: 60 min room temperature, and then 10 min cold, followed by 10 min room temperature water.

c. Fixative and RNA later solutions

Two solutions were made for preserving cellular structures for immuno-labeling or mRNA analysis. For immuno-labeling, stem samples were kept in chilled Formalin Acetic Acid (FAA). For mRNA analysis, stem samples were kept in homemade RNA later solution; solution was made by adding 117g of ammonium sulfate, 5.56ml of 0.75M sodium citrate, 6.67 ml of 0.5M EDTA adjusted to a pH of 5.2 in 250ml of nuclease free water.

d. Sampling for immunolabeling and mRNA expression

Sampling for each tree occurred between 11:00-11:30 hrs each day over an 86-day period between April 24th, 2018 and July 13th, 2018. The location of the sampling on the tree occurred at the precise location of where the cold block was applied to the stem (ie., 13mm of stem covered by the block). After the treatment time was completed, the cold block was carefully and quickly removed. The stem was then quickly cut below the nearest basal leaf, and then the section of stem with the cold block was trimmed using a fresh razor blade. This 13mm stem section was cut in half and dropped into one of two solutions a) 4°C chilled FAA for immuno-labeling or b) RNA later for mRNA expression data. After 30 mins, samples for immuno-labeling were changed into fresh chilled FAA, and once more after 6 hours. Samples for mRNA analysis were transferred to a -20°C freezer until the start of qtPCR. For immuno-labeling a total of 6 control and 4 plants from each experimental treatment were examined, for a total of 18.

e. Sectioning and immunolabeling

Stem sections were kept in FAA fixative for at least 72 hours prior to embedding. Organs were then paraffin embedded in a Leica TP 1020 tissue processor (Leica Microsystems, Wetzlar, Germany) before going into wax block molds. Longitudinal or transverse sections of 7µm thickness were made on a rotary microtome and transferred directly onto Probe-on Plus (Fisher Scientific, Pittsburgh, Pennsylvania) slides flooded with deionized water. Slides were kept on a hotplate set to 50°C until sections flatted out on the water and then placed in a drying oven for at least 24 hours at 37°C.

Immuno-labeling was performed following the methodology of Gong et al. (2006) and has been previously described in Stanfield et al. (2017). To summarize, slides were dewaxed in Safeclear® Xylene Substitute (Fisher Scientific), rehydrated in an ethanol series and then washed in phosphate buffered saline (PBS). After a step in post-fixative and another wash in PBS, slides were transferred to blocking solution (BS) and then washed briefly in low-salt water washing buffer (LWB) before primary antibodies were applied. Approximately 80 – 100µl of *At*PIP1;3 and PIP2 aquaporin antibodies were applied to slides which have confirmed reactivity in balsam poplar according to Western Blot analysis (as used in Stanfield et al. 2017). After 16 – 24h of incubation at 4°C in a dark humid container, slides were washed in LWB and secondary antibodies applied. Approximately 80 – 100µl of Pre-absorbed [1/500] Alexa Fluor (Fisher Scientific) 488 conjugated goat anti-mouse and Alexa Fluor 568 conjugated goat anti-chicken were applied to slides for 2h at 37°C. Secondary antibodies were then removed with LWB, quickly washed in double distilled H_2O and mounted in Slow Fade Gold (Fisher Scientific). Cover slips were sealed-in using nail polish.

f. Microscopy and image analysis

Confocal microscopy was performed on a Zeiss LSM 700 (Carl Zeiss AG, Oberkochen, Germany) operated on Zen Black 2011 edition software. A 63x oil immersion lens was used to capture images. Laser power was set to 5.5% to excite Alexa Fluor 488 (PIP2) and to 2% to excite Alexa Fluor 568 (PIP1). Camera gain was 700 for both color channels and pinhole diameter was set to 1 Airy unit.

Image analysis was carried out using Image-Pro Premier Version 9.2 (Media Cybernetics, Rockville, Maryland). Transverse section images from each sampled tree were analyzed to view sieve elements. Sieve elements within each image were manually traced based upon their PIP2 outline. The use of software allowed for three main types of data to be collected for highlighted sieve elements: (1) average signal intensity (luminance µm), (2) internalization of aquaporin signal and (3) sieve element area (μm^2). Internalization of aquaporins was a categorical value (i.e., sieve element appearing with mostly internalized aquaporin signal) which was determined using the margination and heterogeneity tools of Image Pro (as performed in Stanfield et al. 2017). Generally, if sieve elements had a margination values ≤0.56 they were classified as having an internalized aquaporin signal; conversely if the value was >0.56 their aquaporin signal was classified as membrane bound.

g. qrtPCR analysis

Gene transcript measurements by quantitative real-time PCR Sections of stem segments corresponding to the cold block application (~15mm) were collected and submerged in RNAlater stabilisation solution (Ambion, USA) until further processing. Samples were always collected between 10:00 h and 11:30 h to minimize any diurnal effect on AQP expression.

Under a binocular microscope, > 40mg of phloem-enriched tissue was dissected by peeling off the interior layer of epidermal peels using fine forceps. Control tissue containing the remaining epidermis and the xylem tissue was also stored at -80°C. Total RNA was extracted using the CTAB method of Pavy et al. (2000). RNA quality was assessed on an agarose gel and quantified with a spectrophotometer (Nanodrop ND-1000, Thermo Scientific, Wilmington, DE, USA). RNA was treated as previously described (Laur and Hacke, 2014). Putative stem-expressed AQP genes were selected, PtPIP1;1 (Potri.010G191900), PtPIP1;4 (Potri.006G098100) and PtPIP2;4 (Potri.008G039600) (Wilkins et al., 2009), and specific primers (data not shown) were designed using the QuantPrime online tool (Arvidsson et al., 2008). PCR efficiency was 100% for all primer pairs and specificity was checked using melting curves. Real-time qPCR was performed on a Applied Biosystems viiA™ Real-Time PCR system (Applied Biosystems, Foster City, CA, USA). Relative gene expression was measured according to Livak & Schmittgen (2001) using the 2-ΔΔCT method. The expression values were normalized to the housekeeping gene Elongation Factor 1B (Potri.001G224700; Brunner et al., (2004)). Relative gene expression was determined as the fold change of an AQP isoform at a given condition relative to its expression under control conditions. Real-time PCR was carried out using three biological replicates each with three technical replicates.

h. Data analysis

A one factor ANOVA was used to determine if a significant difference between cold block treatments existed from the response variables of signal intensity, aquaporin internalization and sieve element area. Multiple comparisons were made for outcomes determined to be significantly different ($p < 0.05$) using the Tukey Test. Sigma Plot Version 13.0 (Systat Software, San Jose, California) was used to compute all statistical tests.

3. Results

Visually, immunolabeling of the stem organ sieve elements in cross sectional view appeared to have different intensities (Fig. 3-3). The overall phloem area can be seen stained with aniline blue (Fig. 3-3a). For antibody labeled specimens, a primary antibody control (no primary antibody applied) showed only background fluorescence using confocal microscopy (Fig. 3-3b). In contrast, the four experimental treatments showed various intensities of PIP1 (red) and PIP2 (green) (Figs. 3-3c-f). Of interest were the moderate aquaporin intensities of the control and rewarm treatment (Figs. 3-3c & f). In contrast to these the 2 min chill treatment (Fig. 3-3d) had very intense antibody signals whereas the 10 min chill treatment had markedly diminished signal (Fig. 3-3e). To ascertain if there was a quantitative difference in antibody labeling between treatments, image analysis was performed on 30 images taken from each sampled tree from each treatment (N = 18).

Quantitative intensities of the PIP2 signal were significantly greater in the 2 min chill treatment than the control and 10 min chill treatment (Fig. 3-4a; $DF = 17$, $F = 5.273$, $p < 0.05$). Additionally, the 10 min chill treatment had a 1.6-fold lower antibody signal than the control treatment and was on average 3.1-fold less than the 2 min chill treatment. In contrast, the rewarm treatment was not significantly different from the other treatments. Comparing the ratio of PIP2:PIP1 signal intensity, there was no significant difference found between treatments (Fig. 3-4b; $DF = 17$, $F = 0.717$, $p \geq 0.05$). Visually, the area of individual sieve elements appeared to be greatest in the 10 min chill treatment (Fig. 3-3e), however no significant difference in area was detected between treatments (Fig. 3-4c; $DF = 17$, $F = 2.362$, $p \geq 0.05$). Although there was a trend towards greater internalization of aquaporins from the plasma membrane to internal

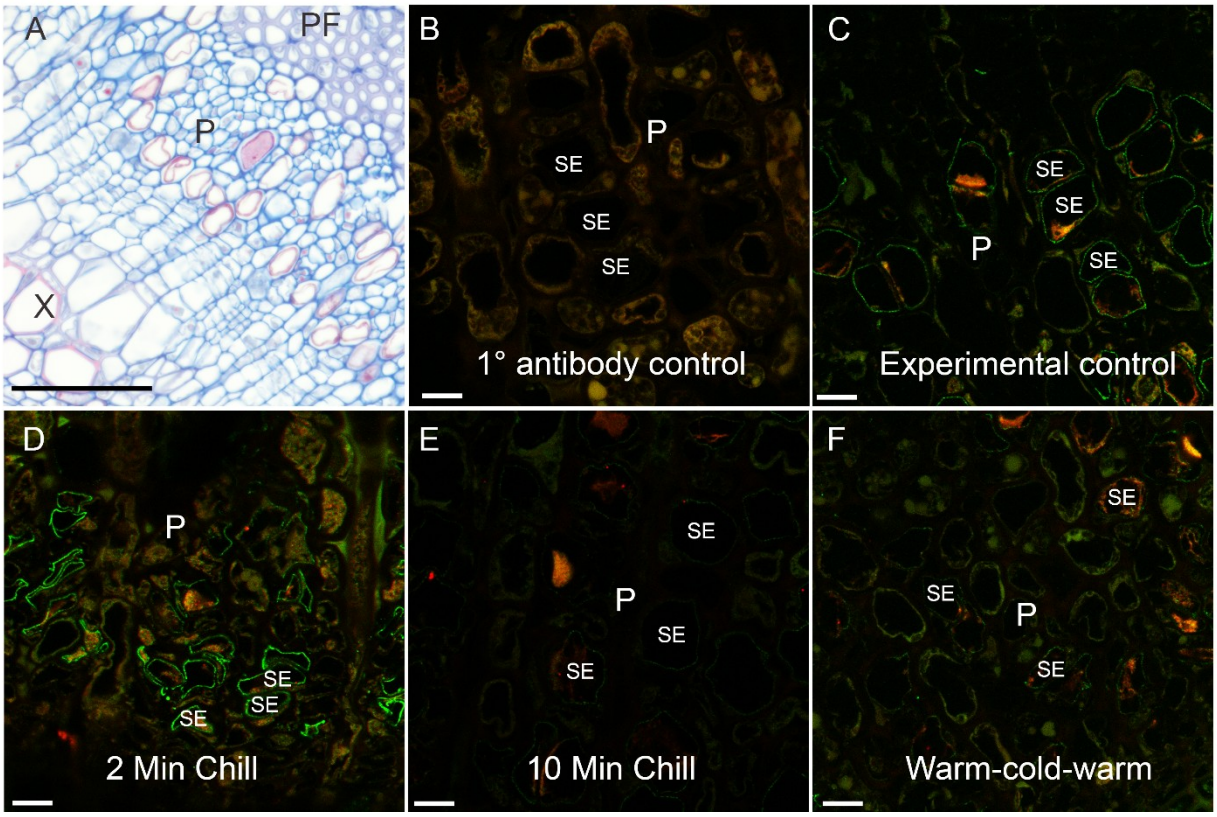

Figure 3-3: Representative phloem bright field and confocal micrographs showing PIP1 and PIP2 aquaporin labeling following cold block treatments. (A) Cross section of stem tissue showing phloem region (P) in-between phloem fibers (PF) and xylem (X). Phloem is stained using aniline blue. (B – F) Confocal laser scanning micrographs of phloem tissue from various cold block experimental treatments. Red channel = PIP1 labeling, green channel = PIP2 labeling. (B) Background fluorescence of the 1° antibody control. (C) Experimental control treatment (no cold application). (D) Two-minute cold application. (E) Ten-minute cold block application. (F) Ten-minute application of room temperature water following 10 minutes of cold application and finally 10 minutes of room temperature water. Scale bars: (A) 60 µm, (B – F) 10µm.

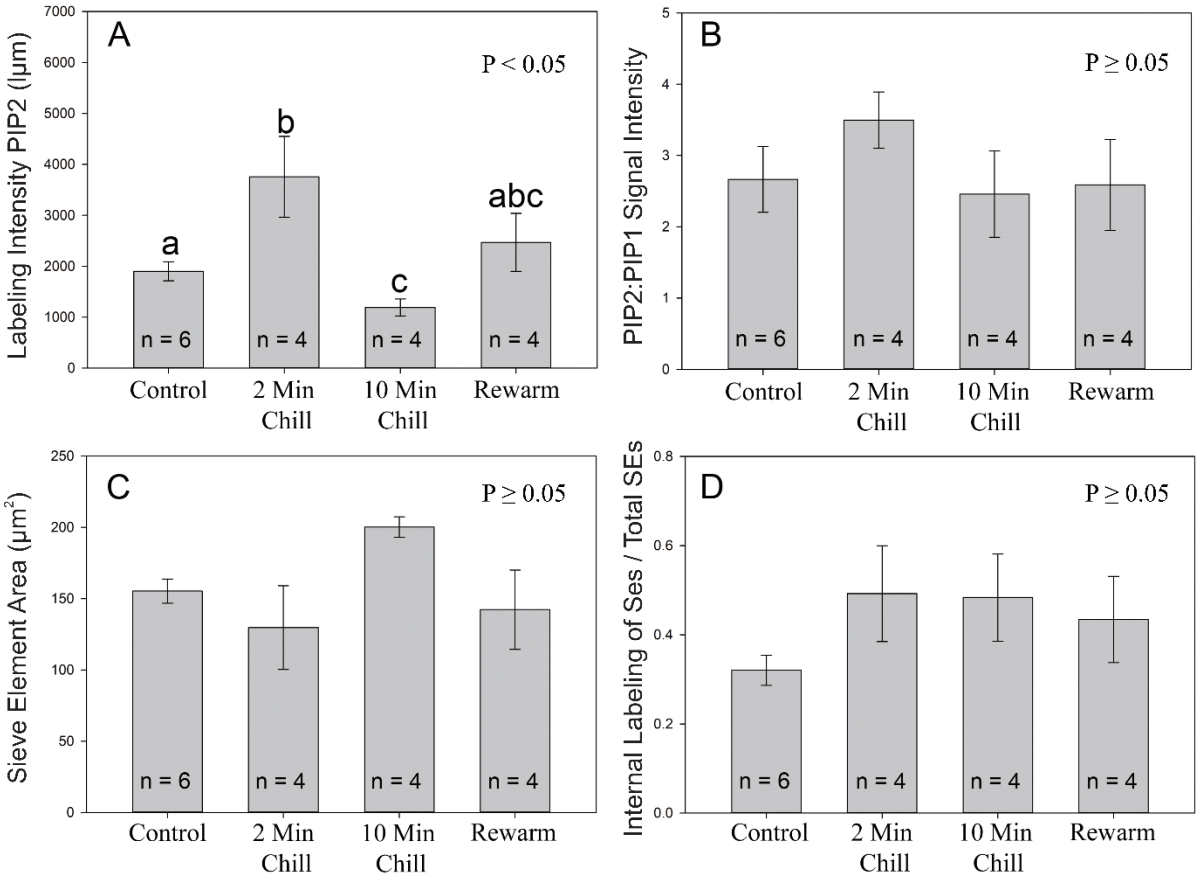

Figure 3-4: Image analysis of aquaporin labeling from the four experimental cold-block treatments. (A) A measure of the pixel signal intensity (luminance micrometers) using the mean intensity value tool in Image Pro software was used for highlighted sieve elements labeled with PIP2 aquaporins. The 2 min chill treatment had significantly greater intensity values than the control and 10-minute treatments (1-way ANOVA). Different letters indicate a significant difference ($p < 0.05$) between treatments (Tukey-Test). (B) Ratio of PIP2:PIP1 intensity values of highlighted sieve elements. No significant differences were found between treatments. (C) Mean area of individual sieve elements. No significant difference found between treatments (D) The proportion of sieve elements, on average, which were categorized as having an overall internalization of PIP1 and PIP2 aquaporins. No significant difference found between treatments. Values shown are means +/- standard error (SE).

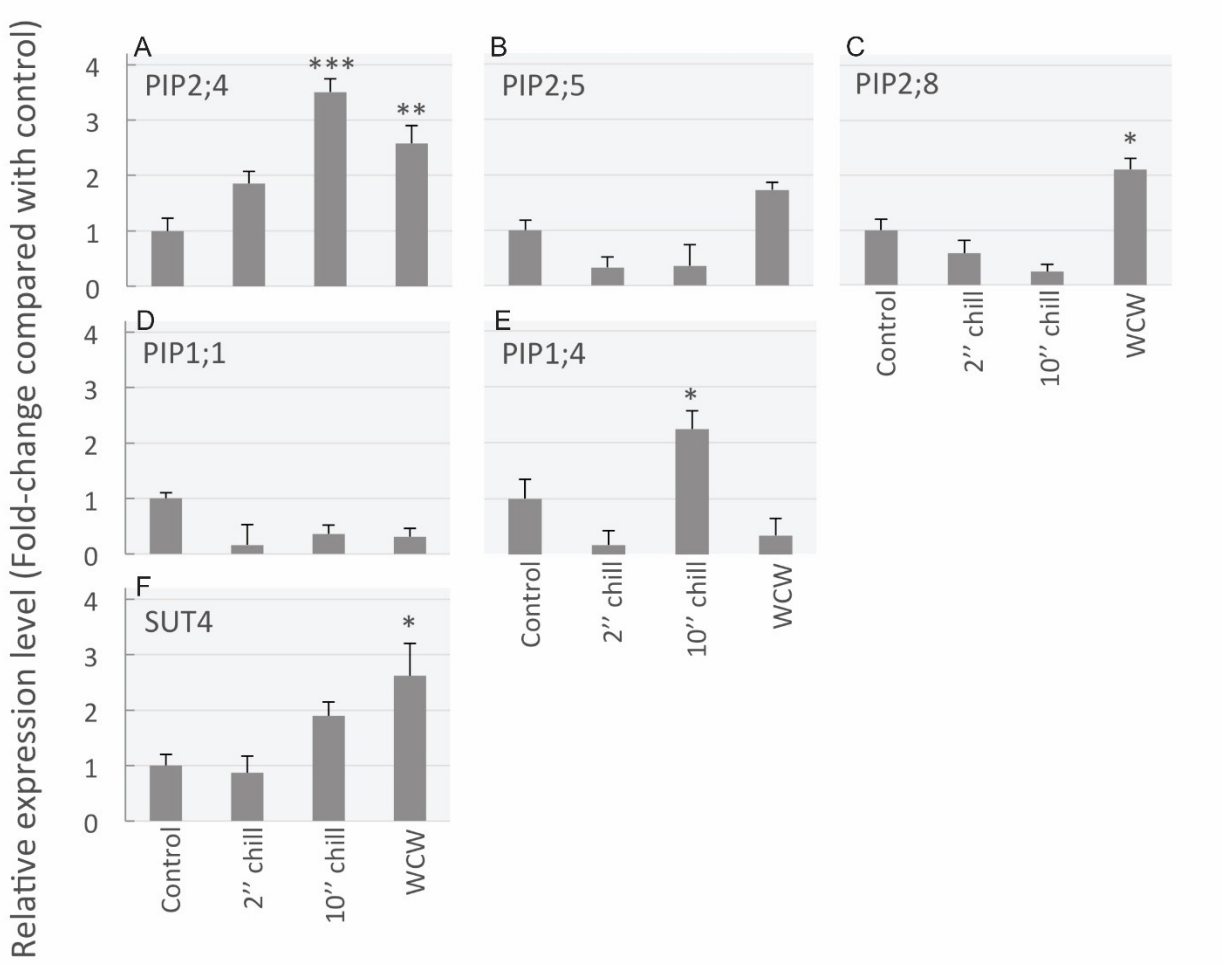

Figure 3-5: Results from qrtPCR mRNA transcript abundance analysis for 5 aquaporin genes and one sucrose transporter gene in stem samples from the following four cold block treatments: control, 2 min chill, 10 min chill and rewarm after chilling (WCW). (A) PIP2;4 transcript significantly increased after 10 min chill and rewarming treatments in comparison to control treatments. (B) PIP2;5 did not significantly change between treatments. (C) For PIP2;8, the rewarming treatment had significantly greater transcript abundance over the controls. (D) PIP1;1 did not show significantly different transcript abundance between treatments. (E) For the PIP1;4 isoform, transcript abundance declines for the 2 min chill treatment, whereas it significantly increased for the 10 min chilling treatment. (F) The sucrose transporter SUT4 was shown to have significantly higher transcript abundance for rewarming treatment in comparison to the control. Asterisks denote significant differences in expression level compared to control levels (one-way ANOVA, followed by Tukey HSD post-hoc test, * P<=0.05; ** P<=0.01*** P<=0.001). Data are means + standard error (SE) of three biological replicates.

membranes in the experimental treatments vs. the control, no significant difference was found (Fig. 3-4d; DF = 17, F = 1.138, $p \geq 0.05$).

Using qrtPCR analysis, mRNA transcript abundance was assessed between the different cold block treatments (Fig. 3-5). A total of five PIP aquaporin genes and one sucrose transporter (SUT) gene was measured. The reference transcript abundance among the four treatments was made relative to the control (i.e., control transcript abundance was always 1). Overall, PIP2;4 showed the most significant treatment effect as it significantly increased 3-fold in comparison to controls for the 10 min chilling treatment and also saw a more than 2.5 fold increase for the rewarming treatment (Fig. 3-4A). Although PIP2;5 did show a nearly 2-fold increase for the rewarming treatment, this was not statistically significant (Fig. 3-4B). In comparison PIP2;8 showed a significant 2-fold increase over controls for the rewarming treatment (Fig. 3-4C). In comparison to the PIP2s, PIP1s overall did not increase substantially in response to the cold (Fig. 3-4D & E). However, the PIP1;4 gene did show a significant gain of over 2-fold for the 10 min chilling treatment (Fig. 3-4E). Finally, the sucrose transporter tested, SUT4, showed a significant ~2.5 fold increase for the rewarming treatment in comparison to the control (Fig. 3-4F).

Discussion

a. PIP2 signal increases substantially following cold treatment, then declines

The immunolabeling experiments showed a significant increase in labeling intensity for PIP2 proteins 2 mins after cold was applied. However, after 10 mins, aquaporin labeling intensity dropped significantly to lower than that of the controls. In chilling tolerant maize lines, leaves exposed to chilling temperatures of 12°C showed an increase in PIP2;3 aquaporin labeling density within sieve tubes after 28hrs of cold exposure relative to controls (Bilska-Kos,

Szczepanik & Sowiński 2016). In contrast, the chilling sensitive line of maize leaves showed a decline in PIP2;3 density in thick walled sieve tubes relative to controls according to their TEM analysis. In a separate study, it was found that maize roots exposed to 5°C chilling for 3 days showed a significant increase in PIP2 protein abundance according to immunoblot intensity (Aroca et al. 2005). In rice roots subjected to a 10°C chill for one day, *Os*PIP2;5 protein abundance increased by ~30% in comparison to controls, according to SDS-page results (Ahamed et al. 2012). These prior studies show an increase in protein abundance and/or labeling following a long duration chilling regime. In contrast, the current study sees this increase much more rapidly. This could mean aquaporin response to chilling is much quicker than previous researchers have reported. The quick aquaporin response could be in part due to a tissue level response to control hydraulic conductivity. The effect of chilling causes a greater amount of water stress at both the root (Ahamed et al. 2012) and leaf level (Bilska-Kos, Szczepanik & Sowiński 2016, Sack, Streeter & Holbrook 2004). This stress is a result of not only viscosity increases that inhibit root water update, but also from the decline in the hydraulic conductivity of plasma membranes. The loss of hydraulic conductivity due to chilling may be a result of decreased fluidity of the plasma membrane (Alonso, Queiroz & Magalhães 1997). Thus, the uptick in PIP2 aquaporin protein signal within sieve tubes observed in the current study could be to counteract inadequacies of the plasma membrane to transfer water via passive diffusion.

Apart from a direct response to cold, the aquaporins in sieve tubes could also be responding to pressure. Sieve tubes experience a transient build-up in pressure following cold block application (Gould, Minchin & Thorpe 2004). Workers found that after 2 mins of cold block application there was a >2-fold pressure increase inside sieve tubes of cow thistle, and a complete stoppage of translocation. However, translocation began to resume after 8 – 10 mins of

cold application and pressure began to return to pre-chill levels. Similarly, in the current study we found that aquaporin signal intensity was maximized after only 2 mins of cold application, but then fell to lower than that of control plants after only 10 mins of chilling. Aquaporins are hypothesized to respond mechanically to high pressure by closing (Luu & Maurel 2005, Chaumont & Tyerman 2014a). It could be that aquaporins were responding to decreased hydraulic conductivity at the individual pore level by upregulating their abundance. Concomitantly, the cold application itself could have had its own independent effect on increasing aquaporin proteins in sieve tube plasma membranes. This double effect of cold and pressure may have caused an overshoot of protein abundance quickly following the cold application, causing aquaporin signal intensity in sieve tubes to fall below their pre-chill treatment levels after 10 mins of chilling. After 10 mins of rewarming, PIP2 aquaporin protein signal level resumed to their prior pre-chill level, which may infer that normal translocation resumed. Future studies are needed to parse out the contribution due to mechanical and cold induced changes in aquaporin expression within sieve tubes.

Thus, we accept our hypothesis that aquaporin protein abundance in the plasma membrane increases in response to a perceived chilling blockage event. However, we must reject our hypothesis that the localization pattern of aquaporins change in response to cold as we did not find a significant treatment effect of plasma membrane: internally located aquaporins. Future work may use super-resolution microscopy to resolve the fine detail of PIP localization that may occur within sieve tubes following a disturbance.

b. mRNA transcript abundance changes depending upon chilling treatment

Although the protein expression patterns provide an explanation of how sieve tube plasma membranes respond to an increase in pressure via chilling, mRNA analysis portrayed a more

complicated picture. Overall in the current study we found that mRNA for PIP1 isoforms were downregulated upon cold treatment, except for PIP1;4 which showed a 2-fold increase after 10mins of chill time. In contrast, PIP2;4 showed a much greater transcript abundance post chilling application, reaching its maximum 10min after chilling. Thus, we may only partially accept our hypothesis that aquaporin genes are upregulated following a cold event. At face value, this appears to be the opposite of the immunolabeling results which first show a strong increase after 2 mins, but then a steep decline in PIP2 signal intensity 10 mins into chilling. However, Aroca (2005) also showed that while PIP1 and PIP2 protein abundance increased after cold in maize roots, mRNA expression levels declined. This shows that mRNA transcript and protein abundance need not be correlated with one another and that control of the two macromolecules fall under complex regulation.

In addition to mRNA levels responding differently to protein level expression, the timing of regulation may vary for different PIP genes. For example, changes in mRNA expression may be slower than changes at the protein level. In one example in response to salt stress, PIP transcript levels took between 2-4 hours to decline, whereas changes in protein abundance occurred within 30 mins (Chevalier & Chaumont 2015). In addition, the time of exposure to cold may impact the expression of PIP genes differently. In a chilling experiment involving the roots of *Arabidopsis*, it was found that the overexpression of PIP1;4 and PIP2;5 in mutant plants counteracted root loss of cellular hydraulic conductivity (Lee et al. 2012). Expression levels in the roots for aquaporin gene PIP2;5 only increased significantly after 24hrs of total chilling. In contrast for PIP1;4, there was a significant increase in transcript abundance after 1hr and 24hrs of chilling. However when these researchers extended the chilling time to 5 days, mutants overexpressing PIP1;4 showed a loss of hydraulic conductivity in comparison to PIP2;5 mutants which retained their increased

hydraulic conductivity. These results indicate that PIP genes respond differently to cold stress. The mechanism for why this could be may be due to the differing roles of PIP1 and PIP2 genes.

The role of PIP1 and PIP2 aquaporins may be functionally different. Whereas PIP2 serves primarily as a water channel (Yaneff, Vitali & Amodeo 2015), PIP1 may serve to transport other molecules such as CO_2 (Uehlein et al. 2008) or O_2 (Zwiazek et al. 2017). A preponderance of studies (see Yaneff et al. 2015 for a review) show that PIP1 has a much lower ability to transport water than PIP2, and that localization studies often find PIP1 within internal membranes rather than the plasma membrane. This finding of internal PIP1 localization has been documented in sieve tubes (Stanfield et al. 2017) and points to the idea that PIP1 has a regulatory role rather than a primary water transport role in plant plasma membranes. One regulatory mechanism PIP1 may possess is the ability to modulate the activity of PIP2. Previous results indicate that PIP isoforms show synergistic relationships with one another, with differing ratios of PIP1 and PIP2 subunits within heterotetramers having contrasting effects on the membrane permeability of measured oocytes (Fetter et al. 2004). For example, *Zm*PIP1;2 and *Zm*PIP2;5 increased membrane permeability by 2-fold in comparison to when *Zm*PIP2;5 was inserted into oocytes by itself. This enhancement of the water transporting capacity of PIP2;5 was only maintained when inserting excess PIP1;2 into the oocyte while the addition of PIP1;1 did not show a synergistic effect.

Thus it is possible that only certain combinations of PIP1 and PIP2 isoforms garner a synergistic effect, which may change how transcript abundance data is interpreted in response to an abiotic stress event. In the current study, we may speculate that PIP1;4 increased significantly after chilling to bolster the effects of the water transporting aquaporin PIP2;4. However, this effect has yet to be tested. As suggested by Yaneff et al. (2015), it is important to test many

combinations of PIP1 and PIP2 genes for their potential synergies. In addition, protein level modifications as well as cellular localization may play an even more important role in determining the response of aquaporins to environmental stress. Future studies will need to verify the downstream consequences of different combinations of aquaporin transcript abundance on their impact to control cellular water permeability.

c. Conclusions

In the current study we found there to be an increased signal of PIP2 aquaporins in sieve tubes membranes after 2 mins of chilling. This response mirrors what has been found physiologically when a stem segment is subjected to cold which causes sieve tubes to experience a transient increase in pressure, presumably due to a blockage event. The results of this study provides a mechanism for pressure release following cold application. Potentially, upregulation of PIP2 protein abundance in the plasma membrane of sieve tubes acts a pressure release valve following cold block application. Once flow is resumed, aquaporin abundance is then quickly adjusted in the plasma membrane to maintain an adequate pressure profile in the sieve tube. We also found that while the upregulation of mRNA gene expression does not match up with the timing of protein signal change within sieve tubes, the two need not necessarily be linked. Likely it is protein level modification which acts to more immediately rectify disturbances in cellular water balance. Later, altered mRNA transcript abundance could then impact protein level accumulation in plasma membranes of effected cells. This relationship between mRNA transcript abundance and protein expression following cold will need to be tested in future studies. Although it is still not clear what causes sieve tubes to become blocked following cold, the plasma membrane likely has a role in regulating the release and retrieval of both water and sugar following a disturbance to maintain proper pressure gradients.

4. References

Ahamed A., Murai-Hatano M., Ishikawa-Sakurai J., Hayashi H., Kawamura Y. & Uemura M. (2012) Cold stress-induced acclimation in rice is mediated by root-specific aquaporins. *Plant and Cell Physiology* 53, 1445-1456.

Alonso A., Queiroz C.S. & Magalhães A.C. (1997) Chilling stress leads to increased cell membrane rigidity in roots of coffee (coffea arabica L.) seedlings. *Biochimica Et Biophysica Acta (BBA)-Biomembranes* 1323, 75-84.

Aroca R., Amodeo G., Fernández-Illescas S., Herman E.M., Chaumont F. & Chrispeels M.J. (2005) The role of aquaporins and membrane damage in chilling and hydrogen peroxide induced changes in the hydraulic conductance of maize roots. *Plant Physiology* 137, 341-353.

Arvidsson, S., Kwasniewski, M., Riaño-Pachón, D. M., & Mueller-Roeber, B. (2008). QuantPrime–a flexible tool for reliable high-throughput primer design for quantitative PCR. *BMC bioinformatics 9*, 465.

Bilska-Kos A., Szczepanik J. & Sowiński P. (2016) Cold induced changes in the water balance affect immunocytolocalization pattern of one of the aquaporins in the vascular system in the leaves of maize (zea mays L.). *Journal of Plant Physiology* 205, 75-79.

Brunner, A. M., Yakovlev, I. A., & Strauss, S. H. (2004). Validating internal controls for quantitative plant gene expression studies. *BMC plant biology 4*, 14.

Chaumont F. & Tyerman S.D. (2014) Aquaporins: Highly regulated channels controlling plant water relations. *Plant Physiology 164*, 1600-1618.

Chevalier A.S. & Chaumont F. (2015) Trafficking of plant plasma membrane aquaporins: Multiple regulation levels and complex sorting signals. *Plant & Cell Physiology* 56, 819-829.

Chisholm S.T., Parra M.A., Anderberg R.J. & Carrington J.C. (2001) Arabidopsis RTM1 and RTM2 genes function in phloem to restrict long-distance movement of tobacco etch virus. *Plant Physiology 127*, 1667-1675.

Comtet J., Jensen K.H., Turgeon R., Stroock A.D. & Hosoi A.E. (2017) Passive phloem loading and long-distance transport in a synthetic tree-on-a-chip. *Nature plants 3*, 17032.

Comtet J., Turgeon R. & Stroock A.D. (2017) Phloem loading through plasmodesmata: A biophysical analysis. *Plant Physiology 175*, 904.

DesRochers A. & Thomas B. (2003) A comparison of pre-planting treatments on hardwood cuttings of four hybrid poplar clones. *New Forests 26*, 17-32.

Fetter K., Van Wilder V., Moshelion M. & Chaumont F. (2004) Interactions between plasma membrane aquaporins modulate their water channel activity. *The Plant Cell 16*, 215-228.

Froelich D.R., Mullendore D.L., Jensen K.H., Ross-Elliott T.J., Anstead J.A., Thompson G.A., Pélissier H.C. & Knoblauch M. (2011) Phloem ultrastructure and pressure flow: Sieve-element-occlusion-related agglomerations do not affect translocation. *The Plant Cell 23*, 4428-4445.

Geiger D.R. & Sovonick S.A. (1975) Effects of temperature, anoxia and other metabolic inhibitors on translocation. In: *Transport in Plants I*, pp. 256-286, Springer, Berlin, Heidelberg.

Giaquinta R.T. & Geiger D.R. (1973) Mechanism of inhibition of translocation by localized chilling. *Plant Physiology 51*, 372-377.

Gong H., Peng Y., Zou C., Wang D., Xu Z. & Bai S. (2006) A simple treatment to significantly increase signal specificity in immunohistochemistry. Plant Molecular Biology Reporter 24, 93-101.

Gould N., Minchin P.E.H. & Thorpe M.R. (2004) Direct measurements of sieve element hydrostatic pressure reveal strong regulation after pathway blockage. *Functional Plant Biology 31*, 987-993.

Jaeger C.H., Goeschl J.D., Magnuson C.E., Fares Y. & Strain B.R. (1988) Short-term responses of phloem transport to mechanical perturbation. *Physiologia Plantarum 72*, 588-594.

Julia Kehr & Anja Buhtz. (2008) Long distance transport and movement of RNA through the phloem. *Journal of Experimental Botany 59*, 85-92.

Kammerloher W., Fischer U., Piechottka G.P. & Schäffner A.R. (1994) Water channels in the plant plasma membrane cloned by immunoselection from a mammalian expression system. *The Plant Journal: For Cell and Molecular Biology 6*, 187-199.

Lang A. & Minchin P. (1986) Phylogenetic distribution and mechanism of translocation inhibition by chilling. *Journal of Experimental Botany 37,* 389-398.

Lee, S. H., Chung, G. C., Jiang, J. Y., Ahn, S. J., & Zwiazek, J. J. (2012). Overexpression of PIP2; 5 aquaporin alleviates effects of low root temperature on cell hydraulic conductivity and growth in *Arabidopsis thaliana*. *Plant Physiology 159*, 479-488.

Luu D. & Maurel C. (2005) Aquaporins in a challenging environment: Molecular gears for adjusting plant water status. *Plant, Cell & Environment 28*, 85-96.

Laur, J., & Hacke, U. G. (2014). The role of water channel proteins in facilitating recovery of leaf hydraulic conductance from water stress in Populus trichocarpa. *PloS one*, *9*, e111751.

Livak KJ, Schmittgen TD (2001) Analysis of relative gene expression data using real-time quantitative PCR and the 22DDCT method. *Methods 2*, 402–408.

Marjanović, Ž., Uehlein, N., Kaldenhoff, R., Zwiazek, J. J., Weiß, M., Hampp, R., & Nehls, U. (2005). Aquaporins in poplar: what a difference a symbiont makes! *Planta 222*, 258-268.

Maurel C., Boursiac Y., Luu D., Santoni V., Shahzad Z. & Verdoucq L. (2015) Aquaporins in plants. *Physiological Reviews 95*, 1321-58.

Maurel C., Reizer J., Schroeder J.I. & Chrispeels M.J. (1993) The vacuolar membrane protein gamma-TIP creates water specific channels in xenopus oocytes. *The EMBO Journal 12*, 2241-2247.

Minchin P. & Thorpe M.R. (1987) Measurement of unloading and reloading of photo-assimilate within the stem of bean. *Journal of Experimental Botany 38*, 211-220.

Minchin P. & Thorpe M.R. (1983) A rate of cooling response in phloem translocation. *Journal of Experimental Botany 34*, 529-536.

Mittler T.E. (1953) Amino-acids in phloem sap and their excretion by aphids. *Nature* 172, 207.

Muday G.K. & Brown-Harding H. (2018) Nervous system-like signaling in plant defense. *Science 361*, 1068-1069.

Mullendore D. L., Ross-Elliott T., Liu Y., Hellmann H. H., Roalson E. H., Peters W. S., & Knoblauch M. (2018). Non-dispersive phloem-protein bodies (NPBs) of Populus trichocarpa consist of a SEOR protein and do not respond to cell wounding and Ca2+. *PeerJ 6*, e4665.

Pavy N, Boyle B, Nelson C, Paule C, Gigue`re I, et al. (2000) Identification of conserved core xylem gene sets: conifer cDNA microarray development, transcript profiling and computational analyses. *New Phytol 180,* 766–86.

Pickard W.F. & Minchin P. (1990) The transient inhibition of phloem translocation in phaseolus vulgaris by abrupt temperature drops, vibration, and electric shock. *Journal of Experimental Botany 41*, 1361-1369.

Rennie E.A. & Turgeon R. (2009) A comprehensive picture of phloem loading strategies. *Proceedings of the National Academy of Sciences 106*, 14162-14167.

Ross-Elliott T.J., Jensen K.H., Haaning K.S., Wager B.M., Knoblauch J., Howell A.H., Mullendore D.L., Monteith A.G., Paultre D. & Yan D. (2017) Phloem unloading in arabidopsis roots is convective and regulated by the phloem-pole pericycle. *Elife 6*, e24125.

Sack L., Streeter C.M. & Holbrook N.M. (2004) Hydraulic analysis of water flow through leaves of sugar maple and red oak. *Plant Physiology 134*, 1824-1833.

Sasaki T., Chino M., Hayashi H. & Fujiwara T. (1998) Detection of several mRNA species in rice phloem sap. *Plant & Cell Physiology 39*, 895-897.

Sibaoka T. (1962) Excitable cells in mimosa. *Science 137*, 226.

Stanfield R.C., Hacke U.G. & Laur J. (2017) Are phloem sieve tubes leaky conduits supported by numerous aquaporins? *American Journal of Botany 104*, 719-732.

Stanfield, R. C., Schulte, P. J., Randolph, K. E., & Hacke, U. G. (2018). Computational models evaluating the impact of sieve plates and radial water exchange on phloem pressure gradients. *Plant, cell & environment*. https://doi.org/10.1111/pce.13414.

Thompson M.V. (2006) Phloem: The long and the short of it. *Trends in Plant Science* 11, 26-32.

Thorpe M.R., Furch A.C., Minchin P.E., Foeller J., Van Bel A.J. & Hafke J.B. (2010) Rapid cooling triggers forisome dispersion just before phloem transport stops. *Plant, Cell & Environment* 33, 259-271.

Törnroth-Horsefield S., Wang Y., Hedfalk K., Johanson U., Karlsson M., Tajkhorshid E., Neutze R. & Kjellbom P. (2006) Structural mechanism of plant aquaporin gating. *Nature* 439, 688.

Uehlein N., Otto B., Hanson D.T., Fischer M., McDowell N. & Kaldenhoff R. (2008) Function of nicotiana tabacum aquaporins as chloroplast gas pores challenges the concept of membrane CO2 permeability. *The Plant Cell* 20, 648-657.

Van Bel A. (2003) The phloem, a miracle of ingenuity. *Plant, Cell & Environment 26*, 125-149.

Wilkins, O., Nahal, H., Foong, J., Provart, N. J., & Campbell, M. M. (2009). Expansion and diversification of the Populus R2R3-MYB family of transcription factors. Plant Physiology *149*, 981-993.

Walz C., Juenger M., Schad M. & Kehr J. (2002) Evidence for the presence and activity of a complete antioxidant defence system in mature sieve tubes. *The Plant Journal 31*, 189-197.

Yaneff, A., Vitali, V., & Amodeo, G. (2015). PIP1 aquaporins: Intrinsic water channels or PIP2 aquaporin modulators?. *FEBS letters*, *589*, 3508-3515.

Zwiazek J.J., Xu H., Tan X., Navarro-Ródenas A. & Morte A. (2017) Significance of oxygen transport through aquaporins. *Scientific Reports 7*, 40411.

IV. Computational models evaluating the impact of sieve plates and radial water exchange on phloem pressure gradients

1. Introduction

The phloem distributes carbohydrates needed for metabolism, growth, and reproduction. The tissue is also involved in the long-distance propagation of molecular (Lucas et al. 2013) and electrical signals (Hedrich, Salvador-Recatalà & Dreyer 2016). Impairment of phloem function due to drought may lead to plant mortality (Sevanto et al. 2014, Sevanto 2018), and phloem architecture in crop plants may impact yields (Ham & Lucas 2014). Despite these essential functional roles, the sieve element is one of the least understood cell types in plants. Many questions remain unresolved as to how phloem structure relates to function (Liesche & Patrick 2017, Turgeon 2010). This has been due to the relative obscurity of the tissue for direct measurement (Van Bel 2003). However, advances in phloem tissue preparation and microscopic techniques (Mullendore et al. 2010, Froelich et al. 2011, Fitzgibbon et al. 2010) yield anatomical images which can then be integrated into computational tools used to model flow. Using these methods, we can begin to assess in more detail the structural and mechanistic details of long distance phloem transport.

Phloem transport proceeds through the lumen of interconnected sieve elements. The main obstructions in the pathway are sieve plates which occur at sieve element end walls in angiosperms (Esau & Thorsch 1985). Surprisingly, some previous models indicated that sieve plates contribute roughly equally to sap resistance in comparison to the lumen (Jensen, Mullendore, Holbrook, Bohr, Knoblauch & Bruus 2012a, Liesche et al. 2017a, Savage et al. 2017). However, other examples show conductivity reductions due to plates of up to 88% (Thompson & Holbrook 2003a). Although the lumen of sieve tubes is devoid of most organelles such as the nucleus and a central vacuole (Van Bel 2003), there are obstructions such as protein agglomerations and plastids. These may contribute to the frictional resistance to flow. While previous work suggests that these structures have limited impacts on flow (Froelich et al. 2011,

Knoblauch et al. 2014), sieve plates may reduce flow by design as a safety mechanism to prevent sap loss after injury. Sieve plate pores occlude with callose after a sieve tube is cut (Mullendore et al. 2010) or insect attack (Hao et al. 2008). Thus, an evolutionary trade-off was proposed for safety vs. efficiency as smaller pores may be able to seal faster at the cost of reducing sap flow (Savage et al. 2017).

A challenge to phloem transport arises from the fact that resistance scales linearly with phloem path length (Turgeon 2010, De Schepper et al. 2013, Savage et al. 2017). This has cast doubt on the feasibility of maintaining sugar transport over long distances in trees. However, Savage et al. (2017) showed that anatomical sieve tube traits scaled with height. From the tip of the tree towards the base, conduits grew wider, and sieve pores larger. Thus, lumen and plate resistance declined from source to sink, which eased pressure requirements needed for long distance flow. Besides these important anatomical scaling relationships, might there also be a physiological mechanism which influences pressure requirements? Sap transport in the sieve tube is thought to be driven by water uptake at the source, and by water loss at the sink, according to Münch's hypothesis (Münch 1930). The process therefore involves water inflow across the plasma membrane of source tissues, and water outflow along the plasma membrane of sink tissues (Eschrich, Evert & Young 1972). Münch assumed that the transport phloem is essentially impermeable to water (Münch 1930, p. 55-56). This view is also apparent in his physical model in which two osmotic cells (representing the source and sink, respectively) are connected via a pipe (representing transport phloem) that is not in contact with the water bath (Münch 1930, Fig 2 "Grundversuch"). In contrast to this view, water and solute exchange may extend throughout the entire length of the transport pathway, modifying the pressure gradient from source to sink (Thompson 2006b, De Schepper et al. 2013). Molecular evidence supports

this view, as sucrose transporters (Payyavula et al. 2011) as well as aquaporin water channels (Stanfield, Hacke & Laur 2017) have been identified in poplar transport phloem. Aquaporins may dynamically change the hydraulic conductivity of the plasma membrane (Chaumont & Tyerman 2014b), making their incorporation into phloem models worth investigating (Van Bel 2003, Sevanto 2018).

Previous phloem models have followed two themes for studying sap flow: a) the impacts of obstructions such as sieve plates on resistivity (flow resistance per length) or b) the impact of radial membrane transport. Structural models have assumed plates are perpendicular to side walls, sieve pores are circular and both sieve plates and lumen are free of obstruction (Thompson & Holbrook 2003a, Mullendore et al. 2010, Jensen, Mullendore, Holbrook, Bohr, Knoblauch & Bruus 2012a). Meanwhile, other models have presented the relative importance of radial water exchange on flow (Tyree & Dainty 1975, Cabrita, Thorpe & Huber 2013, Phillips & Dungan 1993, Hölttä, Mencuccini & Nikinmaa 2009, Jensen et al. 2009). Particularly important to these models is sieve tube pressure as a function of distance along the tube. Different rates of solute permeability were shown to impact this relationship (Cabrita, Thorpe & Huber 2013). However, differing values of plasma membrane hydraulic conductivity (L_p) and their impacts on changing pressure requirements have not been assessed (Tyree & Dainty 1975, Christy & Ferrier 1973).

In the current study, we model detailed structural characteristics of sieve plates and evaluate the qualitative impact of radial water permeability on flow. Specifically, our models use non-circular pores observed using high resolution SEM images of sieve plates from balsam poplar (*Populus balsamifera* L.). Further, we address how sieve tube resistance changes due to plate and lumen blockage events. Sieve plates are known to occur at various angles in relation to tube side walls, which may allow for increased plate pore area (Savage et al. 2017). Thus, we

modeled the impacts of angled plates on overall sieve tube resistance. We also present a simple permeable sieve tube model which incorporates scenarios using differing membrane hydraulic conductivity values. Many phloem models use a simplified solution to the Navier-Stokes equations, the Hagen-Poiseuille equation, to describe fluid movement through sieve tubes. The use of the Hagen-Poiseuille equation to model flow assumes sieve tube dimensions are cylindrical and tube walls impermeable (Phillips & Dungan 1993). Only in cases where the water potential of the phloem and xylem match would it be permissible not to incorporate the impacts of radial flows on axial transport (Sevanto 2014). Thus, previous models use the Hagen-Poiseuille equation with the addition of extra equations to account for radial water flows (Thompson and Holbrook 2003a). Here, we use the full Navier-Stokes equations which govern the motion of Newtonian fluids (Young et al. 2010). In addition, augmented equations are incoorperated describing radial flow in response to water potential differences across the sieve cell membrane. We are then able to obtain flow solutions through irregular sieve plate geometries and simultaneously account for radial water flows provided by the plasma membrane. These equations were solved computationally using Comsol Multiphysics modeling software which has been used previously for modeling flow through xylem pit membranes (Schulte 2012, Schulte, Hacke & Schoonmaker 2015). We discuss the implications of this model against previous efforts and present an updated interpretation of Münch's classical hypothesis on phloem transport.

2. Materials and Methods

a. Plant material

Balsam poplar (*Populus balsamifera* L.) plants were grown from cuttings following an existing protocol (DesRochers & Thomas 2003b) in similar conditions as a previous study (Stanfield, Hacke & Laur 2017). Briefly, cuttings from 10 cm stem segments of ≤2 years age were collected, soaked in water for two days, and then planted in an equal mixture of perlite, vermiculite, and Sunshine soil mix #4 (Sun Gro Horticulture, Agawam, Massachusetts). The source was Alberta-Pacific Forest Industries, from rootstock plants of 10 years age (Boyle, Alberta, Canada). Plants were rooted in a growth chamber for 50 - 93d; temperatures were controlled (18 - 21°C) over a 16/8 h photoperiod. After this time, plants were transferred to a greenhouse (18 - 30°C) for continued growth over 40 - 90d before sample collection.

b. Electron microscopy of sieve plates

For viewing sieve plates under the scanning electron microscope (SEM), the protocol of Mullendore et al. (2010) was followed. Stem or petiole sections were cut using pruners, and then trimmed to 1 cm segments with a fresh razor blade. Segments were immediately placed into a small metal basket and immersed in liquid nitrogen for one minute; the frozen sample was then placed into microcentrifuge tubes containing 100% ethanol and again frozen in liquid nitrogen for one minute. Samples were kept in the ethanol for 24h in a -20°C freezer. After, samples were thawed at room temperature and allowed to settle for 2 hours in deionized (DI) water. The 1 cm segments were then cut into transverse sections of approximately 1 – 2 mm thickness, rinsed in DI water, and put into a 0.1% proteinase K (Life Technologies, Carlsbad, California, USA) solution for up to three weeks. Samples were kept in solution at 55°C and continuously mixed using an orbital shaker set at 125 RPM; microcentrifuge tubes containing the samples were flipped daily to keep the Triton X in solution (see Mullendore et al. 2010). The solution was changed weekly with fresh proteinase K. After enzyme treatment, samples were freeze dried,

placed onto aluminum stubs and sputter coated with gold for SEM imaging using a Zeiss EVO MA 15. The microscope accelerating voltage was set to 20kV, and accelerating current set to 50 pA or 30 pA for cross or longitudinal sections, respectively.

c. Brightfield microscopy

Stem and petiole sections were fixed overnight in ice-chilled (< 4°C) Formaldehyde Acetic Acid (FAA), dehydrated in an ethanol series, and paraffin embedded. Longitudinal sections of 7µm thickness were made on a rotary microtome. Sections were placed directly onto glass slides flooded with water. Slides were allowed to dry overnight before staining. Staining was performed using a previously described method (Clark 1981). Briefly, sections were dewaxed in toluene, stained with 1% safranin 0 for one hour, and then 2% aniline blue for 5 minutes. After washing in Toluene, slides were mounted in DPX (Sigma-Aldrich, Saint Louis, Missouri, USA) and cover glass applied.

d. Immunolabeling callose

Sections were fixed and longitudinal sections made as noted above. Probe-on Plus slides (Fisher Scientific, Pittsburg, Pennsylvania, USA) were flooded with water and tissue sections placed on top. After setting overnight on a warm drying plate, the tissue sections adhered to the slides and were processed for antibody labeling following a previously described protocol (Gong et al. 2006). Briefly, slides were dewaxed in Histochoice (Sigma-Aldrich) solvent, and then rehydrated through an ethanol series. After several washings, slides were incubated in anti-callose primary antibodies (mouse monoclonal IgG antibody targeting (1 → 3)-β-oligosaccharides within (1 → 3)-β-glucans) overnight at 4°C. The next day, slides were washed thoroughly, and Alexa Fluor 488-conjugated [goat] anti-mouse secondary antibodies (Fisher Scientific) were applied and

samples were incubated at 37°C for two hours. Slides were washed again, Slowfade Gold with DAPI (Fisher Scientific) mounting medium added, and coverglass applied. Coverglass was sealed using nail polish.

For super resolution microscopy, antibody labeling was performed as above, with one modification; instead of mounting on glass slides, longitudinal stem sections were mounted onto cover glass (#1.5, 22 x 22mm). For better tissue adherence, coverglass was treated with 0.01% poly-l-lysine. Microscopy was performed using a Deltavision OMX V4 system (Applied Precision, Issaquah, Washington). The 488nm laser was used to excite the Alexa Fluor-488 antibody, power was set to 1%, and exposure times kept to 100-200 ms.

e. Computational modeling

The Navier-Stokes Equations are considered to be the fundamental equations governing the motion of incompressible, Newtonian fluids. Stated in compact form (Munson et al. 1990):

$$\rho\left(\frac{\partial \mathbf{V}}{\partial t} + \mathbf{V}\cdot\nabla\mathbf{V}\right) = -\nabla p + \rho\mathbf{g} + \mu\nabla^2\mathbf{V} \qquad \text{(Eqn 1)}$$

where ρ is the fluid density, $\mathbf{V}$ is the velocity vector, p is the fluid pressure, $\mathbf{g}$ is the gravitational acceleration vector, and μ is the fluid viscosity (see Table 4-1 for a list of mathematical symbols used in this paper). Note that terms are collected so as to reflect the origin of this equation with Newton's Second Law of Motion: terms on the left are acceleration terms and those on the right are forces (pressure, gravity, and shear forces, respectively).

Table 4-1. Mathematical symbols, their definitions and values used in model.

Symbol	Definition	Value
ϕ	Required angle change for pore correction of tilted plates obtained from SEM images	-
Q	Volume flow	-
r_{eq}	Equivalent circular area of a pore from its original non-circular shape	-
A_{pore}	Pore area	-
P_{pore}	Perimeter of pore	-
R^{sieve}	Resistance due to sieve plate	-
Δp^{sieve}	Pressure drop through sieve plate	-
F_{sieve}	The fractional resistance of the sieve cell due to the sieve plate	-
L^{cell}	The length of the cell between each sieve plate	100 µm
L_p	Hydraulic conductivity of the plasma membrane	5 *E*-14 m Pa^{-1} s^{-1}; 1 *E*-13 m Pa^{-1} s^{-1}
U	Flow velocity (open inlet models)	0.1 mm s^{-1}
Ψ_p	Pressure potential	-
Ψ_a	Apoplastic water potential	-1.7 MPa
Ψ_π	Sieve tube osmotic potential	-1.78 MPa
η	Fluid viscosity	1.7 *E*-3; 2.5 *E*-2 Pa s

Solutions for any particular case depend on a continuity or conservation of mass expression:

$$\frac{\partial \rho}{\partial t} + \nabla \cdot (\rho \mathbf{V}) = 0 \qquad \text{(Eqn 2)}$$

For the case of incompressible flow (density is constant), this continuity equation simplifies to:

$$\nabla \mathbf{V} = 0 \quad \text{or} \quad \frac{\partial u}{\partial x} + \frac{\partial v}{\partial y} + \frac{\partial w}{\partial z} = 0 \quad \text{(3D case)} \qquad \text{(Eqn 3)}$$

where u, v, and w are the velocity components in the x, y, and z directions, respectively.

For steady-state, incompressible flow, the momentum equation becomes:

$$\rho(\mathbf{V} \cdot \nabla \mathbf{V}) = -\nabla p + \rho \mathbf{g} + \mu \nabla^2 \mathbf{V} \qquad \text{(Eqn 4)}$$

Computational models for this study were developed to provide solutions for the flow equations for a geometry describing the sieve plates within sieve tubes.

SEM images of the plates in sieve tubes were used to develop models of the flow and pressure relations within those sieve tubes. The first step involved creating the geometry of the sieve plate using the SEM image imported into an AutoCAD drawing. The outlines of the sieve tube and of each pore in the sieve plate were traced using the polyline tool in AutoCAD, which is a connected series of straight lines or arcs. Two approaches were used in the drawing process depending on whether the sieve plate appeared to occur straight across the sieve tube or if it was tilted at an angle.

For sieve plates that appeared to lie straight across the sieve tube (the plane of the plate was perpendicular to the axis of the sieve tube), the image was imported into a 2D drawing and then scaled based on the scale bar shown in the image. Pores were traced as described above along with an outline of the sieve tube. The sieve tube outline was imported into the Comsol Multiphysics program (Comsol Multiphysics, Inc., Burlington, Massechusetts, USA; a general partial differential equation solver with geometry and mesh generation tools). The outline was then extended to a length that would allow for building in the sieve plate along with a region before and after the plate (typically about 60 μm in length). Thus the overall cell had the shape visible in the SEM image and not a simple cylinder. The pores of the sieve plate were imported onto a work plane mid-length along the model and extended a distance matching an average thickness of the sieve plates measured from images that cut across the plate (a standard value of 0.49 μm was used for all models).

For sieve plates that appeared to be tilted with respect to the axis of the cell, a more complicated procedure was required (Appendix 4-1a). The sieve pores in such plates did not appear circular, but elliptical in shape with their eccentricities oriented along the same axis. In contrast, most pores on plates perpendicular to side walls were closer to circular than elliptical and any eccentricity was oriented in random directions. Therefore we assumed the oriented eccentricity was an effect of the perspective distortion from the plate being tilted in reference to the plane of the section. To model these plates, we developed a procedure to correct the sieve pore shapes based upon an estimate of the angle of the sieve plate relative to the image plane. The estimation of this angle assumes that the pores are approximately isodiametric in shape. The plate tilt angle is estimate from:

$$\phi = 90 - \sin^{-1}\left(\frac{a}{b}\right) \quad \text{(Eqn 5)}$$

where ϕ is the angle change required in the correction process outlined below and a and b are the major and minor axes of the pore, respectively. The image also had to be rotated by the angle θ so that all the elongated pores are vertical.

The perspective correction process utilized a 3D drawing created in AutoCAD (Appendix 4-1b) The SEM image is imported onto the "Original" plane. The "Corrected" plane is drawn at an angle ϕ to the original plane containing the image. For drawing the corrected pores, the 3D drawing is rotated so that the Original plane is face-on as displayed. The sieve plate pores can then be traced as AutoCAD polylines, after ensuring that the Corrected plane is active so the pores will appear on the Corrected plane that is tilted with respect to the view. In this manner, a pore that appears elliptical in the image along the mean perspective tilt angle will be drawn as circular on the Corrected plane. When the drawing is then rotated so that the Corrected plane is face-on, the pores will have the corrected shapes. These pores were then selected, copied into a 2D drawing, and imported to Comsol Multiphysics as the sieve plate geometry of the model. This sieve plate was created in the model geometry at the angle ϕ (the angle between the plate normal and the axis of the sieve cell; Appendix 4-2).

Once the geometry was created within the model, fluid properties were set: the viscosity was 1.7 *E*-3 Pa s (Knoblauch et al. 2016) and the fluid density was 998 kg/m^3. The density would be higher due to sucrose in the sieve tube sap. However, note that the fluid density is not at all critical because for very low *Re* flow (typically in plant cells, less than 1), viscous forces strongly dominate over inertial forces where the density would be important. Boundary conditions were also established for the solution. For most models, all walls were set to a no-slip condition. The

inlet opening of the model was either set as a flow boundary with a fixed paraboloid velocity profile across the inlet (thus determining overall volume flow through the model) or as a pressure condition. The outlet opening of the model was set to a pressure condition of zero pascals.

The solution was based on a finite element method whereby the internal volume of the model is discretized into a set of either tetrahedral or hexahedral elements comprising the element mesh. Higher density meshes (smaller elements) tend to lead to more accurate solutions but place greater demands for computer memory and solution time. The general approach was to start with a coarser mesh and then gradually refine the mesh until the solution appears to be converging (see Appendix 4-3).

Solutions of the models gave fluid velocity and pressure at all points in the model geometry. Supplemental calculations can provide a number of derived quantities concerning the flow across the model. For example, one could obtain the integrated flow velocity across a face such as the model inlet or outlet or for individual pores in the sieve plate (thereby volume flow, m^3/s). Other derived values such as the average pressure across faces were also obtained. These pressures and flows were used to calculate a number of parameters describing the effects of sieve plates on fluid flow through sieve tubes.

Comparisons could be made between flow through individual sieve plate pores as modeled and as predicted from equations used in the literature (Thompson & Holbrook 2003a, Jensen, Mullendore, Holbrook, Bohr, Knoblauch & Bruus 2012b):

$$Q = \frac{\Delta p}{\left(\frac{8\eta L_{pore}}{\pi r_{eq}^{\ 4}} + \frac{3\eta}{r_{eq}^{\ 3}} \right)} \qquad \text{(Eqn 6)}$$

The above equation was developed for an isolated, circular point of entry. As the pores in our images often deviated from circular, we were interested in how pore shape would impact flow or resistance of the pores. For each pore in a sieve plate model, the radius of a pore with equivalent circular area (r_{eq}) was calculated from the area of that pore (A_{pore}):

$$r_{eq} = \sqrt{A_{pore}/\pi} \qquad \text{(Eqn 7)}$$

Next, a shape factor or index was calculated for each pore

$$Shape = \frac{P_{pore}}{A_{pore}} \Big/ \frac{2}{r_{eq}} \qquad \text{(Eqn 8)}$$

where P_{pore} is the perimeter of the actual pore. Note that this shape factor would be 1.0 for a round pore and will be greater than one for a pore that deviates from round.

Calculations were also made on resistances to flow and the fractional contribution of the sieve plate to overall sieve tube resistance. The resistance due to the sieve plate (R^{sieve}) is determined by the pressure drop through the sieve plate (Δp^{sieve}) and the volume flow (Q):

$$R^{sieve} = \frac{\Delta p^{sieve}}{Q}$$

where $$\Delta p^{sieve} = \Delta p^{model} - \Delta p^{empty} \qquad \text{(Eqn 9)}$$

The model and empty cell pressure drops are calculated from the difference between the average inlet pressure and the average outlet pressure. An empty cell refers to a model that is identical except no sieve plate is inserted.

The fractional resistance of the sieve plate (F^{sieve}) can be assessed by assuming some length for sieve cells in between each plate (L^{cell}).

$$R^{cell} = \frac{\Delta p^{empty}}{Q}\frac{L^{cell}}{L^{model}}$$
$$F^{sieve} = \frac{R^{sieve}}{R^{sieve} + R^{cell}} \qquad \text{(Eqn 10)}$$

A reasonable value for the length of typical sieve tube members was obtained from SEM images of longitudinal sections of the plant stems: a value of 100 μm was used in our calculations.

For models that were intended to consider sieve tubes having inflow or outflow through their lateral walls, the wall no-slip boundary condition was modified. The flow across the cell boundary can be set as a constant, but a more flexible option was to have flow determined by a water potential difference across the wall and the conductivity (L_p). So for this case, water flow across the side walls of the cells was determined from:

$$U_x = Lp\left(\psi_p + \psi_\pi - \psi_{outside}\right)\left(\frac{x}{\sqrt{x^2 + y^2}}\right)$$
$$U_y = Lp\left(\psi_p + \psi_\pi - \psi_{outside}\right)\left(\frac{y}{\sqrt{x^2 + y^2}}\right)$$
$$U_z = 0 \qquad \text{(Eqn 11)}$$

where U is the flow velocity (m/s). Flow is proportional to the wall conductance per unit area (L_p, conductivity, assumed to be dominated by the cell membrane). The default value was obtained from the literature as 5 E-14 m Pa^{-1} s^{-1} (Jensen et al. 2012, Thompson & Holbrook 2003b). The driving force is the water potential difference across the wall. The pressure component (ψ_p) is solved for by the model. The osmotic component (ψ_π) was set to -1.78 MPa reflecting sugar in the phloem sap, but other values could be chosen as well. The outside water potential was initially set to 0 MPa, but other values were also used in order to yield a flow in the

sieve tube which would be reasonable. The leaky walls condition requires one to specify velocity vector components in the *x, y,* and *z* directions, indicated by the subscript. The velocity component at the wall in *z* is still zero (a no-slip condition). The last factor on the right in each equation above gives the flow vector component such that the combined flow is always the same everywhere around the wall and in a direction normal to the wall (treated as cylindrical for this calculation).

We were also interested in observing the leaky wall effects over longer groups of cells. Models with 10 cells started to have a large number of mesh elements because each of the 10 sieve plates was fairly dense with elements. Such models were solved in a little more than 2 hours but required about 55 GB of computer memory. The idea of extending this approach to 100 or more cells seemed unworkable. So models were developed without sieve plates but with the fluid viscosity increased such that flow resistance along the model would approximate the resistance of models with plates. For example, if the sieve plate used in this case accounted for 93.2% of the total sieve cell resistance (F^{sieve}), a new viscosity ($\hat{\eta}$) was calculated as:

$$\hat{\eta} = \eta \frac{1}{1-0.932} \qquad \text{(Eqn 12)}$$

This would result in the same overall sieve tube resistance even though it is distributed along the cell and not located primarily at the ends of each cell. We verified this approach by comparing our simple two cell model with a plate, and again by removing the plate and increasing viscosity in accordance to eqn (12). We found that the two models differed by less than 0.1%, which validated the use of this approach.

3. Results

a. Sieve plates were a major source of overall sieve tube resistance

A variety of imaged sieve plates were modeled to determine their impact on sap flow. Overall, sieve plates accounted for the vast majority of sieve tube resistance. The median resistance of the sieve plates as a fraction of the total sieve tube resistance (F^{sieve}) was 85% (Table 4-2). Sieve plate resistance accounted for 77.9 - 95.3% of total sieve tube resistance. The median number of pores per plate was 90, while the median total pore area was 38.7μm^2. Increased pore area decreased plate resistance. For example, plate Stem_4 (Table 4-2) was in the upper quartile of total pore area, but in the lower quartile of predicted resistance. Another example (Stem_7), was in the lower quartile for total pore area, but in the upper quartile for total plate resistance. Thus, total pore area per plate impacted the modeled resistance of a sieve plate greatly. We investigated pore properties in more detail to determine more specifically which pore area traits most impacted flow.

b. Pores deviating from round increased sieve plate resistance

The observed sieve plate pores of balsam poplar varied from circular to oblong (Appendix 4-4). Illustrative to this point, we focused on one sieve plate and compared pores of various roundness (Fig. 4-1). To do this, we obtained the flow rate through each pore on the sieve plate as modeled from the actual pore shape provided by the SEM image (Fig. 4-1, white bars), then considered a perfectly circular pore of equivalent area using equation 6 and compared the ratio of these values (Fig. 4-1, gray bars). Overall, pores of a larger area (Fig. 4-1, pores A & B) had greater flow

rates in comparison to smaller pores (Fig. 4-1, pores C & D). In the first example (Fig. 4-1, pore A), this rather circular pore was predicted to have 101% of the flow rate of a perfectly circular pore of the same area. In contrast, very oblong pores (Fig. 4-1, pores C & D) had 81% and 72% of the predicted flow of a perfectly circular pore of the same area, respectively. Pores from many plates were modeled (Appendix 4-4) including ones which were perpendicular to side walls, as well as at an angle. Across all plates, pores which deviated from being round had reduced flow in comparison to perfectly round pores. In some cases, pores with oblong shapes reduced flow by greater than 50% in comparison to pores of a similar area that were round. Interestingly, when the ratio of the flow rate predicted by the model (numerical) and the flow rate predicted by the commonly used equation 6 (predicted) was plotted against pore area and shape factor, we found that the agreement between the two depended heavily on the shape factor. The pores that were very close to circular yielded numerical solution results very close to the predicted results, however as the pores deviated from circular, the predicted value deviated from the numerical solution (Fig. S4).

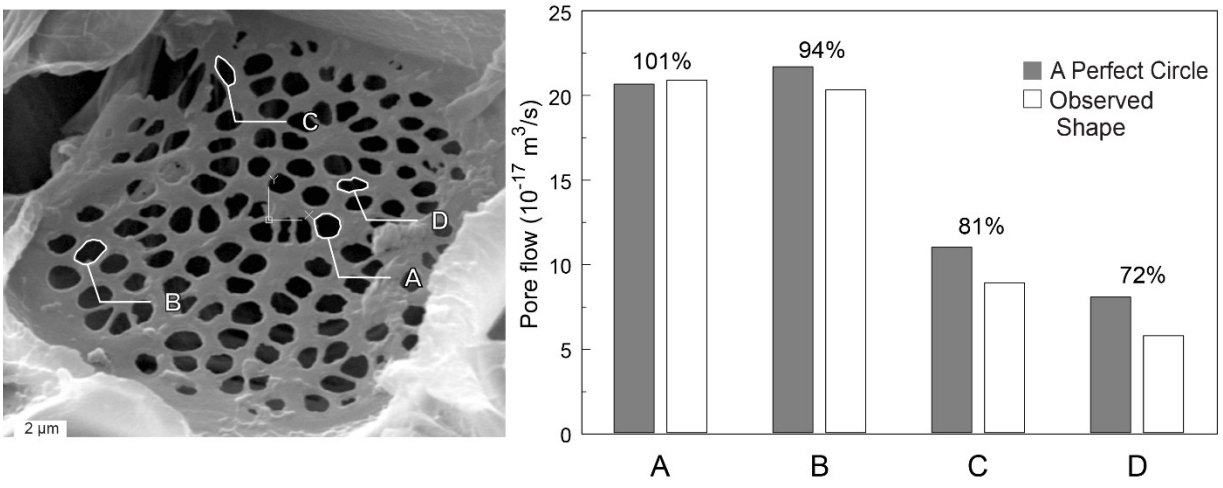

Figure 4-1. All sieve plate models were used to determine the impact of pore shape on pore flow. An example of four different pores (A-D) of various shapes and sizes were modeled on a plate. Overall, pores of a larger area (A, B) had greater flow rates than pores of a smaller area (C, D). Comparing the impact of pore shape on flow, pores were modeled in one of two ways: (1) as they appeared in the SEM image (white bars) and modeled with the Navier-Stokes approach based on eqns 3 and 4 or, (2) assuming that their observed area was made perfectly round (grey bars) and flow calculated based on eqn 6. Percentages above bars represent the differences in flow between pore area modeled as a perfect circle and pore area modeled as observed. Overall, pore flow decreased as pore shape deviated from round.

Table 4-2: General characteristics and modeling results of the sieve plates obtained through SEM images.

Plate ID	Plate tilt (angle)	Number of pores per plate	Total pore area per plate (μm^2)	Δp^{sieve} (Pa)	R^{sieve} (10^{15} Pa s m^{-3})	F^{sieve}
Stem_1	0	119	40.602	41.130	2.7242	0.932
Stem_2	0	74	32.616	30.442	2.8034	0.872
Stem_3	0	64	49.536	13.640	1.1300	0.792
Stem_4	0	101	62.016	14.480	1.0363	0.807
Stem_5	0	119	24.085	31.111	6.7575	0.816
Stem_6	0	101	43.125	24.237	2.1569	0.858
Stem_7	0	68	13.071	65.738	13.467	0.878
Stem_8	0	79	14.922	71.432	11.417	0.953
Stem_9	62.1	96	50.071	20.646	1.6727	0.841
Stem_10	66.3	93	36.808	22.315	2.8482	0.779
Petiole_1	0	54	14.253	55.495	10.057	0.871
Petiole_2	60.2	87	44.602	17.911	1.8261	0.794
Median	**0**	**90**	**38.7**	**27.3**	**2.76**	**0.85**

Models were constructed based upon two sieve elements and one sieve plate. Plate tilt is the observed angle in relation to sieve tube side walls obtained from the SEM image. Δp^{sieve} is the pressure drop through the sieve plate. R^{sieve} is the resistance of the sieve plate. F^{sieve} is the fraction of the total sieve cell resistance that is attributed to the sieve plate. Models were solved using eqn 3 and 4, calculations of sieve plate resistance and fraction of total resistance utilized eqns 9 and 10.

c. Pore arrangement had little impact on flow

In contrast to pore shape, the arrangement of pores had much less impact on flow. There was little impact of where the pore was located on the plate and its associated flow (Fig. 4-2). Additional models were then generated (Appendix 4-5) to determine if pores which clustered together conferred a greater flow than pores spaced far apart (i.e., pore cooperativity). Clustered pores of a typical shape increased flow by at most 2.4% (Table 4-3) over pores which were spaced far apart.

d. Modeling the impact of obstructions

Many potential obstructions occur both in the lumen and sieve plate of the sieve tube (Fig. 4-3). Unidentified spherical objects (Fig. 4-3a, *) were found in the lumen, and resting against sieve plates after sample preparation. In addition, callose accumulated both on side walls (Fig. 3b, blue lining), as well as on plates and within sieve pores (Fig. 4-3c). Note that the images in the first three panels of figure 3 are purely descriptive and were not used to generate data in the models. Under SEM view (Fig. 4-3d – f), some plates were observed with callose deposits around their pores. In addition, plates may be partially blocked due to P-protein or the endoplasmic reticulum (not shown). Thus, different blockage and obstruction scenarios in sieve tubes were modeled to determine their impacts on flow.

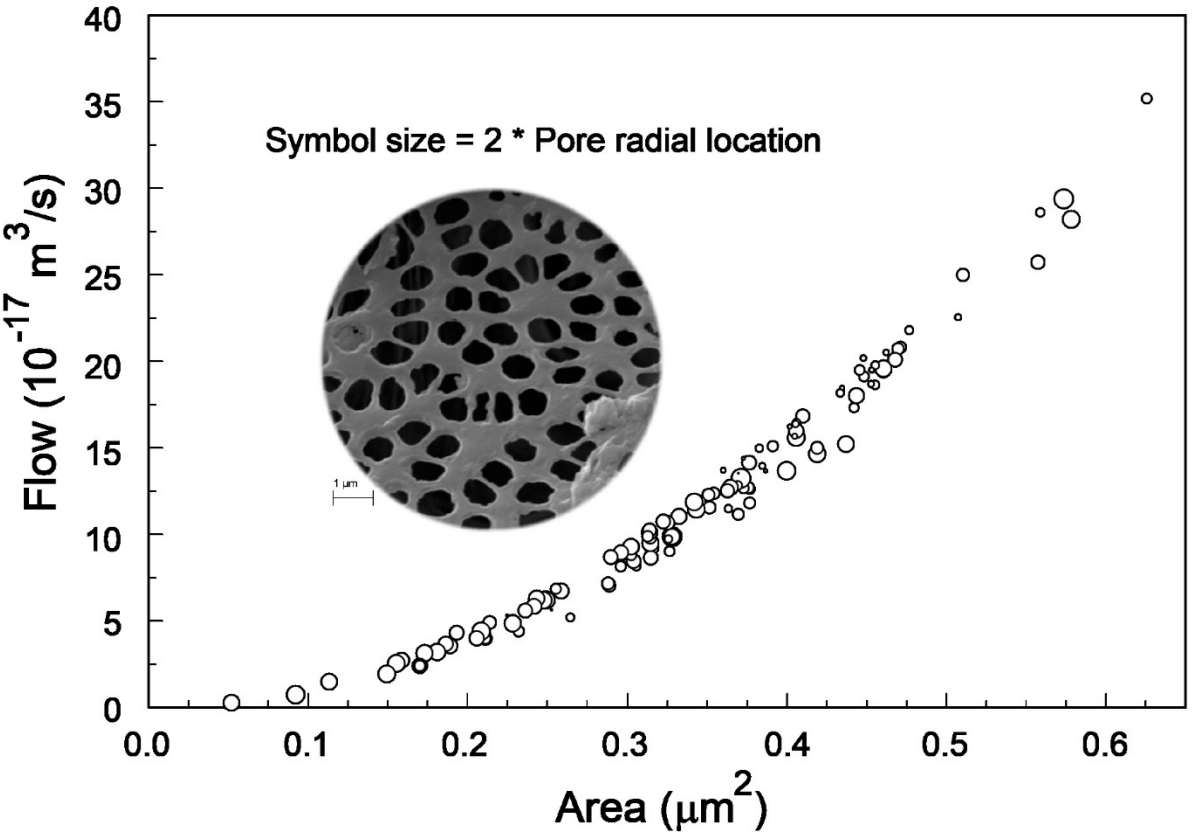

Figure 4-2: Modeling the impact of pore location on flow. Each circle represents the flow of a particular pore as a function of its area. Larger circles represent pores which are farther away from the center of the plate (symbol size = 2 * pore radial location). Although pore area impacts flow considerably, pore position had little relevance. The Stem 1 model was used for this example.

Table 4-3: Pore cooperativity models and their resulting impact of clustering and spacing.

Impact of Pore Arrangement on Flow		
Model	Volume flow ($1E$-14 m^3/s)	Change
Clustered	1.4099	
Spaced	1.3759	-2.4%
Clustered off-center	1.4095	-0.03

Pores from the first clustering model were based on typically shaped pores (Appendix 4-5). Models were run with a common pressure driving force, and so volume flow changes would indicate changes in total flow resistance. Models were solved using eqns 3 and 4.

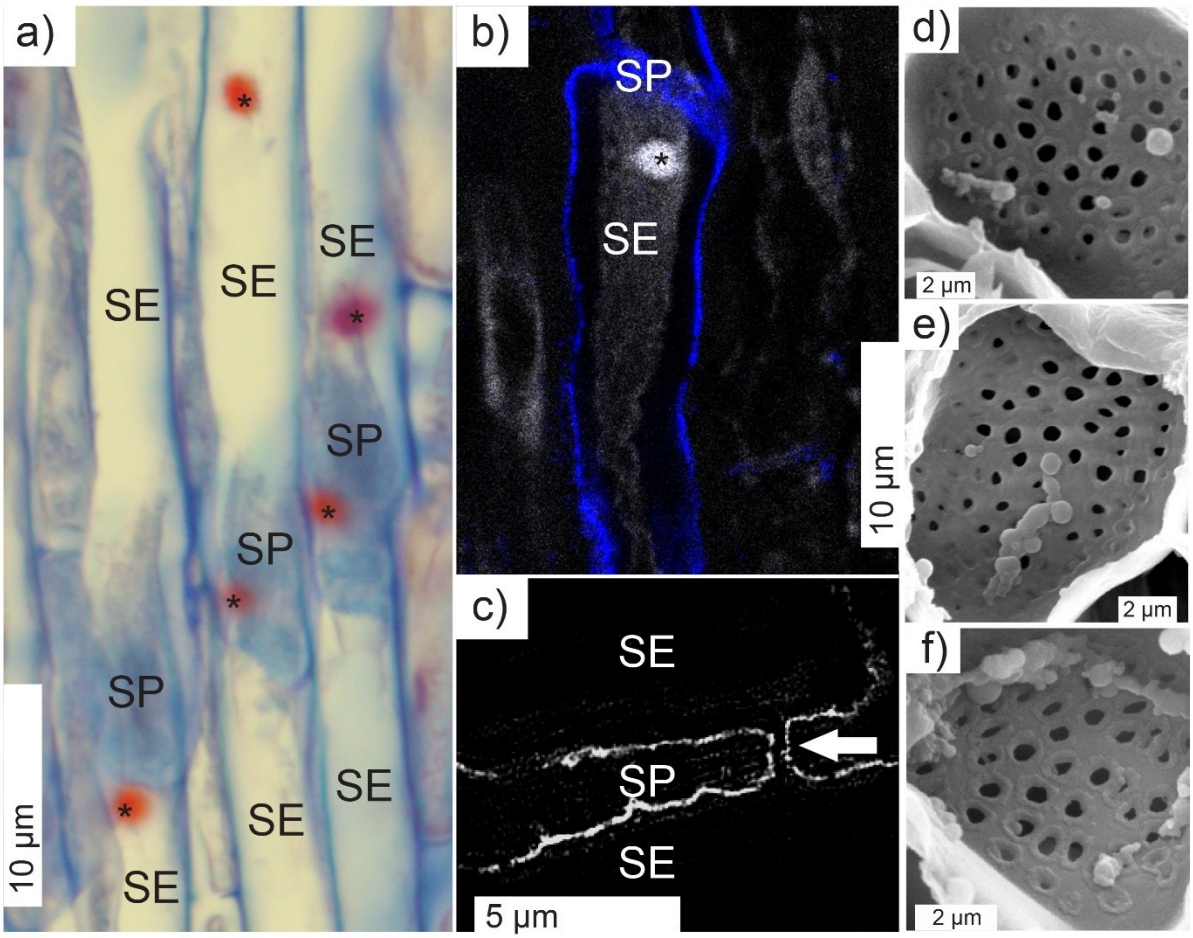

Figure 4-3: Images showing various obstructions within the sieve element lumen or sieve plate. (A) Longitudinal brightfield micrograph stained with aniline blue and safranin O showing sieve elements (SEs) within stem tissue. Unidentified objects (asterisk) occur within the lumen and against sieve plates and are visible as red spheres of ~2µm diameter. (B) Longitudinal confocal laser scanning micrograph from petiole tissue of a sieve element immunolabeled with callose antibody. Callose labeling (blue channel), is shown with background fluorescence (grey channel). Callose deposition is shown along sieve element walls as well as the sieve plate. (C) Longitudinal super resolution image of stem tissue immunolabeled with callose antibody. Two sieve elements are shown joined by their sieve plate. Callose was seen deposited along the sieve plate and within an individual sieve pore (arrow). (D – F) Three examples of sieve plates from petioles with callose observed occurring around pores. Symbols: SE = Sieve Element, SP = Sieve Plate, * = sieve element agglomeration.

Considering sieve plate pore obstruction, three examples of sieve plates (pictured in Fig. 3d – f) with callose deposition around their pores were modeled (Table 4-4). Resistances of these sieve plates (Table 4-4) were substantially greater than determined for sieve plates without callose deposits (Table 4-2) with a median sieve plate resistance of 4.76 *E*16 Pa s m^{-3} as compared to 4.82 *E*15 Pa s m^{-3}. The obstructed pore sieve plates therefore had a 9.9 fold increase in resistance to flow.

The impact of lumen obstructions was next modeled, simulating the occurrence of cytoplasmic spheres like plastids. In a three cell model (Appendix 4-6), 0-16 spheres of 2 μm diameter were introduced into the tube. Velocity heat map profiles (Fig. 4-4) show the color-coded speed of fluid movement and associated velocity vectors (arrows). While substantial increases in velocity were shown as fluid moved through sieve plate pores (Fig. 4-4a, red color), little change was observed near simulated lumen obstructions (Fig. 4-4a, *). By reducing the heat map scale (Fig. 4-4b), we were able to detect that velocity was greater near the center of the lumen in comparison to the margins. However, the impact of adding these 2μm diameter spheres increased overall resistance by at most 1.43% (Table 4-5).

Table 4-4: Modeling results for plates that appeared to have significant callose blockage.

Model	Pores	Pore area (μm^2)	Δp^{sieve} (Pa)	R^{sieve} (10^{15} Pa s m^{-3})
Petiole_Callose_1	38	6.8172	306.02	38.910
Petiole_Callose_2	58	7.0959	260.76	28.336
Petiole_Callose_3	42	3.6421	398.63	75.479

See Fig. 4-3 (d – f) for images of the three plates modeled.

Table 4-5: The contribution towards increased resistance in the lumen by adding spherical bodies.

Number of spheres (2 μm diameter) per two cells	% increase in pressure drop or resistance
0	0
4	0.46
8	0.91
12	1.07
16	1.43

The pressure drop change was calculated by comparison with a two cell model without obstructing bodies. Models were solved using eqns 3 and 4.

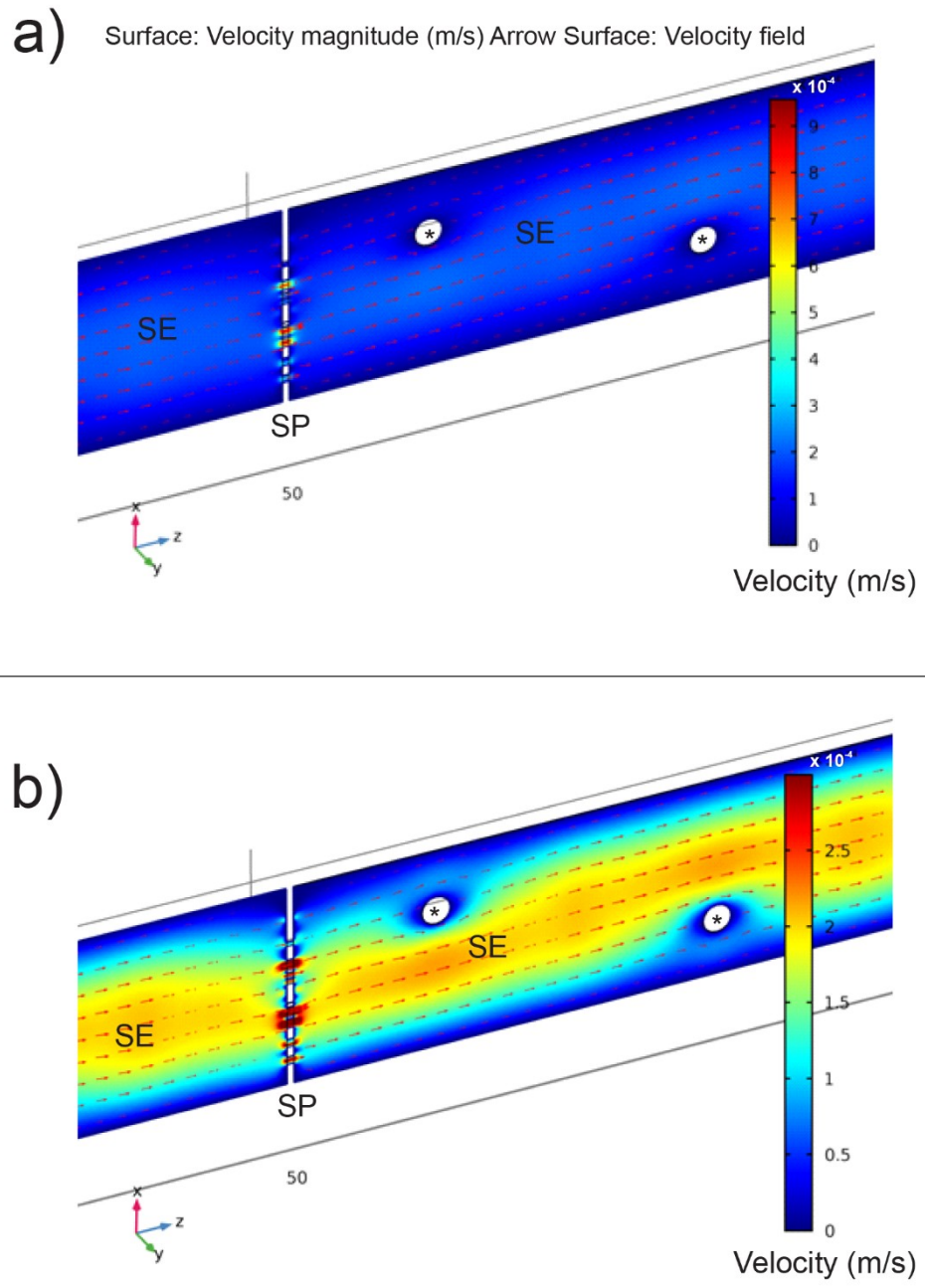

Figure 4-4: Velocity heat map of sieve tube model with sixteen spherical obstructions with two obstructions visible in this view (*). Colors indicate the speed of fluid movement, with arrows showing fluid direction. (A) A 0-1 mm/s color scale showed a majority of velocity increase at sieve plates. (B) A reduced 0-0.3 mm/s color scale which highlighted velocity changes due to lumen obstructions. Although the obstructions redirect flow, their overall effect was relatively minor (see Table 4-5).

e. Steeper plate angle could potentially decrease resistance by allowing for more pores

Sieve plates were observed to occur at differing angles in relation to sieve tube side walls (e.g., Appendix 4-4g). To assess the impact of sieve plate angle, a modeled sieve plate was tilted (Fig. 4-5). The reference angle for perpendicular plates was 0°. In a perpendicular orientation, this plate accounted for 93.2% of modeled sieve tube resistance (Table 4-6). Surprisingly, tilting this plate by 60° did not reduce its absolute resistance in comparison to the perpendicular plate (Fig. 4-5a, b). However, tilting the plate made it possible for the total plate surface area available for pores to increase. To simulate a possible increase in total pore area, pores were added which increased the total pore area to 81.88μm^2 from 40.60μm^2. As outlined above (Table 4-2), adding pore area decreased resistance. Thus, the pressure drop across the sieve plate with added pores declined by greater than 50% in comparison to the first two scenarios (Fig. 4-5c).

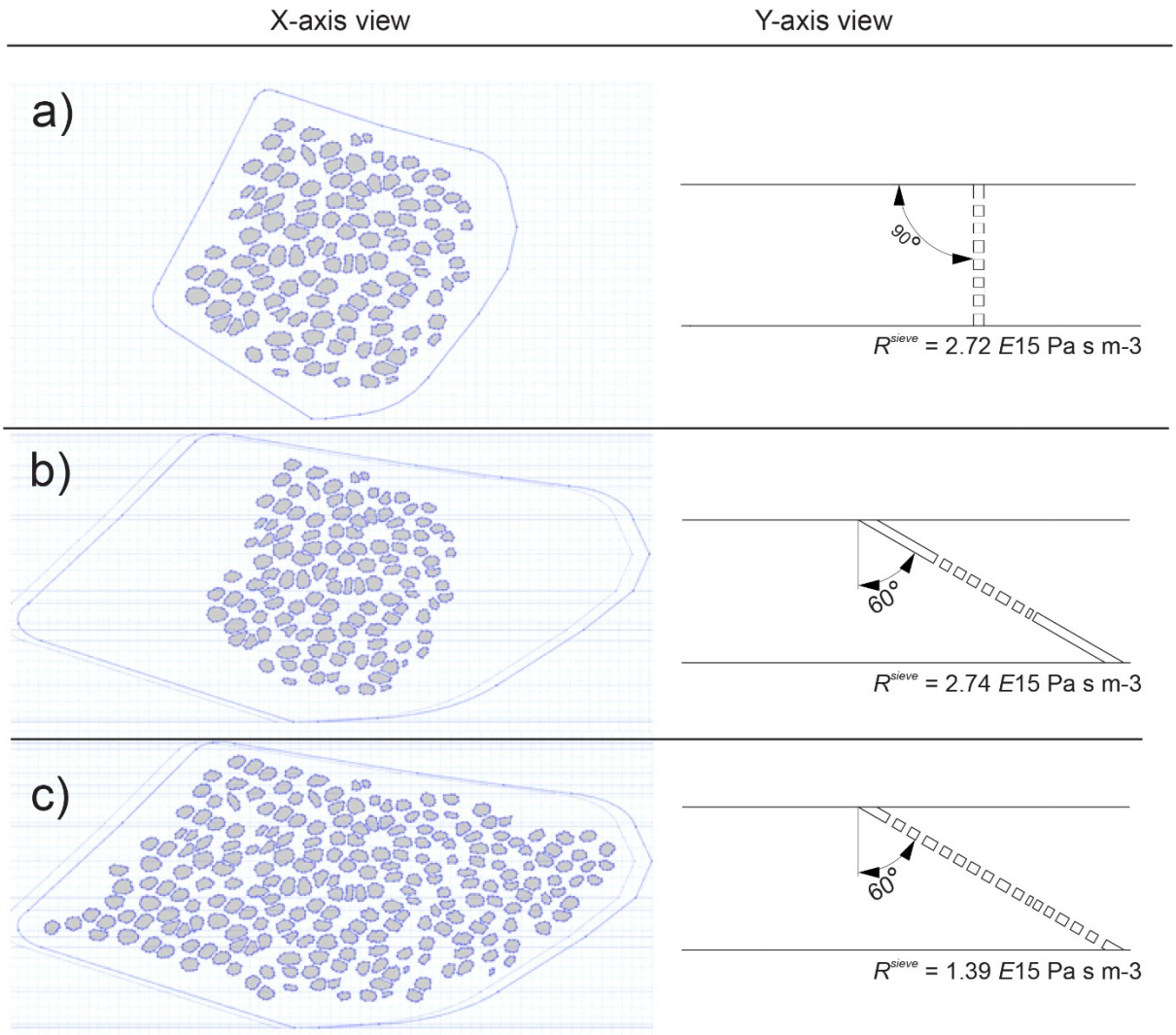

Figure 4-5: Models for considering the effect of sieve plate angle within the sieve cell. (A) An example of a plate with 90° angle in relation to sieve tube side walls. (B) The same plate from (a) was titled by 60°. Upon tilting the plate, the plate area becomes enlarged, yet the pore area remains unchanged (pores in part b are the same size as those in part a). The resulting sieve plate resistance was essentially unchanged (R^{sieve}). (C) The same plate and angle from (b) was modeled, except that an additional 116 pores are added to the unfilled plate area. This additional pore area reduced the sieve tube resistance by greater than 50% in comparison to examples (a) and (b).

Table 4-6: Resistance changes due to the angling of plates.

Plate angle (°)	Δp^{sieve} (Pa)	R^{sieve} (10^{15} Pa s m^{-3})	F^{sieve}
0	41.130	2.7242	0.932
20	41.186	2.7279	0.932
40	41.316	2.7365	0.932
60	41.835	2.7709	0.933
60 filled	20.975	1.3893	0.874

An angle of 0° signifies a plate which is perpendicular to sieve tube side walls. The quantity Δp^{sieve} (Pa) is the pressure drop due to the sieve plate. R^{sieve} is the resistance of a sieve plate. F^{sieve} is the fraction of total sieve cell resistance that is attributed to the sieve plate. Models were solved using eqns 3 and 4.

f. Permeable Membranes Significantly Reduced Pressure Requirements

The high sieve plate resistance observed in our models presents a quandary to phloem transport. How is sugar movement supported past high resistance sieve plate bottlenecks? This is especially important in trees where transport occurs over long distances. Our models of sieve cells with plates suggest that a median value (from data in Table 4-2) of 40.1 Pa pressure drop along a 100 μm sieve cell would lead to a 0.401 MPa/m pressure gradient along the phloem, a high value that would seem to be a problem for phloem transport within tall trees. Although it is increasingly appreciated that the plasma membranes of sieve elements are permeable, the role of aquaporins in regulating radial water movement and its impact on axial transport has not been assessed in a model. Thus our model incorporates permeable cell membranes with hydraulic conductivity values that can be adjusted. We then asked: do strong radial flows help to overcome the large pressure gradients caused by high resistance sieve plates? Two general models were created: (1) water was allowed to enter/exit through the sides of a sieve tube via permeable membranes (along the full length of the tube) and (2) a control scenario recreating a sealed pipe. Both scenarios were set up along a 10cm length of sieve tube (Fig. 4-6a). In these models, sieve plates were omitted due to high computational demands (1000 plates would be required). Instead, the viscosity of the fluid was increased to approximate the overall resistance of sieve plates recurring every 100μm (see methods for governing equations). A comparison of one of our sieve plate models with the sieve plate present and one without a sieve plate, but the viscosity increased,

showed a matching pressure drop in the models (less than 0.1% difference). Scenarios i & ii or iii & iv (Fig. 4-6) are directly comparable to one another, as each set has matching maximum volume flows (as illustrated by the size of the horizontal arrows in Fig. 4-6a).

In the first scenario (Fig. 4-6a, i), the inlet end of the tube was closed. Therefore, flow was generated due to an influx of water traveling through the sides (simulating the cell membrane in a source). The rate of water flow through the sides of sieve tubes was driven by a water potential gradient (Ψ_π = -1.78MPa inside the tube and Ψ_a = -1.7 MPa outside the tube), and by setting membrane permeability to a standard value for membrane permeability from previous phloem modeling studies (see methods). As the water entered into the sieve tube (Fig 4-6a, grey arrows), the magnitude of volume flow increased from left to right (Fig 4-6a, black arrows). Halfway through the tube, the water potential switched to allow radial flow back outside, simulating a sink region. The resulting maximum flow in the middle of the sieve tube was 1.469 *E*-14m^3 s^{-1}. In comparison, the next model had impermeable sides (Fig. 4-6a, ii) and an inlet to drive flow. The inlet condition in this model was set to match the flow rate observed in the middle of the first permeable wall model (Fig. 4-6a, * indicates equal flow rates). In the next scenario (Fig. 4-7a, iii), the membrane permeability of the sieve tube sides was doubled while keeping the water potential gradient across the membrane unchanged. This doubling of membrane permeability increased the maximum flow by about 1.9-fold. This flow of 2.811 *E*-13 m^3s^{-1} was applied as the inlet condition of the final sealed pipe model (Fig. 4-6a, iv#).

From these modeled setups, four pressure profiles as a function of position along the sieve tube were generated (Fig. 4-6b). The overall pressure profiles for the permeable membrane models were non-linear (Fig. 4-6b, lines i, iii). In comparison, the sealed pipe models generated linear pressure drops (Fig. 4-6b, lines ii, iv). Models with standard (Fig. 4-6b, solid lines) or increased volume flow (Fig. 4-6b, dashed lines) were compared. The first permeable sieve tube model (Fig.4- 6b, line i) experienced a pressure drop of 0.0192 MPa. In comparison, the sealed pipe model experiencing the same maximum magnitude of flow (Fig. 4-6b, line ii) lost 0.0388 MPa; this represents a 2 fold increase in pressure loss over the same distance. By doubling the L_p (Fig. 4-6b, line iii), the permeable sieve tube experienced a 0.0362 MPa pressure drop over its 10cm length. This increased pressure drop was due to the greater flow magnitude as a result of the higher membrane permeability. Comparing this to the sealed pipe scenario that used the same maximum flow (Fig. 4-6b, line iv), a pressure drop of 0.0743 MPa was observed. This represents a 2.1 fold increase in pressure loss for the same distance traveled. To sum, water flow through permeable plasma membranes along the entire length of the sieve tubes allowed for the same velocity and volume flow, while the pressure loss was cut in half.

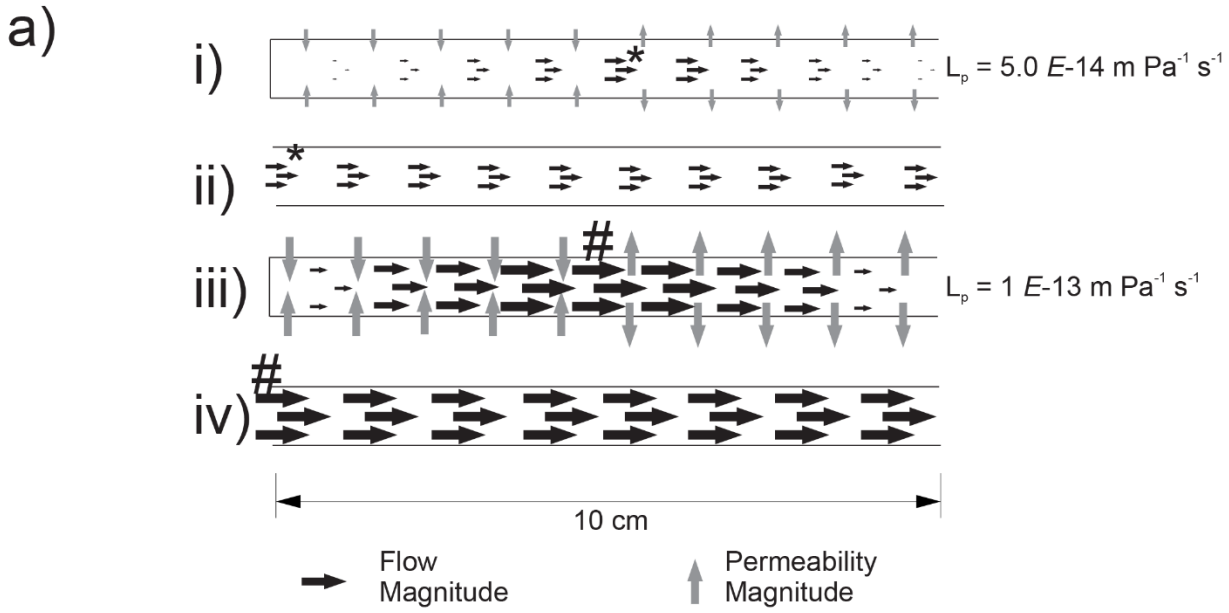
a)
i)
ii)
iii)
iv)
*
#
L_p = 5.0 *E*-14 m Pa^{-1} s^{-1}
L_p = 1 *E*-13 m Pa^{-1} s^{-1}
10 cm
Flow Magnitude
Permeability Magnitude

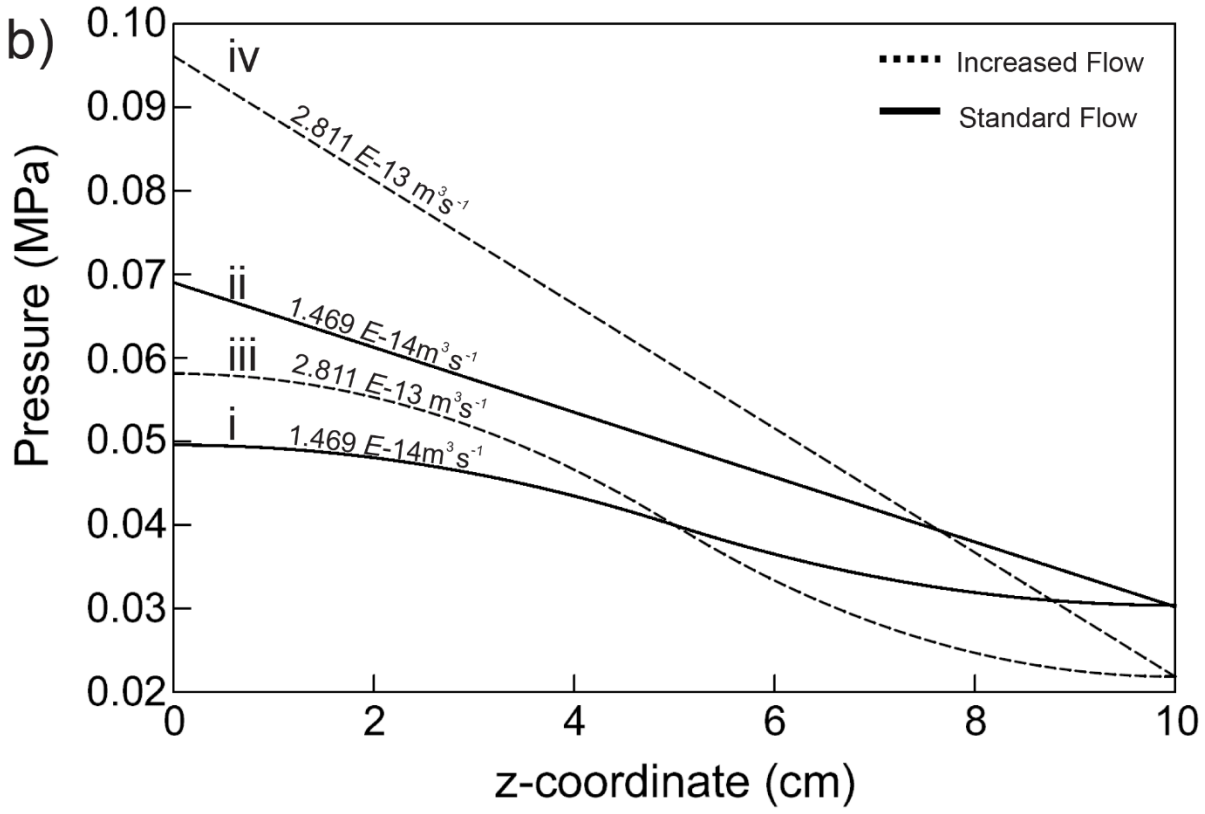
b)
Pressure (MPa)
z-coordinate (cm)
Increased Flow
Standard Flow
iv
ii
iii
i
2.811 E-13 $m^3 s^{-1}$
1.469 E-14$m^3 s^{-1}$
2.811 E-13 $m^3 s^{-1}$
1.469 E-14$m^3 s^{-1}$
0.10
0.09
0.08
0.07
0.06
0.05
0.04
0.03
0.02
0
2
4
6
8
10

Figure 4-6. A model was constructed to determine the impact of water transport across membranes on pressure loss through a section of sieve tube. (A) Conceptual model of 4 scenarios which were tested. Each scenario represents a 10-cm sieve tube segment. Viscosity was increased to compensate for the removal of sieve plates. In the first scenario (i), permeable membranes (grey arrows) increase volume flow (black arrows) for the first 5cm along the tube, and then decrease flow for the second half of the 5cm segment. This water movement into the sieve tube was driven by a water potential gradient specified in the model (into the sieve tube for the left half and out of the sieve tube for the right half). In contrast, the sealed sieve tube scenario (ii), had an open inlet and used the same starting volume flow as the maximum volume flow of the previous model (*). The next two scenarios (iii & iv) replicated the conditions of the first two, except membrane conductivity (L_p) was doubled, resulting in a higher maximum volume flow (#). (B) The four pressure profiles generated from the scenarios of (a). Maximum volume flow rates are labeled above each line. Standard flow models (solid lines) are distinguished from increased flow models (dashed lines). Non-linear lines (i & iii) are due to increases/decreases to the maintenance of pressure over long distances from water inflow/outflow provided by permeable membranes. Straight lines (ii & iv) represent sealed tube pressure profiles. Comparing within sieve tubes which had either increased flow or standard flow, pressure loss was reduced by up to 2-fold for permeable sieve tubes over sealed sieve tubes.

4. Discussion

a. Sieve plates add Substantial Resistance to the Sieve Tube Pathway

Our model provides evidence to support the hypothesis that sieve plates are responsible for a major source of resistance in sieve tubes of young balsam poplar stems. In a recent study assessing sieve tube resistances across multiple families, Liesche et al. (2017b) compared sieve plate and lumen flow properties in 447 angiosperm and gymnosperm species. In terms of absolute pressure drop across the sieve plate, our results lie on the upper end of values for sieve plates in angiosperms (Liesche et al. 2017b). Therefore for poplar stems our results suggest that sieve plates contribute substantially to sieve tube resistance in comparison to other species. One explanation is that our calculations used a sieve element length of 100μm, which was representative of the images collected during our analysis. This length is on the low end of the spectrum in comparison to other species. To study the effect of sieve element length on pressure gradients, we also developed a model for one sieve plate located in a 200μm cell. By doubling the sieve element length, we found that the sieve plate contribution towards overall sieve tube resistance declined by 6.6% (results not shown). The effect of having longer sieve elements over a longer distance would be a decrease in pressure gradient as the number of sieve plates per unit length would decline. This has been suggested as an evolutionary adaptation to decrease pressure requirements in the sieve tubes of tall trees (Savage et al. 2017). Thus, the impact of lowering sieve element length is to increase the fractional contribution of the sieve plates towards overall resistance, and lower the contribution due to the lumen. In the model with the sieve plate in the 200 μm cell, the pressure drop between the ends of the cell increased from 44.1 Pa to 47.2 Pa, a 7% increase. But because the cell length was doubled, the pressure gradient along a series of such cells would decrease from 0.44 MPa/m to 0.24 MPa/m. Therefore, cell length is clearly an

important factor in overall phloem transport. Further, sieve tubes do not have lumens which are perfectly cylindrical, and instead may be "bone shaped" in appearance with wider diameters towards the sieve plate (although this may be an artifact of sample preparation). In future modeling work, it would be of interest to determine the impact of these irregular lumen shapes. However, the focus of the current work was to assess which sieve plate characters most impact flow.

We found that the most important sieve plate traits which impact plate resistance were total pore area and shape. Previous methodologies take into account the variability of pore radii in their models (Liesche et al. 2017b, Savage et al. 2017) but assume pores are always circular. However, our results indicate that assuming pore shape as being circular instead of using their actual shape may underestimate pore flow by as much as two-fold in comparison to past work (e.g., Thompson and Holbrook 2003a, Jensen et al. 2012b). To our knowledge, Jensen et al. (2012a) was the only other study to have used the Comsol software to provide solutions for the Navier-Stokes equation for fluid flow through sieve plates. This study modeled one example of a sieve plate from *Cucurbita maxima*, a species with relatively large sieve plate pores. The numerical results shown in Jensen et al. (2012b) varied by only 10% compared with analytical solutions for fluid flow through sieve tubes using the Hagen-Poiseuille equation (Mullendore et al. 2010, Thompson & Holbrook 2003a). The accounted variability was attributed to interactions between pores. In the current study, we similarly provide numerical solutions for >13 imaged sieve plates. We found that interactions between pores due to pore clustering accounted for only a minor increase in overall flow. In addition, we found that while pores that are close to circular show agreement between previous analytical approaches and the numerical solutions to the full Navier-Stokes equations, pores that deviate from circular do not show the same agreement. Thus

we suggest that flow through non-circular sieve pores cannot be approximated by assuming circular pores of equivalent area.

Another interesting sieve plate trait that has received relatively little attention is plate angle. Using the same sieve plate while changing its angle does little to impact resistance. However, a steeper plate angle provides greater area for pores to develop. Thus if plants respond developmentally to increased plate area by producing more pores, the sieve element resistance would drop markedly. In future research, it would be useful to consider more fully the number of pores and total pore area occurring on plates of varying angles. Across a number of tree species, the number of sieve areas within a plate increase with steeper plate angle (Savage et al. 2017). Thus, sieve tubes may additionally reduce resistance over length by generating steeper angle sieve plates that may possess greater total pore area.

b. Impacts from lumen and plate obstructions

In another set of models, we determined the impact of both lumen and plate obstructions on flow. Although we followed the technique of Mullendore et al. (2010) to image sieve plates with minimal wound artifacts, some sieve plates still showed the appearance of callose rings. Many factors may cause this, including physical disturbance (Jaeger et al. 1988b). In the event that plates were partially blocked with callose, we used this as an opportunity to assess how this obstruction would impact flow. Plates with partially blocked pores had substantially increased resistance values in comparison to unblocked pores. By preparing samples with proper freezing technique prior to viewing, SEM (Mullendore et al. 2010) and TEM (Froelich et al. 2011) images have shown sieve plates without any callose deposition. These findings provide evidence that sieve pores were mostly open to flow *in situ*. Despite this, intact sieve tubes may still respond to environmental stimuli. After heat shock, sieve plates of broad bean were blocked with callose 3-

4 cm from where the stimulus was applied (Furch et al. 2007) and accumulation was shown to increase as a response to temperature in cotton (McNairn 1972). In addition, rice plants under siege by the brown planthopper plugged sieve plates with callose proximal to areas where the insect's stylet was inserted (Hao et al. 2008). This opens the possibility that pore closure is regulated by more than one macromolecule. Future work in this area would be of interest to assess the extent of pore blockage after gentle preparation techniques under various abiotic and biotic stresses.

As opposed to sieve plates, blockages in the lumen played a less significant role for reducing flow. These spheres may represent protein agglomerations, plastids, mitochondria, endoplasmic reticulum, or other organelles found in sieve tubes (Knoblauch et al. 2014). Froelich et al. (2011) showed that up to 35% of the lumen is obstructed due to these cytoplasmic contents in well preserved sieve tubes. However, the occurrence of P-protein agglomerations were reported infrequently, making their contribution towards total sieve tube resistance an order of magnitude less than the sieve plate or lumen. Similarly in this study, our light microscopy images reveal few protein agglomerations per sieve element. Thus blockages at the sieve plate incur a much steeper penalty to flow than blockages of the lumen according to our results.

c. Permeable membranes modify pressure requirements

Our conceptual understanding of phloem transport is mostly based on the pressure flow hypothesis (illustrated in Münch 1930, Fig 2 "Grundversuch"). In Münch's insightful figure, there are two compartments with semipermeable membranes (the source and sink, respectively). The sides of the connecting pipe are considered to be impermeable to water. Münch thought that this was necessary to prevent pressure loss along the pathway (Münch 1930, p. 56). This assumption is consistent with the frequent use of the Hagen-Poiseuille equation in models of

phloem transport (e.g., Thompson & Holbrook 2003a, Savage et al. 2017, Epron et al. 2018). Use of Poiseuille-driven flow has been justified as long as extra equations are included to account for radial water exchange (Thompson & Holbrook 2003a). Thus, the use of Hagen-Poiseuille is justified in scenarios where radial transport is insufficient to alter axial flow (see Thompson and Holbrook (2003a) and Sevanto (2014) for an in depth discussion on the use of the Hagen-Poiseuille equation and radial transport). However, our model provides simulations to assess how axial transport is impacted when radial flow is relatively high. Assessing this scenario is important in light of recent molecular evidence. In poplar, there is evidence for sugar transporters (Payyavula et al. 2011) and aquaporin water channels (Stanfield, Hacke & Laur 2017) which occur along the entire transport pathway. Water and sugars may therefore be exchanged along the entire route, not just in the source and sink regions (Thompson 2006, DeSchepper 2013, Sevanto 2018). This may have implications for the regulation of phloem pressure (Sevanto 2014, Van Bel 2003), and it may also impact pressure and velocity profiles (Tyree & Dainty 1975, Phillips & Dungan 1993, Cabrita, Thorpe & Huber 2013). Here we asked how a semipermeable membrane with high water transport capacity would affect the pressure gradient in the sieve tube. Although simple, this scenario provides an important modification to the original Münch model (Fig. 4-7) and is designed to provoke future studies on the impacts of radial flows on axial transport.

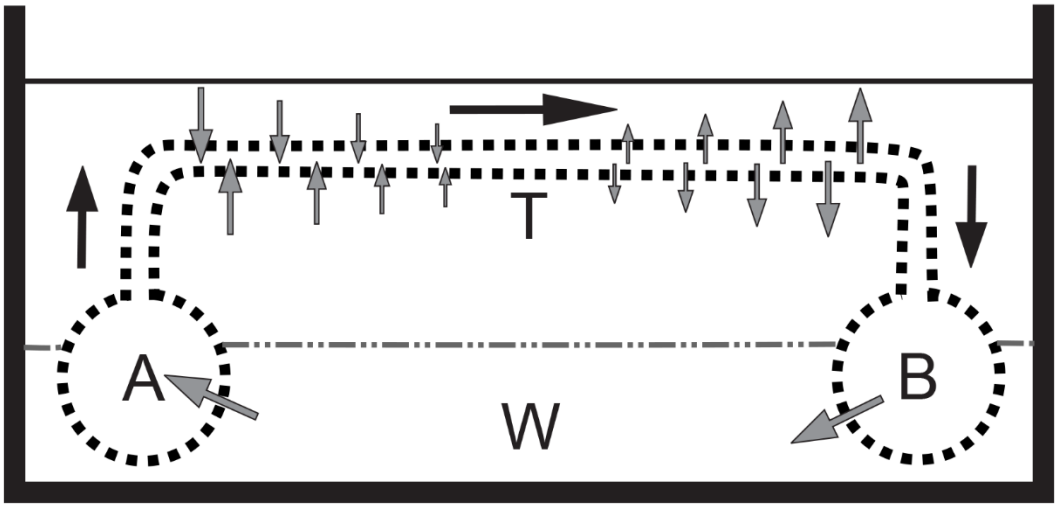

Figure 4-7: The original Münch model of osmotically driven pressure flow, with the modification of permeable walls throughout the transport pathway. Two permeable containers representing a source (A) and sink (B) are connected by a permeable transport pathway (T). The entire setup is submerged below water level (black line) within a water bath (W). This is in contrast to the original model whose water level (dashed line) only covered the source and sink vessels. Water movement past membranes is symbolized by grey arrows, solution flow by black arrows.

Incorporating radial water flows allows for a consideration of their impacts on axial flows and pressure gradients. We found that permeable membranes allow for non-linear pressure profiles and a significant reduction in pressure gradients compared with flow in a sealed system. In addition, we found that increasing the membrane hydraulic conductivity values increases pressure profiles because higher inflow led to greater flow through the sieve tube. Previous studies have also shown non-linear pressure profiles due to radial inflow (Philips and Dungan 1993, Cabrita, Thorpe & Huber 2013) and also report pressure gradient increases due to increased radial water flows. In contrast to the current study, the aforementioned reports seem to show that when radial water flow ceases, pressure gradients are reduced. However, an explanation for this may be due to the starting boundary conditions as our model used a closed vs. an open inlet. Thus, there was no inflow from the inlet and flow was only generated by radial inflow. The pressure drop along a length of phloem sieve cells is determined by the volume flow rate and the distance traveled. An increase in flow rate would occur in a model with radial inflow in addition to inlet inflow. For our models with higher radial inflow because of a higher radial conductivity, flow was increased along with the pressure drop. Therefore the results of these two studies are actually consistent. Radial inflow would allow for greater flow in the phloem and/or a reduction in pressure requirements because the distance involved in that flow is reduced. In addition, we use different values for membrane hydraulic conductivity, which also controls pressure generation. This highlights the importance of both boundary conditions and membrane hydraulic conductivity in determining pressure profiles, the latter of which may be controllable by the plant.

Being able to exchange water and solutes along the entire sieve tube pathway would provide the plant with more control over pressure and flow in the sieve tubes. For instance, it

may be favorable to minimize sieve tube membrane permeability when xylem pressure is rapidly becoming more negative; this would reduce water loss to the xylem (Sevanto 2014) and buffer the sieve tubes to some extent from the dynamic changes in xylem pressure. On the other hand, when the water tension in the xylem is mild (e.g., at night), increased aquaporin activity along an extended uptake zone may allow for increased transport rates in the phloem. Future work in this area may address the optimal membrane hydraulic conductivity values which promote the most efficient flow in a variety of environmental conditions. While the impact of changes in membrane permeability on pressure gradients in the phloem can be demonstrated, much remains to be learned about the sensors and signaling feedbacks that would be required to modify phloem flow in response to changes in water potentials. We hypothesize that aquaporin regulation plays a central role in this scenario.

5. References

Ahamed A., Murai-Hatano M., Ishikawa-Sakurai J., Hayashi H., Kawamura Y. & Uemura M. (2012) Cold stress-induced acclimation in rice is mediated by root-specific aquaporins. *Plant and Cell Physiology 53*, 1445-1456.

Alonso A., Queiroz C.S. & Magalhães A.C. (1997) Chilling stress leads to increased cell membrane rigidity in roots of coffee (coffea arabica L.) seedlings. *Biochimica Et Biophysica Acta (BBA)-Biomembranes 1323*, 75-84.

Aroca R., Amodeo G., Fernández-Illescas S., Herman E.M., Chaumont F. & Chrispeels M.J. (2005) The role of aquaporins and membrane damage in chilling and hydrogen peroxide induced changes in the hydraulic conductance of maize roots. *Plant Physiology 137*, 341-353.

Bilska-Kos A., Szczepanik J. & Sowiński P. (2016) Cold induced changes in the water balance affect immunocytolocalization pattern of one of the aquaporins in the vascular system in the leaves of maize (zea mays L.). *Journal of Plant Physiology 205*, 75-79.

Cabrita P., Thorpe M. & Huber G. (2013) Hydrodynamics of steady state phloem transport with radial leakage of solute. *Frontiers in Plant Science 4*, 531.

Chaumont F. & Tyerman S.D. (2014a) Aquaporins: Highly regulated channels controlling plant water relations. *Plant Physiology 164,* 1600-1618.

Chevalier A.S. & Chaumont F. (2015) Trafficking of plant plasma membrane aquaporins: Multiple regulation levels and complex sorting signals. *Plant & Cell Physiology 56*, 819-829.

Chisholm S.T., Parra M.A., Anderberg R.J. & Carrington J.C. (2001) Arabidopsis RTM1 and RTM2 genes function in phloem to restrict long-distance movement of tobacco etch virus. *Plant Physiology 127*, 1667-1675.

Christy A.L. & Ferrier J.M. (1973) A mathematical treatment of munch's pressure-flow hypothesis of phloem translocation. *Plant Physiology 52*, 531-538.

Clark G. (1981) Staining procedures. In *Staining Procedures* Staining procedures. William & Wilkins.

Comtet J., Jensen K.H., Turgeon R., Stroock A.D. & Hosoi A.E. (2017) Passive phloem loading and long-distance transport in a synthetic tree-on-a-chip. *Nature plants 3*, 17032.

Comtet J., Turgeon R. & Stroock A.D. (2017) Phloem loading through plasmodesmata: A biophysical analysis. *Plant Physiology 175*, 904.

De Schepper V., De Swaef T., Bauweraerts I. & Steppe K. (2013) Phloem transport: A review of mechanisms and controls. *Journal of Experimental Botany 64*, 4839-4850.

DesRochers A. & Thomas B. (2003a) A comparison of pre-planting treatments on hardwood cuttings of four hybrid poplar clones. *New Forests 26*, 17-32.

DesRochers A. & Thomas B. (2003b) A comparison of pre-planting treatments on hardwood cuttings of four hybrid poplar clones. *New Forests 26*, 17-32.

Esau K. & Thorsch J. (1985) Sieve plate pores and plasmodesmata, the communication channels of the symplast: Ultrastructural aspects and developmental relations. *American Journal of Botany 72,* 1641-1653.

Eschrich W., Evert R.F. & Young J.H. (1972) Solution flow in tubular semipermeable membranes. *Planta 107*, 279-300.

Fetter K., Van Wilder V., Moshelion M. & Chaumont F. (2004) Interactions between plasma membrane aquaporins modulate their water channel activity. *The Plant Cell 16*, 215-228.

Fitzgibbon J., Bell K., King E. & Oparka K. (2010) Super-resolution imaging of plasmodesmata using three-dimensional structured illumination microscopy. *Plant Physiology 153*, 1453-1463.

Froelich D.R., Mullendore D.L., Jensen K.H., Ross-Elliott T.J., Anstead J.A., Thompson G.A., Pélissier H.C. & Knoblauch M. (2011) Phloem ultrastructure and pressure flow: Sieve-element-occlusion-related agglomerations do not affect translocation. *The Plant Cell 23*, 4428-4445.

Furch A.C., Hafke J.B., Schulz A. & van Bel A.J. (2007) Ca2 -mediated remote control of reversible sieve tube occlusion in vicia faba. *Journal of Experimental Botany 58*, 2827-2838.

Geiger D.R. & Sovonick S.A. (1975) Effects of temperature, anoxia and other metabolic inhibitors on translocation. In *Transport in Plants I* Effects of temperature, anoxia and other metabolic inhibitors on translocation. pp. 256-286. Springer.

Giaquinta R.T. & Geiger D.R. (1973) Mechanism of inhibition of translocation by localized chilling. *Plant Physiology 51*, 372-377.

Gong H., Peng Y., Zou C., Wang D., Xu Z. & Bai S. (2006) A simple treatment to significantly increase signal specificity in immunohistochemistry. *Plant Molecular Biology Reporter 24*, 93-101.

Gould N., Minchin P.E.H. & Thorpe M.R. (2004) Direct measurements of sieve element hydrostatic pressure reveal strong regulation after pathway blockage. *Functional Plant Biology 31*, 987-993.

Ham B. & Lucas W.J. (2014) The angiosperm phloem sieve tube system: A role in mediating traits important to modern agriculture. *Journal of Experimental Botany 65*, 1799-1816.

Hao P., Liu C., Wang Y., Chen R., Tang M., Du B., Zhu L. & He G. (2008) Herbivore-induced callose deposition on the sieve plates of rice: An important mechanism for host resistance. *Plant Physiology 146*, 1810-1820.

Hedrich R., Salvador-Recatalà V. & Dreyer I. (2016) Electrical wiring and long-distance plant communication. *Trends in Plant Science 21*, 376-387.

Hölttä T., Mencuccini M. & Nikinmaa E. (2009) Linking phloem function to structure: Analysis with a coupled xylem–phloem transport model. *Journal of Theoretical Biology 259*, 325-337.

Jaeger C.H., Goeschl J.D., Magnuson C.E., Fares Y. & Strain B.R. (1988a) Short-term responses of phloem transport to mechanical perturbation. *Physiologia Plantarum 72*, 588-594.

Jaeger C.H., Goeschl J.D., Magnuson C.E., Fares Y. & Strain B.R. (1988b) Short-term responses of phloem transport to mechanical perturbation. *Physiologia Plantarum 72*, 588-594.

Jensen K.H., Liesche J., Bohr T. & Schulz A. (2012) Universality of phloem transport in seed plants. *Plant, Cell & Environment 35*, 1065-1076.

Jensen K.H., Rio E., Hansen R., Clanet C. & Bohr T. (2009) Osmotically driven pipe flows and their relation to sugar transport in plants. *Journal of Fluid Mechanics 636*, 371-396.

Jensen K.H., Mullendore D.L., Holbrook N.M., Bohr T., Knoblauch M. & Bruus H. (2012a) Modeling the hydrodynamics of phloem sieve plates. *Frontiers in Plant Science 3*, 151.

Jensen K.H., Mullendore D.L., Holbrook N.M., Bohr T., Knoblauch M. & Bruus H. (2012b) Modeling the hydrodynamics of phloem sieve plates. *Frontiers in Plant Science 3*, 151.

Julia Kehr & Anja Buhtz. (2008) Long distance transport and movement of RNA through the phloem. *Journal of Experimental Botany* 59, 85-92.

Kammerloher W., Fischer U., Piechottka G.P. & Schäffner A.R. (1994) Water channels in the plant plasma membrane cloned by immunoselection from a mammalian expression system. *The Plant Journal : For Cell and Molecular Biology 6*, 187-199.

Knoblauch M., Froelich D.R., Pickard W.F. & Peters W.S. (2014) SEORious business: Structural proteins in sieve tubes and their involvement in sieve element occlusion. *Journal of Experimental Botany 65*, 1879-1893.

Knoblauch M., Knoblauch J., Mullendore D.L., Savage J.A., Babst B.A., Beecher S.D., Dodgen A.C., Jensen K.H. & Holbrook N.M. (2016) Testing the münch hypothesis of long distance phloem transport in plants. *Elife* 5, e15341.

Lang A. & Minchin P. (1986) Phylogenetic distribution and mechanism of translocation inhibition by chilling. *Journal of Experimental Botany 37,* 389-398.

Liesche J., Pace M.R., Xu Q., Li Y. & Chen S. (2017a) Height-related scaling of phloem anatomy and the evolution of sieve element end wall types in woody plants. *New Phytologist 214*, 245-256.

Liesche J., Pace M.R., Xu Q., Li Y. & Chen S. (2017b) Height-related scaling of phloem anatomy and the evolution of sieve element end wall types in woody plants. *New Phytologist 214*, 245-256.

Liesche J. & Patrick J. (2017) An update on phloem transport: A simple bulk flow under complex regulation. *F1000Research* 6.

Lucas W.J., Groover A., Lichtenberger R., Furuta K., Yadav S., Helariutta Y., He X., Fukuda H., Kang J., Brady S.M., Patrick J.W., Sperry J., Yoshida A., López-Millán A., Grusak M.A. & Kachroo P. (2013) The plant vascular system: Evolution, development and FunctionsF. *Journal of Integrative Plant Biology 55*, 294-388.

Luu D. & Maurel C. (2005) Aquaporins in a challenging environment: Molecular gears for adjusting plant water status. *Plant, Cell & Environment 28*, 85-96.

Maurel C., Boursiac Y., Luu D., Santoni V., Shahzad Z. & Verdoucq L. (2015) Aquaporins in plants. *Physiological Reviews 95*, 1321-58.

Maurel C., Reizer J., Schroeder J.I. & Chrispeels M.J. (1993) The vacuolar membrane protein gamma-TIP creates water specific channels in xenopus oocytes. *The EMBO Journal 12*, 2241-2247.

McNairn R.B. (1972) Phloem translocation and heat-induced callose formation in field-grown gossypium hirsutum L. *Plant Physiology 50*, 366-370.

Milburn J.A. (1974) Phloem transport in ricinus: Concentration gradients between source and sink. *Planta 117*, 303-319.

Minchin P. & Thorpe M.R. (1987) Measurement of unloading and reloading of photo-assimilate within the stem of bean. *Journal of Experimental Botany 38*, 211-220.

Minchin P. & Thorpe M.R. (1983) A rate of cooling response in phloem translocation. *Journal of Experimental Botany 34*, 529-536.

Mittler T.E. (1953) Amino-acids in phloem sap and their excretion by aphids. *Nature 172*, 207.

Muday G.K. & Brown-Harding H. (2018) Nervous system-like signaling in plant defense. *Science 361*, 1068-1069.

Mullendore D.L., Windt C.W., Van As H. & Knoblauch M. (2010) Sieve tube geometry in relation to phloem flow. *The Plant Cell 22*, 579-593.

Münch E. (1930) Die stoffbewegungen in der pflanze. *Gustav Fischer Verlagsb.Jena, Germany* p. 234.

Munson B.R., Young D.F., Okiishi T.H. & Heubsch W.W. (1990) Viscous flow in pipes. In: *Fundamentals of Fluid Mechanics.* pp- 504-517.

Payyavula R.S., Tay K.H.C., Tsai C. & Harding S.A. (2011) The sucrose transporter family in populus: The importance of a tonoplast PtaSUT4 to biomass and carbon partitioning. *The Plant Journal 65*, 757-770.

Phillips R.J. & Dungan S.R. (1993) Asymptotic analysis of flow in sieve tubes with semi-permeable walls. *Journal of Theoretical Biology 162*, 465-485.

Pickard W.F. & Minchin P. (1990) The transient inhibition of phloem translocation in phaseolus vulgaris by abrupt temperature drops, vibration, and electric shock. *Journal of Experimental Botany 41*, 1361-1369.

Rennie E.A. & Turgeon R. (2009) A comprehensive picture of phloem loading strategies. *Proceedings of the National Academy of Sciences 106*, 14162-14167.

Ross-Elliott T.J., Jensen K.H., Haaning K.S., Wager B.M., Knoblauch J., Howell A.H., Mullendore D.L., Monteith A.G., Paultre D. & Yan D. (2017) Phloem unloading in arabidopsis roots is convective and regulated by the phloem-pole pericycle. *Elife 6*, e24125.

Sack L., Streeter C.M. & Holbrook N.M. (2004) Hydraulic analysis of water flow through leaves of sugar maple and red oak. *Plant Physiology 134*, 1824-1833.

Sasaki T., Chino M., Hayashi H. & Fujiwara T. (1998) Detection of several mRNA species in rice phloem sap. *Plant & Cell Physiology* 39, 895-897.

Savage J.A., Beecher S.D., Clerx L., Gersony J.T., Knoblauch J., Losada J.M., Jensen K.H., Knoblauch M. & Holbrook N.M. (2017) Maintenance of carbohydrate transport in tall trees. *Nature Plants 3*, 965.

Schulte P.J. (2012) Computational fluid dynamics models of conifer bordered pits show how pit structure affects flow. *New Phytologist 193*, 721-729.

Schulte P.J., Hacke U.G. & Schoonmaker A.L. (2015) Pit membrane structure is highly variable and accounts for a major resistance to water flow through tracheid pits in stems and roots of two boreal conifer species. *New Phytologist 208*, 102-113.

Sevanto S. (2018) Drought impacts on phloem transport. *Current Opinion in Plant Biology 43*, 76-81.

Sevanto S. (2014) Phloem transport and drought. *Journal of Experimental Botany 65*, 1751-1759.

Sevanto S., McDowell N.G., Dickman L.T., Pangle R. & Pockman W.T. (2014) How do trees die? A test of the hydraulic failure and carbon starvation hypotheses. *Plant, Cell & Environment 37*, 153-161.

Sibaoka T. (1962) Excitable cells in mimosa. *Science 137*, 226.

Stanfield R.C., Hacke U.G. & Laur J. (2017) Are phloem sieve tubes leaky conduits supported by numerous aquaporins? *American Journal of Botany 104*, 719-732.

Thompson M.V. (2006a) Phloem: The long and the short of it. *Trends in Plant Science 11*, 26-32.

Thompson M.V. (2006b) Phloem: The long and the short of it. *Trends in Plant Science 11*, 26-32.

Thompson M.V. & Holbrook N.M. (2003a) Application of a single-solute non-steady-state phloem model to the study of long-distance assimilate transport. *Journal of Theoretical Biology 220*, 419-455.

Thompson M.V. & Holbrook N.M. (2003b) Scaling phloem transport: Water potential equilibrium and osmoregulatory flow. *Plant, Cell & Environment 26*, 1561-1577.

Thorpe M.R., Furch A.C., Minchin P.E., Foeller J., Van Bel A.J. & Hafke J.B. (2010) Rapid cooling triggers forisome dispersion just before phloem transport stops. *Plant, Cell & Environment 33*, 259-271.

Törnroth-Horsefield S., Wang Y., Hedfalk K., Johanson U., Karlsson M., Tajkhorshid E., Neutze R. & Kjellbom P. (2006) Structural mechanism of plant aquaporin gating. *Nature 439*, 688.

Turgeon R. (2010) The puzzle of phloem pressure. *Plant Physiology 154*, 578-581.

Tyree M.T. & Dainty J. (1975) Theoretical considerations. In *Transport in Plants I* Theoretical considerations. pp. 367-392. Springer.

Uehlein N., Otto B., Hanson D.T., Fischer M., McDowell N. & Kaldenhoff R. (2008) Function of nicotiana tabacum aquaporins as chloroplast gas pores challenges the concept of membrane CO2 permeability. *The Plant Cell 20*, 648-657.

Van Bel A. (2003) The phloem, a miracle of ingenuity. *Plant, Cell & Environment 26*, 125-149.

Walz C., Juenger M., Schad M. & Kehr J. (2002) Evidence for the presence and activity of a complete antioxidant defence system in mature sieve tubes. *The Plant Journal 31*, 189-197.

Young D.F., Munson B.R., Okiishi T.H. & Huebsch W.W. (2010) A brief introduction to fluid mechanics. John Wiley & Sons.

Zwiazek J.J., Xu H., Tan X., Navarro-Ródenas A. & Morte A. (2017) Significance of oxygen transport through aquaporins. *Scientific Reports 7*, 40411.

V. Super-resolution microscopy of phloem proteins

1. Introduction

Maturation of sieve elements is accompanied by a loss of autonomy, as the nucleus disintegrates, the protein synthesis machinery is degraded, and the Golgi and vacuole compartments dissolved. As depicted by TEM, ribosomes are spreading over the cytoplasm in the last stage of differentiation both, in experimentally induced wound phloem as well as in regular phloem of angiosperms and gymnosperms (Behnke and Sjolund 1990, Schulz 1986). Eventually, the sieve element cytoplasm only contains three types of organelles, sieve-element plastids, mitochondria and the peripheral ER. Structural and partially mobile phloem proteins present in the cytoplasm of mature sieve elements were assigned a role in sieve plate occlusion, able to prevent wound-induced exudation (Ernst et al. 2012, Knoblauch et al. 2014, Anstead et al. 2012, Froelich et al. 2011, Leineweber, Schulz & Thompson 2000, Golecki, Schulz & Thompson 1999, Golecki et al. 1998). The dramatic change of the cytoplasm in young nucleate sieve elements to the mictoplasm of mature sieve elements (Engleman 1965) might be considered a partial autophagy, but is not programmed cell *death*. Living sieve elements, and in particular the integrity of their plasma membrane, are a prerequisite for the osmotically generated pressure flow in the phloem. The sieve element plasma membrane seems to be maintained by active companion cells in angiosperms and Strasburger cells in gymnosperms that seem to have high metabolic and protein synthesising activity (van Bel and Knoblauch 2000, Liesche and Schulz 2018, Martens et al. 2006). Both sieve-element neighbours are well coupled to the sieve elements by pore-plasmodesma units. This pathway is used for sugar entry into the collection phloem, but is present along the entire transport phloem and, thus, offer a pathway for membrane protein and lipid transfer (Liesche and Schulz 2018, Mertens et al. 2006).

a. Phloem membrane proteins

One approach to solve the cell-biological question, how the sieve element plasma membrane is maintained by protein and lipid turnover, is given by identifying the role and localisation of phloem-specific membrane proteins. Among the most relevant proteins for this approach are the plasma membrane aquaporins (PIPs), the early-nodulin like protein 9 (ENODL9) and the companion-cell specific proton pump AHA3 (Stanfield et al. 2017, Laur and Hacke 2014, Almeida-Rodriguez and Hacke 2012, Ziomkiewicz et al. 2015, Khan et al. 2007, Ivashikina et al. 2003, DeWitt and Sussman 1995). A challenge for the localisation of the involved proteins is the resolution limits of wide-field and confocal microscopes, as the distance between companion cell and sieve element is just the thickness of one cell wall interface (around 200—700 nm). Moreover, the phloem is deeply embedded in the plant body, demanding physical sectioning of the plant material and making live imaging only possible in thin organs.

Super-resolution techniques have been introduced that bridge the gap between diffraction-limited fluorescence microscopy and electron microscopy (Bell and Oparka 2011, Klar et al. 2000, Gustafsson 2000, Betzig et al. 2006). Accordingly, they allow using FP reporter-gene constructs and/or doing immunolocalization to assess the distribution of relevant proteins in the phloem. From the three established techniques, three-dimensional structured illumination (3D-SIM) and single molecule localisation microscopy (SMLM) have been used in phloem research and have reached a lateral/axial resolution of 100/200 nm and 34/100 nm, respectively (Fitzgibbon et al. 2010, Stanfield, Hacke & Laur 2017, Ziomkiewicz et al. 2015). This equals an improvement in resolution of nearly 3 and 10 times, respectively, as compared to widefield fluorescence microscopy. The third technique, stimulated emission depletion, is less suitable for plant material, since the wavelength of the depletion laser is strongly absorbed by chloroplasts, limiting its application to chlorophyll-extracted material. According to our experience, 3D-SIM

allows doing 3D reconstructions of z-stacks up to 20 µm thickness and more. It can be used with any fluorescent protein or synthetic dye such as used for immunofluorescence. Because of its high applicability, we have limited the present super- resolution protocol to 3D-SIM; details for SMLM can be found in Ziomkiewicz et al. (2015).

b. Background of super-resolution microscopy

For an understanding of the super-resolution techniques, the reader is referred to the excellent reviews from Schermelleh, Heintzmann & Leonhardt 2010 and Huang, Bates & Zhuang (2009). In the context of the present protocol, the optical background of structural illumination and single molecule localisation microscopy is only briefly explained.

In structured illumination, the homogenous excitation light of widefield microscopes is replaced by a grid of dark and white lines with a spatial distance of some 200 nm in the focal plane. For 3D-SIM excitation light is not only scrambled in x and y, but also in the axial direction. During image acquisition, the grid cube is rotated 3 or 5 times and axially shifted in phase 5 times. Each single emission image shows the dark-bright patterns caused by the grid, but the 15 (or 25) images together allow the reconstruction of an evenly illuminated high-resolution image. The algorithms used for reconstruction take also neighbouring sections of an image stack in account, deconvoluting the objective-depending point-spread function and improving the resolution in all three axes (Gustafsson et al. 2008). As consequence, the diffraction-limited point-spread function of a widefield microscope with some 250 by 250 by 700 nm (xyz) is tailored to the 100 by 100 by 300 nm, achievable at blue wavelengths with a 3D-SIM microscope (Gustafsson et al. 2008, Schermelleh et al. 2008, Huang et al. 2009).

An even higher resolution can be achieved with SMLM, based on a separation in time of fluorescence blinks. Depending on the way fluorochromes are stimulated to blink, the technique is also known as STORM (stochastic optical reconstruction microscopy) and PALM (photoactivated localization microscopy) and variants thereof (Schermelleh et al. 2010). Single molecule resolution is achieved by the microscope camera which collects photons from a single blinking fluorochrome molecule. Because of inherent optical aberrations of objective lenses, a point light source is depicted as a cigar-shaped cloud after being refracted by the lens. The probability of photons hitting the centre decreases both laterally and axially (Huang et al. 2009). In SMLM, photons are counted over time. If labelling density is appropriate, the software can calculate the position of a molecule by constructing a centroid, based on a 2-D Gauss distribution. The coordinates of the centre of this centroid are given in a table together with the precision of this localisation. The table includes low and high precision values of all detected fluorochrome molecules, allowing the user to discard low precision values and, thus, chose the requested resolution (Schermelleh et al. 2010). The more photons are detected from one molecule, the better the achieved resolution. The challenge in SMLM is the right balance of labelling and/or photoactivation events: over-labelling means that neighbouring molecules have overlapping centroids and thus cannot be discriminated. A low labelling density results in lack of precision and low resolution. To collect a sufficient number of photons, the specimen might have to be recorded for 5-10 min. Only with additional optical elements can SMLM discriminate molecules in the z-axis. Therefore, it is very often combined with a near-field technique (total internal reflection excitation; TIRF). Here only a thin plane under the cover slip is excited and will emit photons. For plant cells it is crucial to adjust the TIRF excitation angle, so that excitation reaches the plasma membrane below the cell wall.

c. Examples of 3D-SIM and SMLM phloem imaging

Karl Oparka's lab was first to publish 3D-SIM images of mesophyll and phloem. Using antibodies and transformants expressing a viral movement protein-GFP fusion (MP) they could discriminate the callose-positive plasmodesmal neck region from the MP-positive median cavity in mesophyll plasmodesmata. Within the phloem, both sieve pores in sieve plates as well as the pore-plasmodesmata units were traversed by MP positive ER strands. Identity of the MP positive strands with the ER was proven with the ER-positive hexyl rhodamine B. The pore plasmodesma unit showed callose on the SE-side only, the PD branching from the median cavity in these connection were each characterised by a MP-positive ER strand (Fitzgibbon et al. 2010).

Water entering sieve elements make use of highly abundant aquaporins, water channels located in the sieve-element plasma membrane. In poplar trees, sieve elements were standing out with a dense labelling of the plasma membrane with the aquaporin PIP2 (Stanfield et al. 2017). 3D-SIM allowed to discriminate this labelling from the labelling of an internal membrane layer, most probably the sieve element reticulum (Stanfield et al. 2017). The present protocol is a detailed description of the different steps used in the poplar paper. Fig. 5-1A, shows a correctly adjusted single 3D-SIM image using the PIP1 and PIP2 antibodies. Fig. 5-1B is an example of an image with poor image reconstruction results; technical notes are included to increase the chances of recording a properly reconstructed image. For comparison, and ordinary confocal image is depicted in Fig. 5-1C. The same protocol can be applied to other plant species by adjusting the fixation times as well as concentration of primary antibodies.

The GPI-anchor protein ENODL9 of crucifers which exclusively occurs in the sieve element plasma membrane was visualised with SMLM, using directly, ALEXA-647 labelled monoclonal antibodies (Ziomkiewicz et al. 2015). ENODL9 forms elliptical nanodomains in the plasma

membrane, the diameter of which was automatically determined by a MatLab program to be some 110 by 157 nm. Automation prevents a manual selection of nanodomains that might be biased by circularity and a clear outline. This study concluded that specific lipid and protein composition of "raft platforms" (Linwood and Simons 2010) in the PM that are able to recruit membrane proteins, in particular GPI-anchor proteins (Raffaele et al. 2007, Jarsch et al. 2014).

2. Materials

a. Fixation, embedding, sectioning

1. Fixation Solution: Formaldehyde Acetic Acid (FAA) – 5% glacial acetic acid, 50% EtOH, 10% Formalin, 35% DI H_2O, chilled to 4°C (*see* **Note 1**)
2. Leica TP 1020 tissue processor (Leica Microsystems, Wetzlar, Germany) for paraffin embedding
3. Rotary microtome

b. Antibody labelling and Washing Solutions

1. Coverslip staining rack (Fisher Scientific, Pittsburgh, Pennsylvania)
2. Safeclear® Xylene Substitute (Fisher Scientific) for dewaxing
3. Ethanol series: 100%, 95%, 85%, 70%, 50%, 30% ethanol (EtOH)
4. Phosphate Buffered Saline (PBS; 10x concentrate): to 800ml of Double Distilled H_2O, add 80g NaCl, 2.0g of KCl, 14.4g of Na_2HPO_4 and 2.4g KH_2PO_4. Adjust pH to 7.2, bring volume to 1000ml with more Double Distilled H_2O. Dilute a working solution to 1:10 in Double Distilled H_2O
5. PBS with Proteinase-K: 10 µl of 20 mg/ml Proteinase K (Promega, Madison, Wisconsin, USA) in 200 ml PBS
6. Post-fixative: PBS buffered FAA - 10% PBS solution in FAA

7. Blocking Solution (BS): PBS with 0.1% Tween 20 detergent, 1.5% Glycine, and 5% (w/v) Bovine Serum Albumin (BSA)
8. Washing Solution: Low salt Washing Buffer (LWB) - PBS with 0.8% NaCl, 0.8% BSA, and 0.1% Tween 20 detergent (Sigma-Aldrich, Oakville, Ontario, Canada)
9. Parafilm

c. Antibody solutions

1. Primary antibodies: Plasma membrane Intrinsic Protein (PIP1 and PIP2) (*see* **Note 2**) diluted to 1/80 concentration in BS
2. Secondary antibodies: Pre-absorbed (*see* **Note 3**) [1/100] Alexa Fluor (Fisher Scientific) 488 conjugated goat anti-mouse (PIP2 detection) and Alexa Fluor 568 conjugated goat anti-chicken (for PIP1 detection) diluted to [1/5] in BS

d. Coverslip and mounting medium

1. Number 1.5 coverslip (22 x 22mm) coated in 0.01% poly-l-lysine solution (see methods)
2. Slow Fade Gold (Fisher Scientific) mounting medium. For super resolution microscopy, ensure there is no DAPI in mounting medium
3. Nail polish for sealing coverslip to slide

e. Microscope

1. 3D-SIM enabled microscope such as Deltavision OMX or Zeiss Elyra S1 (see **Note 4**)

2. Manufacturer-supplied software for imaging and image reconstruction

3. Methods

a. Fixation and embedding

1. Cut 1 cm samples of root, stem, petiole or leaf (1 x 1cm) with a fresh razor blade. For this protocol, longitudinal sections of balsam poplar (*Populus balsamifera L.*) were used.
2. Wash samples if needed in deionized water, if needed (e.g., root samples covered in soil).
3. Immediately after cutting, place samples into cool FAA (4°C), over ice, for 30 mins.
4. Change out FAA with fresh cool FAA, and keep at 4°C.
5. After six hours, again replace with additional fresh cool FAA and keep at 4°C overnight (*see* **Note 5**).
6. The next day, put samples into 50% EtOH (~5 mins), then 70% EtOH.
7. Keep in 70% EtOH at 4°C until ready to begin paraffin embedding.
8. Using preferred tissue processor, infiltrate tissue with paraffin wax. After overnight paraffin processing, embed the organ sample in mould. The organ can be oriented in a transverse or longitudinal orientation within the mould.

b. Coverslip preparation

1. Wash coverslip with 100% EtOH (5 mins).
2. Wash coverslip with deionized water (5 mins).
3. Let coverslip dry.
4. Immerse coverslip in 0.01% poly-l-lysine (5 mins).
5. Quickly wash three times in deionized water.
6. Let coverslip dry.

c. Sectioning

1. After paraffin block has cooled, place cutting face down onto ice.
2. Set the rotary microtome to a cutting thickness of 7µm.

3. Place poly lysine coated coverslip directly on slide warmer and set to 37°C. Flood coverslip with deionized water.
4. Cut paraffin sections on microtome and gently place on top of water pool above the coverslip.
5. Let the wax section spread out on top of the water until wrinkles are gone. Remove excess water via pipette.
6. Let section dry onto coverslip for at least 24 hours on the slide warmer (37°C) (*see* **Note 6**).

d. Antibody labelling

Day 1:

1. Preheat PBS containing proteinase-K solution to 37°C.
2. Begin antibody labelling (following the procedure of Gong et al. 2006) by dewaxing using xylene or xylene substitute for 10 mins, twice. The use of a coverslip staining rack will facilitate the transfer of the coverslip from one solution to the next.
3. Place coverslip through ethanol series for 5 mins each for each concentration of ethanol (100%, 95%, 85%, 70%, 50%, 30%).
4. Wash coverslip in PBS twice, each for 5 mins.
5. Incubate coverslip in PBS containing proteinase-K for 30 mins at 37°C.
6. Wash coverslip in PBS three times, each for 10 mins.
7. Immerse coverslip in post-fixative for 15 mins.
8. Wash in PBS three times, each for 10 mins.
9. Place coverslip in blocking solution for 45 mins.
10. Briefly wash coverslip in LWB.

11. Wipe excess solution off the underside of coverslip (opposite of tissue section), but do not allow side with tissue to dry out. Being sure that the coverslip is positioned in a horizontal orientation, apply 40 – 50 µl of primary antibody. Apply a small piece of parafilm over the coverslip (just enough to cover the coverslip area). Place coverslip back into coverslip staining rack. Wrap the entire coverslip staining rack in parafilm to ensure coverslip does not dry out.
12. Let samples incubate at 4°C for 16 – 24 hours. Be sure to orient coverslip staining rack in a horizontal position to prevent antibody solution from leaking.

Day 2:

1. The next day, remove primary antibodies by rinsing coverslip briefly in LWB, three times.
2. Incubate again in fresh LWB twice, each for 15 mins.
3. Wash coverslip in PBS once for 15 mins.
4. Wipe away excess solution from bottom of coverslip. Apply 40 – 50µl of secondary antibodies to coverslip, apply parafilm (as done before with primary antibodies) and return coverslip to staining rack. Wrap entire staining rack in parafilm and let incubate at room temperature for 4 hours.
5. Remove secondary antibodies by rinsing briefly in LWB three times, followed by 15 mins in PBS.
6. Rinse coverslip in double distilled H_2O, wipe off any extra solution.
7. Place 40 - 50µl of liquid mounting medium onto coverslip. Place tissue side down onto a microscope slide.
8. Seal coverslip to the middle of the slide using nail polish.

e. 3D-SIM Imaging

1. Ensure slides are free of debris and apply the appropriate immersion oil directly above specimen on coverslip (immersion oil with a refractive index of 1.514 was used in this protocol).
2. Clean microscope lens with chloroform, if needed.
3. Locate the tissue sample on the slide. Use the conventional light source for this process so as not to photo-bleach tissue prematurely. When using the Deltavision OMX, use the mosaic tool to quickly scan and view a large area of tissue and narrow in on the phloem.
4. Switch light source to structured illumination (SI). Set laser power to 1%, and exposure times to 100 – 200ms. Set the sample thickness to 0.5µm before attempting a thicker z-stack (*see* **Note 7**). For the Zeiss Elyra system, choose the grating that fits the objective and tissue thickness. Select 5 grating rotations and 5 phase-changes for each section.
5. Intensity counts on the resulting image should be between 2000 – 4000 for best image reconstruction (*see* **Note 8**).
6. Once images have been captured, use the image reconstruction software supplied by the manufacturer to perform Structured Illumination Reconstruction. Under the options for SI reconstruction, select a Wiener filter of 0.001 for smoothing noise of image. Keep all other settings to their default. If reconstruction is poor, increasing the filter value may be advantageous at the expensive of decreased resolution.
7. A proper image (Fig. 5-1A) should show sharp lines between visible objects. An image showing poor reconstruction (Fig. 5-1B) will show cellular features with lines less sharp (i.e., poor resolution) even in comparison to confocal imaging (Fig. 5-1C).

8. If wanting a 3D view, use the software's volume viewer to visualize the SI reconstructed output in rotation.

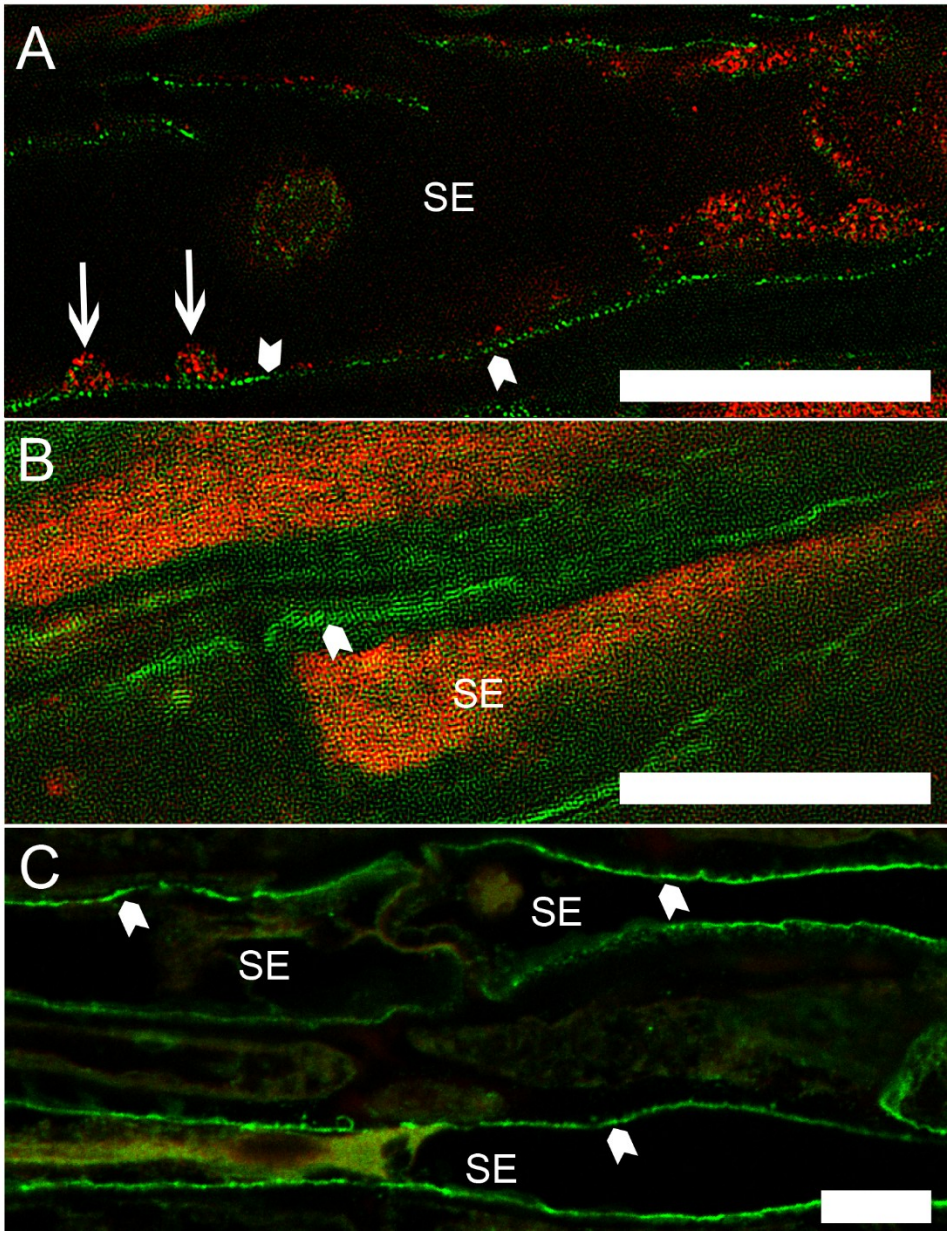

Figure 5-1: Imaging of sieve elements in longitudinal view from stem tissue of balsam poplar with PIP1 (red) and PIP2 (green) immuno-labelling. (A) An example image of a properly reconstructed 3D-SIM image. Note how individual units of PIP2 fluorophore can be discerned at the plasma membrane (arrowheads) within the sieve element (SE). Also detected is the formation of a budding vesicle from the plasma membrane, enriched with PIP proteins (arrows). (B) An example of an image that was not properly reconstructed in 3D-SIM. The resolution is quite poor, even more so than confocal imaging. (C) A comparison image showing a confocal laser scanning micrograph. Scale bar = 10µm.

4. Notes

1. For the viewing of fine endomembrane structures like the endoplasmic reticulum, a gentler fixation procedure is recommended. For this protocol, see Bell, Oparka & Knox (2018).
2. The *At*PIP1 antibodies used were designed for *Arabidopsis thaliana* but have confirmed reactivity in *Populus balsamifera* (see Stanfield et al. 2017). The PIP2 antibodies were designed to target the conserved 10 amino acid sequence of the c-terminus of the protein and had reactivity with PIP2 proteins of *Populus balsamifera* (see Stanfield et al. 2018). When using antibodies designed to target different epitopes, the same procedure may be used except for possibly needing to decrease the primary antibody concentration.
3. The pre-absorption of secondary antibodies means to incubate the supplied antibody solution in plant material obtained from your test species (as performed in Gong et al. 2006). This technique will significantly improve the signal to noise ratio in the resulting fluorescent image. To pre-absorb secondary antibodies, pulverise leaves and stems in acetone using a mortar and pestle while applying small amounts of liquid nitrogen. Once ground to a powder, add more acetone and allow material to dry overnight on filter paper at 4°C. The next day, resuspend powder in acetone and centrifuge at 10000rcf. Remove supernatant and repeat 2 or 3 times or until chlorophyll is removed from the pellet. Save pellet and allow to air-dry on filter paper. Add ~30mg of the resulting dried powder to 400µl of BS with 10µl of the secondary antibody and incubate at room temperature for 24hrs in a darkened

cabinet. The next day add 600µl of PBS and centrifuge at 10000rcf for 5min at 4°C. The resulting supernatant is the [1/100] pre-absorbed solution.

4. This protocol was tested on the Deltavision OMX and Zeiss Elyra PS1. However, it should also be easy to adapt to other 3D-SIM capable microscopes. It may also be used with confocal microscopy, apart from adhering tissue directly to slides instead of cover glass.
5. For woody stems, it is recommended to keep samples in FAA for up to one week to maintain better section quality. However, too much fixation time may degrade proteins, so caution must be taken.
6. Applying heat to the coverslip helps tissue adherence through the antibody labelling process. If by the end of the labelling process tissue starts to fall off the coverslip, heat future samples to 50°C for up to one hour in a drying oven prior to beginning the labelling process.
7. A thicker z-stack (number of images taken in the z-axis) will increase the possibility that the fluorophore on the secondary antibody will bleach. If photo bleaching occurs, this will diminish the ability for the software to perform proper image reconstruction. A symptom of this will be progressively lower intensity counts from the top of the z-stack towards the bottom. If this occurs, try lowering the z-stack thickness in the capturing software.
8. If intensity counts fall well outside the range of 2000 – 4000 (on average), then SI image reconstruction likely will turn out poor. If this is the case, it is recommended to sample another area of the tissue, change immersion oil, or try using another sample slide. Lower or higher intensity counts may be acceptable if the variance of

the intensity counts of images collected on the same z-plane is low (i.e., a range of min/max values within 2000 counts, on average). For the Elyra system, laser power may be increased as it is not as sensitive to photo bleaching effects as the OMX. If results continue to be poor, the microscope may need calibration, or the secondary antibody may need to be replaced and/or primary antibody concentrations adjusted.

5. References

Almeida-Rodriguez A.M., Hacke U.G. (2012) Cellular Localization of Aquaporin Mrna in Hybrid Poplar Stems. *Am J Bot 99*, 1249-1254.

Anstead J.A., Froelich D.R., Knoblauch M., Thompson G.A. (2012) Arabidopsis P-Protein Filament Formation Requires Both AtSEOR1 and AtSEOR2. *Plant and Cell Physiology 53*, 1033-1042.

Behnke H.D., Sjolund R.D., eds. (1990) Sieve Elements - Comparative structure, induction and development. Springer Berlin Heidelberg. doi:10.1007/978-3-642-74445-7

Bell K., Oparka K. (2011) Imaging plasmodesmata. *Protoplasma 248*, 9-25.

Bell K., Oparka K., Knox K. (2018) Preparation and Imaging of Specialized ER Using Super-Resolution and TEM Techniques. In: Hawes C, Kriechbaumer V (eds) The Plant Endoplasmic Reticulum : Methods and Protocols. Springer New York, New York, NY, pp 33-42.

Betzig E., Patterson G.H., Sougrat R., Lindwasser O.W., Olenych S., Bonifacino J.S., Davidson M.W., Lippincott-Schwartz J., Hess H.F. (2006) Imaging Intracellular Fluorescent Proteins at Nanometer Resolution. *Science 313*, 1642-1645.

DeWitt N.D., Sussman M.R. (1995) Immunocytological localization of an epitope-tagged plasma membrane proton pump (H+-ATPase) in phloem companion cells. *Plant Cell 7*, 2053-2067.

Engleman E.M. (1965) Sieve Element of Impatiens Sultanii2. Developmental Aspects. *Ann Bot-London 29*, 103-104.

Ernst A.M., Jekat S.B., Zielonka S., Muller B., Neumann U., Ruping B., Twyman R.M., Krzyzanek V., Prufer D., Noll G.A. (2012) Sieve element occlusion (SEO) genes encode structural phloem proteins involved in wound sealing of the phloem. *P Natl Acad Sci USA 109*, E1980-E1989.

Fitzgibbon J., Bell K., King E., Oparka K. (2010) Super-Resolution Imaging of Plasmodesmata Using Three-Dimensional Structured Illumination Microscopy. *Plant Physiol 153*, 1453-1463.

Froelich D.R., Mullendore D.L., Jensen K.H., Ross-Elliott T.J., Anstead J.A., Thompson G.A., Pélissier H.C., Knoblauch M. (2011) Phloem Ultrastructure and Pressure Flow: Sieve-Element-Occlusion-Related Agglomerations Do Not Affect Translocation. *Plant Cell 23*, 4428-4445.

Golecki B., Schulz A., Thompson G.A. (1999) Translocation of structural P proteins in the phloem. *Plant Cell 11*, 127-140.

Golecki B., Schulz A., Carstens-Behrens U., Kollmann R. (1998) Evidence for graft transmission of structural phloem proteins or their precursors in heterografts of Cucurbitaceae. *Planta 206*, 630-640.

Gong H.Q., Peng Y.B., Zou C., Wang D.H., Xu Z.H., Bai S.N. (2006) A simple treatment to significantly increase signal specificity in immunohistochemistry. *Plant Mol Biol Rep* 24, 93-101.

Gustafsson M.G. (2000) Surpassing the lateral resolution limit by a factor of two using structured illumination microscopy. *J Microsc 198*, 82-87

Gustafsson M.G., Shao L., Carlton P.M., Wang C.J., Golubovskaya I.N., Cande W.Z., Agard D.A., Sedat J.W. (2008) Three-dimensional resolution doubling in wide-field fluorescence microscopy by structured illumination. *Biophysical journal 94*, 4957-4970.

Huang B., Bates M., Zhuang X.W. (2009) Super-Resolution Fluorescence Microscopy. *Annual Review of Biochemistry 78*, 993-1016.

Ivashikina N., Deeken R., Ache P., Kranz E., Pommerrenig B., Sauer N., Hedrich R. (2003) Isolation of AtSUC2 promoter-GFP-marked companion cells for patch-clamp studies and expression profiling. *Plant J 36*, 931-945

Jarsch I.K., Konrad S.S.A., Stratil T.F., Urbanus S.L., Szymanski W., Braun P., Braun K.H., Ott T. (2014) Plasma Membranes Are Subcompartmentalized into a Plethora of Coexisting and Diverse Microdomains in Arabidopsis and Nicotiana benthamiana. *Plant Cell 26*, 1698-1711.

Khan J.A., Wang Q., Sjolund R.D., Schulz A., Thompson G.A. (2007) An early nodulin-like protein accumulates in the sieve element plasma membrane of Arabidopsis. *Plant Physiol 143*, 1576-1589.

Klar T.A., Jakobs S., Dyba M., Egner A., Hell S.W. (2000) Fluorescence microscopy with diffraction resolution barrier broken by stimulated emission. *Proceedings of the National Academy of Sciences 97*, 8206-8210.

Knoblauch M., Froelich D.R., Pickard W.F., Peters W.S. (2014) SEORious business: structural proteins in sieve tubes and their involvement in sieve element occlusion. *J Exp Bot 65*, 1879-1893.

Laur J., Hacke U.G. (2014) Exploring Picea glauca aquaporins in the context of needle water uptake and xylem refilling. *New Phytol 203*, 388-400.

Leineweber K., Schulz A., Thompson G.A. (2000) Dynamic transitions in the translocated phloem filament protein. *Australian Journal of Plant Physiology 27*, 733-741.

Liesche J., Schulz A. (2018) Phloem transport in gymnosperms: a question of pressure and resistance. *Curr Opin Plant Biol 43*, 36-42.

Lingwood D., Simons K. (2010) Lipid rafts as a membrane-organizing principle. *Science 327*, 46-50.

Martens H.J., Roberts A.G., Oparka K.J., Schulz A. (2006) Quantification of plasmodesmatal endoplasmic reticulum coupling between sieve elements and companion cells using fluorescence redistribution after photobleaching. *Plant Physiol 142*, 471-480.

Raffaele S., Mongrand S., Gamas P., Niebel A., Ott T. (2007) Genome-wide annotation of remorins, a plant-specific protein family: Evolutionary and functional perspectives. *Plant Physiol 145*, 593-600.

Schermelleh L., Carlton P.M., Haase S., Shao L., Winoto L., Kner P., Burke B., Cardoso M.C., Agard D.A., Gustafsson M.G.L., Leonhardt H., Sedat J.W. (2008) Subdiffraction multicolor imaging of the nuclear periphery with 3D structured illumination microscopy. *Science 320,*1332-1336.

Schermelleh L., Heintzmann R., Leonhardt H. (2010) A guide to super-resolution fluorescence microscopy. *The Journal of cell biology 190*, 165-175.

Schulz A. (1986) Wound phloem in transition to bundle phloem in primary roots of Pisum sativum L. .1. Development of bundle-leaving wound-sieve tubes. *Protoplasma 130*, 12-26.

Stanfield R.C., Hacke U.G., Laur J. (2017) Are phloem sieve tubes leaky conduits supported by numerous aquaporins? *Am J Bot 104*, 719-732.

van Bel A.J.E., Knoblauch M. (2000) Sieve element and companion cell: the story of the comatose patient and the hyperactive nurse. *Australian Journal of Plant Physiology 27*, 477-487.

Ziomkiewicz I., Sporring J., Pomorski T.G., Schulz A. (2015) Novel approach to measure the size of plasma-membrane nanodomains in single molecule localization microscopy. Cytometry Part A 87A, 868-877.

VI. General discussion and conclusions

1. Outcomes of this study

This study sought to enhance our understanding of aquaporins in the phloem of a tree species, how they respond to an environmental disturbance, and to characterize specific sieve plate traits and radial water flows.

Using immunolabeling techniques I found that PIP1 and PIP2 water channels occur in the phloem of balsam poplar (**Chapter 2**). I usually found the PIP2s in the plasma membrane of sieve tubes (not or rarely in companion cells). PIP1s by contrast often occurred within internal compartments of sieve tubes. These aquaporins occurred throughout the entire transport pathway of the phloem.

Since the localization pattern of these aquaporins differed between the two aquaporin subfamilies within sieve tubes, a cold block experiment was performed to determine if localization patterns would change (**Chapter 3**). I did not find significant differences in the cellular location of the PIP1 and PIP2 aquaporins due to the cold block treatment. However, it was found that aquaporin mRNA transcript abundance was altered, and that the protein signal was transiently enhanced within sieve tubes in response to cold. This study adds to our knowledge about how the sieve tube responds to chilling. Past studies have shown that the sieve tubes respond by building up pressure, but then quickly release this pressure under chilling conditions. In this chapter I found that the water channel increase provides the possible explanation that aquaporins help to release pressure through the rapid removal of water.

In the next study, Comsol Multiphysics software and mathematical modeling tools were used to assess sieve plate structure as well as the influence of radial water inflows on axial transport in the sieve tube (**Chapter 4**). Here I found that the sieve plates are responsible for up to 85% of the overall sieve tube resistance. I also found that sieve plate pores which deviate from

circular pores substantially increased resistance. This last finding is important because previous phloem models always assume sieve plate pores are perfectly round, which is not always the case. To integrate the results of aquaporins in sieve tubes, we performed a modeling study which assessed the impact of radial water flow on the axial transport of phloem sap. We found that by allowing sieve tubes to be permeable, this helped to reduce pressure gradients by half in comparison to tubes that did not allow for radial inflows.

The final chapter was about the methodology of using immuno-histochemistry techniques in conjunction with super-resolution microscopy to view phloem tissue (**Chapter 5**). Combining previously available protocols, and providing valuable troubleshooting tips, this chapter outlines the techniques needed to carefully prepare phloem tissue sections tagged with antibodies of the researcher's choice. Once slides are prepared, techniques and troubleshooting tips are outlined to increase the chances of visualizing phloem tissue in resolutions down to 100nm.

2. Outlook and future studies

The overarching theme of the current work is the consideration that aquaporins may help facilitate the function and reaction of the phloem sieve tube in both normal and challenging conditions (**Chapters 2 and 3**). Further, sieve plate morphology was shown to be variable, and may change quickly in response to environmental stimuli through the accumulation of callose on the plate (**Chapter 4**). In addition, the impact of radial water flows on axial translocation seems to be a promising future avenue of research, especially in tree species. The research points to the idea that far from being static, the sugar conducting sieve tube can respond dynamically to disturbances in the environment.

Looking forward, there are many questions related to cell biology that arise from the results of the current study. Within a slice of a tissue section, it was observed that PIP1s and PIP2s may locate predominately within internal compartments, plasma membrane, or equally in both. Although it was not found that diurnal cycle or cold (**Chapters 2 and 3**) change this localization pattern, it is possible that the methodology used to detect a difference was not significantly robust to identify changes. For example, it may be of value to use super-resolution microscopy (as outlined in **Chapter 5**) to count the number of invaginations of the plasma membrane in response to an environmental stimulus. Future work will also have to address what kind of environmental stimuli (e.g., physical wounding, insect attack, cold, etc.) dictate this sub-cellular trafficking to the greatest extent. Further, it is unknown how aquaporins are shuttled between internal compartments and the plasma membrane within sieve tubes. Sieve tubes lack the cytoskeletal organelles that most cells possess which are used to move organelles and vesicles to different positions. How does the sieve tube manage to get aquaporins from internal compartments to the plasma membrane without this trafficking infrastructure? Future work may use immunolabeling techniques to identify other cytoskeletal elements that could be used to perform this task.

At the phloem physiological level, the occurrence of aquaporins throughout the transport conduit of the sieve tube in balsam poplar opens a plethora of questions that need to be addressed. First, what is the consequence of having consistent and significant radial transport of water in the transport phloem? From the modeling work of this study (**Chapter 4**), pressure gradients are reduced due to this radial influx of water. Intuitively this makes sense; if water can be allowed to gradually enter along the transport system, instead of all at once at the source, the pressure need not be as high to support translocation. One criticism of this idea is that aquaporins

are only passive water channels and allow the movement of water to occur only by facilitated osmosis. Therefore, the sieve tube conduit and surrounding phloem tissue would have to be at a constant water potential disequilibrium to facilitate this radial exchange. Future studies need to thoroughly assess if and under what conditions, the transport conduit exists at an osmotic disequilibrium. This dynamic response to maintaining an optimal pressure gradient may be especially important in times of drought, where competition from water in the xylem may disrupt the pressure gradient of the phloem. This idea leads to another testable question of how interconnected the phloem and xylem are in terms of their water sharing capacity along the transport pathway? (Can this water sharing ability be turned on or off dynamically in response to drought?) Testing these questions experimentally may look at the alteration of aquaporin signals in xylem and phloem ray cells, as well as gaining a better understanding of the plasmodesmata connections that unite the two tissues symplastically.

The last future work entails the structurally important sieve plate. This end wall structure that acts as the partition to sieve elements still has many unresolved questions. Callose sugars and p-protein accumulate on the sieve plate in the event of a damaged conduit. However, it is not well known all the environmental stresses that may cause callose accumulation on plates. For example, does abiotic stress such as wind or cold cause sieve plate blockage with callose? What about from insect or viral attack? Also, do sieve tubes that persist over multiple seasons have sieve plates that remain open over the winter, or do they become blocked, only to reopen in the spring? Thus, future studies on sieve plates may look at a variety of abiotic and biotic environmental disturbances that may cause sieve plate blockage. As the phloem is the energy pipeline for the plant, and is directly responsible for growth, a wide variety of researchers may be

interested in knowing what disturbances may cause the dynamic sieve tube to become open or blocked.

References

Ahamed A., Murai-Hatano M., Ishikawa-Sakurai J., Hayashi H., Kawamura Y. & Uemura M. (2012) Cold stress-induced acclimation in rice is mediated by root-specific aquaporins. *Plant and Cell Physiology 53*, 1445-1456.

Almeida-Rodriguez A. M., & Hacke, U. G. (2012). Cellular localization of aquaporin mRNA in hybrid poplar stems. *American Journal of Botany 99*, 1249-1254.

Almeida-Rodriguez A. M., Cooke, J. E., Yeh, F., & Zwiazek, J. J. (2010). Functional characterization of drought-responsive aquaporins in Populus balsamifera and Populus simonii× balsamifera clones with different drought resistance strategies. *Physiologia Plantarum 140*, 321-333.

Almeida-Rodriguez A.M., Hacke U.G. (2012) Cellular Localization of Aquaporin Mrna in Hybrid Poplar Stems. *Am J Bot 99*, 1249-1254.

Alonso A., Queiroz C.S. & Magalhães A.C. (1997) Chilling stress leads to increased cell membrane rigidity in roots of coffee (coffea arabica L.) seedlings. *Biochimica Et Biophysica Acta (BBA)-Biomembranes 1323*, 75-84.

Anstead J.A., Froelich D.R., Knoblauch M., Thompson G.A. (2012) Arabidopsis P-Protein Filament Formation Requires Both AtSEOR1 and AtSEOR2. *Plant and Cell Physiology 53*, 1033-1042.

Aroca R., Amodeo G., Fernández-Illescas S., Herman E.M., Chaumont F. & Chrispeels M.J. (2005) The role of aquaporins and membrane damage in chilling and hydrogen peroxide induced changes in the hydraulic conductance of maize roots. *Plant Physiology 137*, 341-353.

Behnke H.D., Sjolund R.D., eds. (1990) Sieve Elements - Comparative structure, induction and development. Springer Berlin Heidelberg. doi:10.1007/978-3-642-74445-7

Bell K., Oparka K. (2011) Imaging plasmodesmata. *Protoplasma 248*, 9-25.

Bell K., Oparka K., Knox K. (2018) Preparation and Imaging of Specialized ER Using Super-Resolution and TEM Techniques. In: Hawes C, Kriechbaumer V (eds) The Plant Endoplasmic Reticulum: Methods and Protocols. Springer New York, New York, NY, pp 33-42.

Betzig E., Patterson G.H., Sougrat R., Lindwasser O.W., Olenych S., Bonifacino J.S., Davidson M.W., Lippincott-Schwartz J., Hess H.F. (2006) Imaging Intracellular Fluorescent Proteins at Nanometer Resolution. *Science 313*, 1642-1645.

Bilska-Kos A., Szczepanik J. & Sowiński P. (2016) Cold induced changes in the water balance affect immunocytolocalization pattern of one of the aquaporins in the vascular system in the leaves of maize (zea mays L.). Journal of *Plant Physiology 205*, 75-79.

Boursiac Y., Chen S., Luu D., Sorieul M., van den Dries N. & Maurel C. (2005) Early effects of salinity on water transport in arabidopsis roots. molecular and cellular features of aquaporin expression. *Plant Physiology 139*, 790-805.

Brunner, A. M., Yakovlev, I. A., & Strauss, S. H. (2004). Validating internal controls for quantitative plant gene expression studies. *BMC plant biology 4*, 14.

Cabrita P., Thorpe M. & Huber G. (2013) Hydrodynamics of steady state phloem transport with radial leakage of solute. *Frontiers in Plant Science 4*, 531.

Cayla T., Batailler B., Le Hir R., Revers F., Anstead J.A., Thompson G.A., Grandjean O. & Dinant S. (2015) Live imaging of companion cells and sieve elements in arabidopsis leaves. *PloS One 10*, e0118122.

Chaumont F. & Tyerman S.D. (2014) Aquaporins: Highly regulated channels controlling plant water relations. *Plant Physiology 164*, 1600-1618.

Chevalier A.S. & Chaumont F. (2015) Trafficking of plant plasma membrane aquaporins: Multiple regulation levels and complex sorting signals. *Plant & Cell Physiology 56*, 819-829.

Chisholm S.T., Parra M.A., Anderberg R.J. & Carrington J.C. (2001) Arabidopsis RTM1 and RTM2 genes function in phloem to restrict long-distance movement of tobacco etch virus. *Plant Physiology 127*, 1667-1675.

Christy A.L. & Ferrier J.M. (1973) A mathematical treatment of munch's pressure-flow hypothesis of phloem translocation. *Plant Physiology 52*, 531-538.

Clark G. (1981) Staining procedures. In Staining Procedures Staining procedures. William & Wilkins.

Comtet J., Jensen K.H., Turgeon R., Stroock A.D. & Hosoi A.E. (2017) Passive phloem loading and long-distance transport in a synthetic tree-on-a-chip. *Nature plants 3*, 17032

Comtet J., Turgeon R. & Stroock A.D. (2017) Phloem loading through plasmodesmata: A biophysical analysis. *Plant Physiology 175*, 904.

De Schepper V., De Swaef T., Bauweraerts I. & Steppe K. (2013) Phloem transport: A review of mechanisms and controls. *Journal of Experimental Botany 64*, 4839-4850.

DesRochers A. & Thomas B. (2003a) A comparison of pre-planting treatments on hardwood cuttings of four hybrid poplar clones. *New Forests 26*, 17-32.

DeWitt N.D., Sussman M.R. (1995) Immunocytological localization of an epitope-tagged plasma membrane proton pump (H+-ATPase) in phloem companion cells. *Plant Cell 7*, 2053-2067.

Dixon H.H. (1914) Transpiration and the ascent of sap in plants. In: plants. Macmillan and Company, limited.

Engleman E.M. (1965) Sieve Element of Impatiens Sultanii2. Developmental Aspects. *Ann Bot-London 29*, 103-104.

Ernst A.M., Jekat S.B., Zielonka S., Muller B., Neumann U., Ruping B., Twyman R.M., Krzyzanek V., Prufer D., Noll G.A. (2012) Sieve element occlusion (SEO) genes encode structural phloem proteins involved in wound sealing of the phloem. *P Natl Acad Sci USA 109*, E1980-E1989.

Esau K. & Thorsch J. (1985) Sieve plate pores and plasmodesmata, the communication channels of the symplast: Ultrastructural aspects and developmental relations. American Journal of Botany 72, 1641-1653.

Esau K. (1939) Development and structure of the phloem tissue. Botanical Review 5, 373-432.

Eschrich W., Evert R.F. & Young J.H. (1972) Solution flow in tubular semipermeable membranes. *Planta 107*, 279-300.

Fetter K., Van Wilder V., Moshelion M. & Chaumont F. (2004) Interactions between plasma membrane aquaporins modulate their water channel activity. *The Plant Cell 16*, 215-228.

Fischer G., Kosinska-Eriksson U., Aponte-Santamaría C., Palmgren M., Geijer C., Hedfalk K., Hohmann S., De Groot B.L., Neutze R. & Lindkvist-Petersson K. (2009) Crystal structure of a yeast aquaporin at 1.15 Å reveals a novel gating mechanism. *PLoS Biology 7*, e1000130.

Fitzgibbon J., Bell K., King E. & Oparka K. (2010) Super-resolution imaging of plasmodesmata using three-dimensional structured illumination microscopy. *Plant Physiology 153*, 1453-1463.

Fraysse L.C., Wells B., McCann M.C. & Kjellbom P. (2005) Specific plasma membrane aquaporins of the PIP1 subfamily are expressed in sieve elements and guard cells. *Biology of the Cell 97*, 519-534.

Froelich D.R., Mullendore D.L., Jensen K.H., Ross-Elliott T.J., Anstead J.A., Thompson G.A., Pélissier H.C. & Knoblauch M. (2011) Phloem ultrastructure and pressure flow: Sieve-element-occlusion-related agglomerations do not affect translocation. *The Plant Cell 23*, 4428-4445.

Furch A.C., Hafke J.B., Schulz A. & van Bel A.J. (2007) Ca2 -mediated remote control of reversible sieve tube occlusion in vicia faba. *Journal of Experimental Botany 58*, 2827-2838.

Gamalei Y. (1991) Phloem loading and its development related to plant evolution from trees to herbs. *Trees 5*, 50-64.

Geiger D.R. & Sovonick S.A. (1975) Effects of temperature, anoxia and other metabolic inhibitors on translocation. In: Transport in Plants 1, pp- 256-286.

Giaquinta R.T. & Geiger D.R. (1973) Mechanism of inhibition of translocation by localized chilling. *Plant Physiology 51*, 372-377.

Golecki B., Schulz A., Carstens-Behrens U., Kollmann R. (1998) Evidence for graft transmission of structural phloem proteins or their precursors in heterografts of Cucurbitaceae. *Planta 206*, 630-640.

Golecki B., Schulz A., Thompson G.A. (1999) Translocation of structural P proteins in the phloem. *Plant Cell 11*, 127-140.

Gong H., Peng Y., Zou C., Wang D., Xu Z. & Bai S. (2006) A simple treatment to significantly increase signal specificity in immunohistochemistry. *Plant Molecular Biology Reporter 24*, 93-101.

Gould N., Minchin P.E.H. & Thorpe M.R. (2004) Direct measurements of sieve element hydrostatic pressure reveal strong regulation after pathway blockage. *Functional Plant Biology 31*, 987-993.

Gupta A.B. & Sankararamakrishnan R. (2009) Genome-wide analysis of major intrinsic proteins in the tree plant populus trichocarpa: Characterization of XIP subfamily of aquaporins from evolutionary perspective. *BMC Plant Biology 9*, 134.

Gustafsson M.G. (2000) Surpassing the lateral resolution limit by a factor of two using structured illumination microscopy. *J Microsc 198*, 82-87

Gustafsson M.G., Shao L., Carlton P.M., Wang C.J., Golubovskaya I.N., Cande W.Z., Agard D.A., Sedat J.W. (2008) Three-dimensional resolution doubling in wide-field fluorescence microscopy by structured illumination. *Biophysical journal 94*, 4957-4970.

Ham B. & Lucas W.J. (2014) The angiosperm phloem sieve tube system: A role in mediating traits important to modern agriculture. *Journal of Experimental Botany 65*, 1799-1816.

Hao P., Liu C., Wang Y., Chen R., Tang M., Du B., Zhu L. & He G. (2008) Herbivore-induced callose deposition on the sieve plates of rice: An important mechanism for host resistance. *Plant Physiology 146*, 1810-1820.

Hedrich R., Salvador-Recatalà V. & Dreyer I. (2016) Electrical wiring and long-distance plant communication. *Trends in Plant Science 21*, 376-387.

Hölttä T., Mencuccini M. & Nikinmaa E. (2009) Linking phloem function to structure: Analysis with a coupled xylem–phloem transport model. *Journal of Theoretical Biology 259*, 325-337.

Huang B., Bates M., Zhuang X.W. (2009) Super-Resolution Fluorescence Microscopy. *Annual Review of Biochemistry 78*, 993-1016.

Ivashikina N., Deeken R., Ache P., Kranz E., Pommerrenig B., Sauer N., Hedrich R. (2003) Isolation of AtSUC2 promoter-GFP-marked companion cells for patch-clamp studies and expression profiling. *Plant J 36*, 931-945

Jaeger C.H., Goeschl J.D., Magnuson C.E., Fares Y. & Strain B.R. (1988) Short-term responses of phloem transport to mechanical perturbation. *Physiologia Plantarum 72*, 588-594.

Jarsch I.K., Konrad S.S.A., Stratil T.F., Urbanus S.L., Szymanski W., Braun P., Braun K.H., Ott T. (2014) Plasma Membranes Are Subcompartmentalized into a Plethora of Coexisting and Diverse Microdomains in Arabidopsis and Nicotiana benthamiana. *Plant Cell 26*, 1698-1711.

Jensen K.H., Lee J., Bohr T., Bruus H., Holbrook N.M. & Zwieniecki M.A. (2011) Optimality of the münch mechanism for translocation of sugars in plants. *Journal of the Royal Society Interface 8*, 1155-1165.

Jensen K.H., Liesche J., Bohr T. & Schulz A. (2012) Universality of phloem transport in seed plants. *Plant, Cell & Environment 35*, 1065-1076.

Jensen K.H., Mullendore D.L., Holbrook N.M., Bohr T., Knoblauch M. & Bruus H. (2012) Modeling the hydrodynamics of phloem sieve plates. *Frontiers in Plant Science 3*, 151.

Jensen K.H., Rio E., Hansen R., Clanet C. & Bohr T. (2009) Osmotically driven pipe flows and their relation to sugar transport in plants. *Journal of Fluid Mechanics 636*, 371-396.

Julia Kehr & Anja Buhtz. (2008) Long distance transport and movement of RNA through the phloem. *Journal of Experimental Botany 59*, 85-92.

Julia Kehr & Anja Buhtz. (2008) Long distance transport and movement of RNA through the phloem. *Journal of Experimental Botany 59*, 85-92.

Kammerloher W., Fischer U., Piechottka G.P. & Schäffner A.R. (1994) Water channels in the plant plasma membrane cloned by immunoselection from a mammalian expression system. *The Plant Journal 6*, 187-199.

Khan J.A., Wang Q., Sjolund R.D., Schulz A., Thompson G.A. (2007) An early nodulin-like protein accumulates in the sieve element plasma membrane of Arabidopsis. *Plant Physiol 143*, 1576-1589.

Klar T.A., Jakobs S., Dyba M., Egner A., Hell S.W. (2000) Fluorescence microscopy with diffraction resolution barrier broken by stimulated emission. *Proceedings of the National Academy of Sciences 97*, 8206-8210.

Knoblauch M. & Peters W.S. (2010) Münch, morphology, microfluidics - our structural problem with the phloem. *Plant, Cell & Environment 33*, 1439-1452.

Knoblauch M., Froelich D.R., Pickard W.F. & Peters W.S. (2014) SEORious business: Structural proteins in sieve tubes and their involvement in sieve element occlusion. *Journal of Experimental Botany 65*, 1879-1893.

Knoblauch M., Knoblauch J., Mullendore D.L., Savage J.A., Babst B.A., Beecher S.D., Dodgen A.C., Jensen K.H. & Holbrook N.M. (2016) Testing the münch hypothesis of long distance phloem transport in plants. *Elife 5*, e15341.

Kramer P.J. & Boyer J.S. (1995) Water relations of plants and soils. Academic Press, New York.

Lang A. & Minchin P. (1986) Phylogenetic distribution and mechanism of translocation inhibition by chilling. *Journal of Experimental Botany 37*, 389-398.

Larchevêque M., Maurel M., Desrochers A., & Larocque, G. R. (2011). How does drought tolerance compare between two improved hybrids of balsam poplar and an unimproved native species? *Tree Physiology 31*, 240-249.

Laur J. & Hacke U.G. (2013) Transpirational demand affects aquaporin expression in poplar roots. *Journal of Experimental Botany 64*, 2283-2293.

Laur J., Hacke U.G. (2014) Exploring Picea glauca aquaporins in the context of needle water uptake and xylem refilling. *New Phytol 203*, 388-400.

Laur, J., & Hacke, U. G. (2014). The role of water channel proteins in facilitating recovery of leaf hydraulic conductance from water stress in Populus trichocarpa. *PloS one 9*, e111751.

Lee, S. H., & Zwiazek, J. J. (2015). Regulation of aquaporin-mediated water transport in Arabidopsis roots exposed to NaCl. *Plant and Cell Physiology 56*, 750-758.

Lee, S. H., Chung, G. C., Jiang, J. Y., Ahn, S. J., & Zwiazek, J. J. (2012). Overexpression of PIP2; 5 aquaporin alleviates effects of low root temperature on cell hydraulic conductivity and growth in Arabidopsis thaliana. *Plant Physiology 159*, 479-488.

Leineweber K., Schulz A., Thompson G.A. (2000) Dynamic transitions in the translocated phloem filament protein. *Australian Journal of Plant Physiology 27*, 733-741.

Liesche J. & Patrick J. (2017) An update on phloem transport: A simple bulk flow under complex regulation. F1000Research 6.

Liesche J. & Schulz A. (2012) In vivo quantification of cell coupling in plants with different phloem loading strategies. *Plant Physiology 159*, 355-365.

Liesche J., Pace M.R., Xu Q., Li Y. & Chen S. (2017a) Height-related scaling of phloem anatomy and the evolution of sieve element end wall types in woody plants. *New Phytologist 214*, 245-256.

Liesche J., Schulz A. (2018) Phloem transport in gymnosperms: a question of pressure and resistance. *Curr Opin Plant Biol 43*, 36-42.

Lingwood D., Simons K. (2010) Lipid rafts as a membrane-organizing principle. *Science 327*, 46-50.

Livak KJ, Schmittgen TD (2001) Analysis of relative gene expression data using real-time quantitative PCR and the 22DDCT method. *Methods 2*, 402–408.

Lucas W.J., Groover A., Lichtenberger R., Furuta K., Yadav S., Helariutta Y., He X., Fukuda H., Kang J., Brady S.M., Patrick J.W., Sperry J., Yoshida A., López-Millán A., Grusak M.A. & Kachroo P. (2013) The plant vascular system: Evolution, development and Functions *F. Journal of Integrative Plant Biology 55*, 294-388.

Luu D. & Maurel C. (2005) Aquaporins in a challenging environment: Molecular gears for adjusting plant water status. *Plant, Cell & Environment 28*, 85-96.

Marjanović, Ž., Uehlein, N., Kaldenhoff, R., Zwiazek, J. J., Weiß, M., Hampp, R., & Nehls, U. (2005). Aquaporins in poplar: what a difference a symbiont makes! *Planta 222*, 258-268.

Martens H.J., Roberts A.G., Oparka K.J., Schulz A. (2006) Quantification of plasmodesmatal endoplasmic reticulum coupling between sieve elements and companion cells using fluorescence redistribution after photobleaching. *Plant Physiol 142*, 471-480.

Maule, A. J., Benitez-Alfonso, Y., & Faulkner, C. (2011). Plasmodesmata–membrane tunnels with attitude. *Current Opinion in Plant Biology 14*, 683-690.

Maurel C., Boursiac Y., Luu D., Santoni V., Shahzad Z. & Verdoucq L. (2015) Aquaporins in plants. *Physiological Reviews 95*, 1321-58.

Maurel C., Javot H., Lauvergeat V., Gerbeau P., Tournaire C., Santoni V. & Heyes J. (2002) Molecular physiology of aquaporins in plants. In: International Review of Cytology, Molecular physiology of aquaporins in plants. pp. 105-148. Elsevier Science & Technology, United States.

Maurel C., Lionel Verdoucq, Doan-Trung Luu & Véronique Santoni. (2008) Plant aquaporins: Membrane channels with multiple integrated functions. *Annual Review of Plant Biology 59*, 595-624.

Maurel C., Reizer J., Schroeder J.I. & Chrispeels M.J. (1993) The vacuolar membrane protein gamma-TIP creates water specific channels in Xenopus oocytes. *The EMBO Journal 12*, 2241-2247.

Maurel C., Verdoucq L. & Rodrigues O. (2016) Aquaporins and plant transpiration. *Plant, Cell & Environment 39*, 2580-2587.

McDowell N., Pockman W. T., Allen C. D., Breshears D. D., Cobb N., Kolb T. & Yepez E. A. (2008). Mechanisms of plant survival and mortality during drought: why do some plants survive while others succumb to drought? *New phytologist 178*, 719-739.

McNairn R.B. (1972) Phloem translocation and heat-induced callose formation in field-grown gossypium hirsutum L. *Plant Physiology 50*, 366-370.

Milburn J.A. (1974) Phloem transport in ricinus: Concentration gradients between source and sink. *Planta 117*, 303-319.

Minchin P. & Thorpe M.R. (1983) A rate of cooling response in phloem translocation. *Journal of Experimental Botany 34*, 529-536.

Minchin P. & Thorpe M.R. (1987) Measurement of unloading and reloading of photo-assimilate within the stem of bean. *Journal of Experimental Botany 38*, 211-220.

Mittler T.E. (1953) Amino-acids in phloem sap and their excretion by aphids. *Nature 172*, 207.

Moran P.J., Cheng Y., Cassell J.L. & Thompson G.A. (2002) Gene expression profiling of Arabidopsis thaliana in compatible plant-aphid interactions. *Archives of Insect Biochemistry and Physiology 51*, 182-203.

Mori I.C., Rhee J., Shibasaka M., Sasano S., Kaneko T., Horie T. & Katsuhara M. (2014) CO2 transport by PIP2 aquaporins of barley. *Plant & Cell Physiology 55*, 251-257.

Muday G.K. & Brown-Harding H. (2018) Nervous system-like signaling in plant defense. *Science 361*, 1068-1069.

Mullendore D. L., Ross-Elliott T., Liu Y., Hellmann H. H., Roalson E. H., Peters W. S., & Knoblauch M. (2018). Non-dispersive phloem-protein bodies (NPBs) of Populus trichocarpa consist of a SEOR protein and do not respond to cell wounding and Ca2+. *PeerJ 6*, e4665.

Mullendore D.L., Windt C.W., Van As H. & Knoblauch M. (2010) Sieve tube geometry in relation to phloem flow. *The Plant Cell 22*, 579-593.

Münch E. (1927) Versuche über den Saftkreislauf. Berichte der Deutschen Botanischen Gesellschaft 45: 340-356.

Münch E. (1930) Die stoffbewegungen in der pflanze. Gustav Fischer Verlagsb.Jena, Germany 234.

Munson B.R., Young D.F., Okiishi T.H. & Heubsch W.W. (1990) Viscous flow in pipes. In: Fundamentals of Fluid Mechanics. pp- 504-517.

Nobel, P. S. (2009). Physicochemical & environmental plant physiology. Academic press, New York. p. 481.

Pavy N, Boyle B, Nelson C, Paule C, Gigue`re I, et al. (2000) Identification of conserved core xylem gene sets: conifer cDNA microarray development, transcript profiling and computational analyses. *New Phytol 180*, 766–86.

Payyavula R.S., Tay K.H.C., Tsai C. & Harding S.A. (2011) The sucrose transporter family in populus: The importance of a tonoplast PtaSUT4 to biomass and carbon partitioning. *The Plant Journal 65*, 757-770.

Peterson E. B., & Peterson N. M. (1992). Ecology, management, and use of aspen and balsam poplar in the prairie provinces. Northwest Region, Northern Forestry Centre, Edmonton, Alberta, Canada: Forestry Canada.

Phillips R.J. & Dungan S.R. (1993) Asymptotic analysis of flow in sieve tubes with semi-permeable walls. *Journal of Theoretical Biology 162*, 465-485.

Pickard W.F. & Minchin P. (1990) The transient inhibition of phloem translocation in phaseolus vulgaris by abrupt temperature drops, vibration, and electric shock. *Journal of Experimental Botany 41*, 1361-1369.

Pickard W.F. & Minchin P. (1990) The transient inhibition of phloem translocation in phaseolus vulgaris by abrupt temperature drops, vibration, and electric shock. Journal of Experimental Botany 41, 1361-1369.

Raffaele S., Mongrand S., Gamas P., Niebel A., Ott T. (2007) Genome-wide annotation of remorins, a plant-specific protein family: Evolutionary and functional perspectives. *Plant Physiol 145*, 593-600.

Rennie E.A. & Turgeon R. (2009) A comprehensive picture of phloem loading strategies. *Proceedings of the National Academy of Sciences 106*, 14162-14167.

Rockwell F.E., Gersony J.T. & Holbrook N.M. (2018) Where does münch flow begin? sucrose transport in the pre-phloem path. *Current Opinion in Plant Biology 43*, 101-107.

Ross-Elliott T.J., Jensen K.H., Haaning K.S., Wager B.M., Knoblauch J., Howell A.H., Mullendore D.L., Monteith A.G., Paultre D. & Yan D. (2017) Phloem unloading in arabidopsis roots is convective and regulated by the phloem-pole pericycle. *Elife 6*, e24125.

Russin W.A. & Evert R.F. (1985) Studies on the leaf of populus deltoides (salicaceae): Quantitative aspects, and solute concentrations of the sieve-tube members. *American Journal of Botany 72*, 487-500.

Ryan M.G. & Asao S. (2014) Phloem transport in trees. *Tree Physiology 34*, 1-4.

Sack L., Streeter C.M. & Holbrook N.M. (2004) Hydraulic analysis of water flow through leaves of sugar maple and red oak. *Plant Physiology 134*, 1824-1833.

Sade N., Shatil-Cohen A., Attia Z., Maurel C., Boursiac Y., Kelly G., Granot D., Yaaran A., Lerner S. & Moshelion M. (2014) The role of plasma membrane aquaporins in regulating the bundle sheath-mesophyll continuum and leaf hydraulics. *Plant Physiology 166*, 1609-1620.

Sasaki T., Chino M., Hayashi H. & Fujiwara T. (1998) Detection of several mRNA species in rice phloem sap. *Plant & Cell Physiology 39*, 895-897.

Savage J.A., Beecher S.D., Clerx L., Gersony J.T., Knoblauch J., Losada J.M., Jensen K.H., Knoblauch M. & Holbrook N.M. (2017) Maintenance of carbohydrate transport in tall trees. *Nature Plants 3*, 965.

Schermelleh L., Carlton P.M., Haase S., Shao L., Winoto L., Kner P., Burke B., Cardoso M.C., Agard D.A., Gustafsson M.G.L., Leonhardt H., Sedat J.W. (2008) Subdiffraction multicolor imaging of the nuclear periphery with 3D structured illumination microscopy. *Science 320*, 1332-1336.

Schermelleh L., Heintzmann R., Leonhardt H. (2010) A guide to super-resolution fluorescence microscopy. *The Journal of cell biology 190*, 165-175.

Schulte P.J. (2012) Computational fluid dynamics models of conifer bordered pits show how pit structure affects flow. *New Phytologist 193*, 721-729.

Schulte P.J., Hacke U.G. & Schoonmaker A.L. (2015) Pit membrane structure is highly variable and accounts for a major resistance to water flow through tracheid pits in stems and roots of two boreal conifer species. *New Phytologist 208*, 102-113.

Schulz A. (1986) Wound phloem in transition to bundle phloem in primary roots of Pisum sativum L. .1. Development of bundle-leaving wound-sieve tubes. *Protoplasma 130*, 12-26.

Schulz A. (2015) Diffusion or bulk flow: How plasmodesmata facilitate pre-phloem transport of assimilates. *Journal of Plant Research 128*, 49-61.

Sevanto S. (2014) Phloem transport and drought. *Journal of Experimental Botany 65*, 1751-1759.

Sevanto S. (2018) Drought impacts on phloem transport. *Current Opinion in Plant Biology 43*, 76-81.

Sevanto S., McDowell N.G., Dickman L.T., Pangle R. & Pockman W.T. (2014) How do trees die? A test of the hydraulic failure and carbon starvation hypotheses. *Plant, Cell & Environment 37*, 153-161.

Sibaoka T. (1962) Excitable cells in mimosa. *Science 137*, 226.

Sperry J.S., Adler F.R., Campbell G.S. & Comstock J.P. (1998) Limitation of plant water use by rhizosphere and xylem conductance: Results from a model. *Plant, Cell & Environment 21*, 347-359.

Stanfield R.C., Hacke U.G. & Laur J. (2017) Are phloem sieve tubes leaky conduits supported by numerous aquaporins? *American Journal of Botany 104*, 719-732.

Stanfield, R. C., Schulte, P. J., Randolph, K. E., & Hacke, U. G. (2018). Computational models evaluating the impact of sieve plates and radial water exchange on phloem pressure gradients. *Plant, cell & environment*. https://doi.org/10.1111/pce.13414.

Thompson M.V. & Holbrook N.M. (2003a) Application of a single-solute non-steady-state phloem model to the study of long-distance assimilate transport. *Journal of Theoretical Biology 220*, 419-455.

Thompson M.V. & Holbrook N.M. (2003b) Scaling phloem transport: Water potential equilibrium and osmoregulatory flow. *Plant, Cell & Environment 26*, 1561-1577.

Thompson M.V. (2006) Phloem: The long and the short of it. *Trends in Plant Science 11*, 26-32.

Thorpe M.R., Furch A.C., Minchin P.E., Foeller J., Van Bel A.J. & Hafke J.B. (2010) Rapid cooling triggers forisome dispersion just before phloem transport stops. P*lant, Cell & Environment 33*, 259-271.

Tjallingii W.F. & Hogen Esch T. (1993) Fine structure of aphid stylet routes in plant tissues in correlation with EPG signals. *Physiological Entomology 18*, 317-328.

Tomos A.D. & Leigh R.A. (1999) The pressure probe: A versatile tool in plant cell physiology. Annual Review of Plant Biology 50, 447-472.

Törnroth-Horsefield S., Wang Y., Hedfalk K., Johanson U., Karlsson M., Tajkhorshid E., Neutze R. & Kjellbom P. (2006) Structural mechanism of plant aquaporin gating. *Nature 439*, 688.

Truernit E. (2014) Phloem imaging. *Journal of Experimental Botany 65*, 1681-1688.

Turgeon R. (2010) The puzzle of phloem pressure. *Plant Physiology 154*, 578-581.

Turgeon, R., & Hepler, P. K. (1989). Symplastic continuity between mesophyll and companion cells in minor veins of mature Cucurbita pepo L. leaves. *Planta 179*, 24-31.

Tyree M.T. & Dainty J. (1975) Theoretical considerations. In Transport in Plants I Theoretical considerations. pp. 367-392. Springer.

Tyree M.T. & Ewers F.W. (1991) The hydraulic architecture of trees and other woody plants. *New Phytologist 119*, 345-360.

Uehlein N., Otto B., Hanson D.T., Fischer M., McDowell N. & Kaldenhoff R. (2008) Function of nicotiana tabacum aquaporins as chloroplast gas pores challenges the concept of membrane CO2 permeability. *The Plant Cell 20*, 648-657.

van Bel A. (2003) The phloem, a miracle of ingenuity. *Plant, Cell & Environment 26*, 125-149.

van Bel A.J. & Knoblauch M. (2000) Sieve element and companion cell: The story of the comatose patient and the hyperactive nurse. *Functional Plant Biology 27*, 477-487.

van Bel A.J.E. (2019) Sieve Elements: The Favourite Habitat of Phytoplasmas. In: Musetti R., Pagliari L. (eds) Phytoplasmas. Methods in Molecular Biology, vol 1875. Humana Press, New York, NY.

van Bel A.J.E., Knoblauch M. (2000) Sieve element and companion cell: the story of the comatose patient and the hyperactive nurse. *Australian Journal of Plant Physiology 27*, 477-487.

Verdoucq L., Rodrigues O., Martinière A., Luu D.T. & Maurel C. (2014) Plant aquaporins on the move: Reversible phosphorylation, lateral motion and cycling. *Current Opinion in Plant Biology 22*, 101-107.

Walz C., Juenger M., Schad M. & Kehr J. (2002) Evidence for the presence and activity of a complete antioxidant defence system in mature sieve tubes. *The Plant Journal 31*, 189-197.

Wilkins, O., Nahal, H., Foong, J., Provart, N. J., & Campbell, M. M. (2009). Expansion and diversification of the Populus R2R3-MYB family of transcription factors. *Plant Physiology 149*, 981-993.

Windt C.W., Vergeldt F.J., Jager d., P.A & As v., H. (2006) MRI of long-distance water transport: A comparison of the phloem and xylem flow characteristics and dynamics in poplar, castor bean, tomato and tobacco. *Plant, Cell & Environment 29*, 1715-1729.

Yaneff, A., Vitali, V., & Amodeo, G. (2015). PIP1 aquaporins: Intrinsic water channels or PIP2 aquaporin modulators? *FEBS letters 589*, 3508-3515.

Young D.F., Munson B.R., Okiishi T.H. & Huebsch W.W. (2010) A brief introduction to fluid mechanics. John Wiley & Sons.

Zhang C., Lu Han, Thomas L. Slewinski, Jianlei Sun, Jing Zhang, Zeng-Yu Wang & Robert Turgeon. (2014) Symplastic phloem loading in poplar. *Plant Physiology 166*, 306-313.

Zhao C., Shao H. & Chu L. (2008) Aquaporin structure–function relationships: Water flow through plant living cells. Colloids and Surfaces B: *Biointerfaces 62*, 163-172.

Ziomkiewicz I., Sporring J., Pomorski T.G., Schulz A. (2015) Novel approach to measure the size of plasma-membrane nanodomains in single molecule localization microscopy. Cytometry Part A 87A, 868-877.

Zwiazek J.J., Xu H., Tan X., Navarro-Ródenas A. & Morte A. (2017) Significance of oxygen transport through aquaporins. *Scientific Reports 7*, 40411.

Appendices

Appendix 2-1: Amino acid multiple sequence alignment of the primary antibody targeted sequences used in this study of the PIP aquaporins. (A) Alignment of the N-terminal region of AtPIP1;3 and *Populus trichocarpa* PIP1s; (B) the alignment of the conserved C-terminal region of *Populus trichocarpa* PIP2s. Shading is indicative of the degree of amino-acid conservation at a specific position (black = identity, grey = similarity).

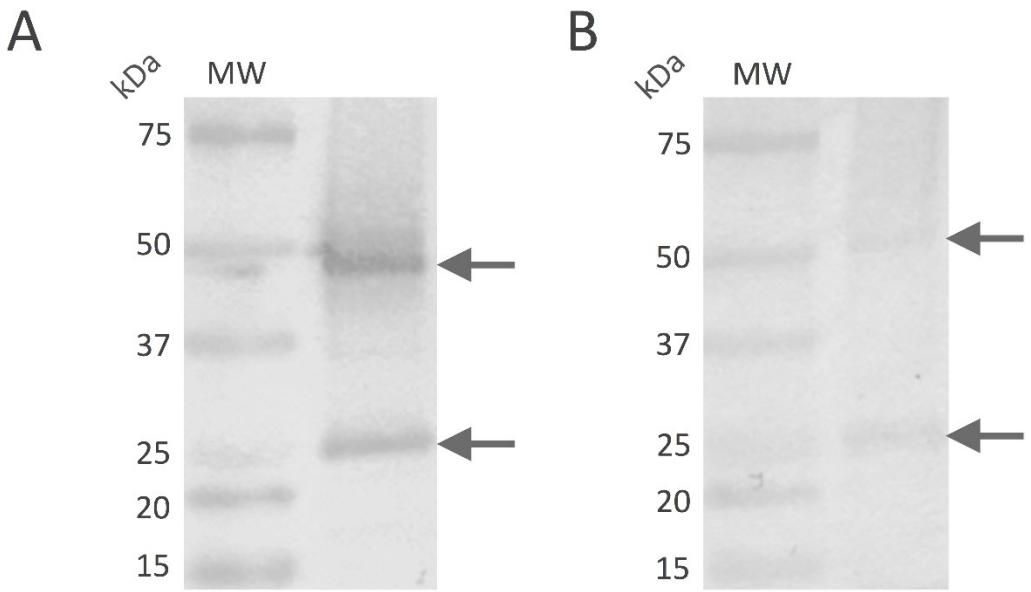

Appendix 2-2: Binding specificity of anti-aquaporin antibodies. Balsam poplar shoot microsomal membrane proteins were subjected to immunoblotting using (A) affinity purified anti-PIP1 antibodies and (B) anti-PIP2 antiserum. The first lane shows standard molecular weight markers in kDa. Arrows indicate targeted monomeric (≈ 25kDa) and dimeric (≈ 50kDa) forms of each aquaporin subfamily.

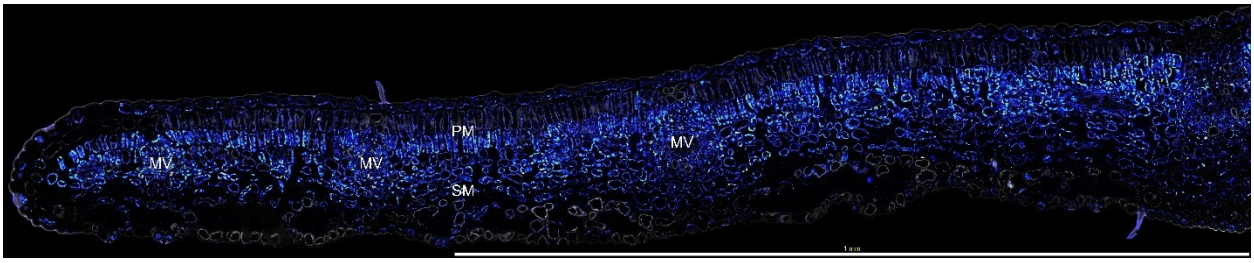

Appendix 2-3: A composite image of over 50 smaller images stitched together using confocal laser scanning micrographs. The image represents approximately one-half of an immature leaf lamina from balsam poplar. Immunolabeling was performed using PIP1 antibody. A distinct labeling pattern in the palisade mesophyll (PM) is shown, whereby the upper layer remains largely unlabeled, while the lower layer is consistently labeled (predominantly in chloroplasts). Symbols: MV = minor vein, SM = Spongy Mesophyll.

Appendix 2-4: The median diameters and interquartile range (IQR) of sieve elements of balsam poplar in different organs. Median lengths and IQR of sieve elements from select organs are also displayed. SE = sieve elements, all units in µm.

Organ	SE Diameter			SE Length		
	Median	IQR	*N*	Median	IQR	*N*
Root	8.91	7.80 – 10.30	37	-	-	-
Stem	7.82	6.65 – 9.29	322	110.91	89.70 – 132.18	90
Petiole	3.94	3.14 – 4.99	1051	-	-	-
Mid Vein	4.23	3.54 – 5.24	832	-	-	-
Minor Vein	2.80	2.03 – 3.33	77	32.02	23.92 – 47.63	14

N, total number of sieve elements measured for each organ.

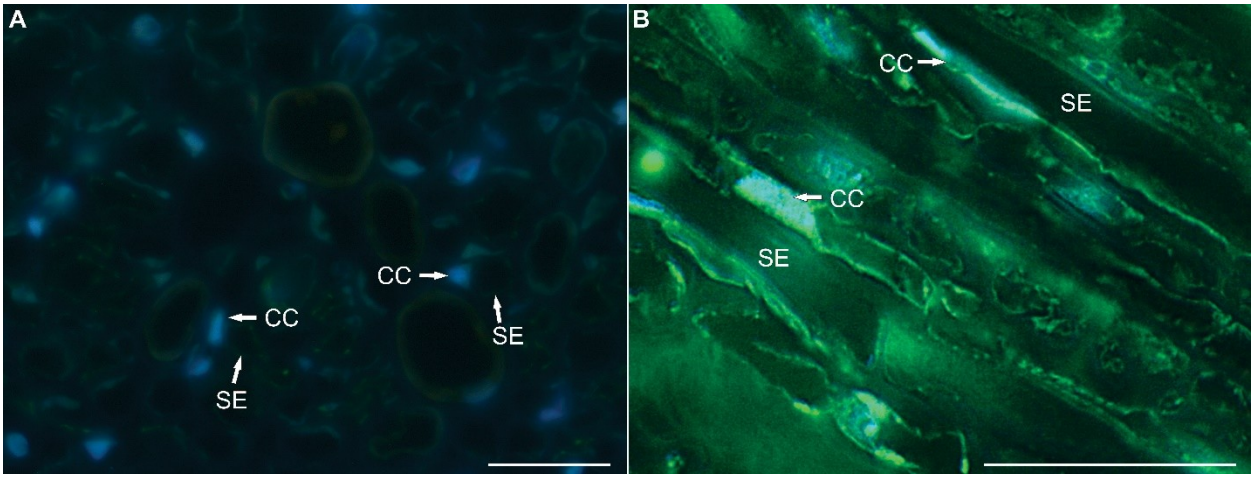

Appendix 2-5: Fluorescence micrograph (A) showing a transverse section of a stem and (B) a confocal laser scanning micrograph of a stem longitudinal section of the phloem of balsam poplar. Nuclei were stained with DAPI (light blue). Symbols: CC = companion cell, SE = sieve element. Bar = 20µm.

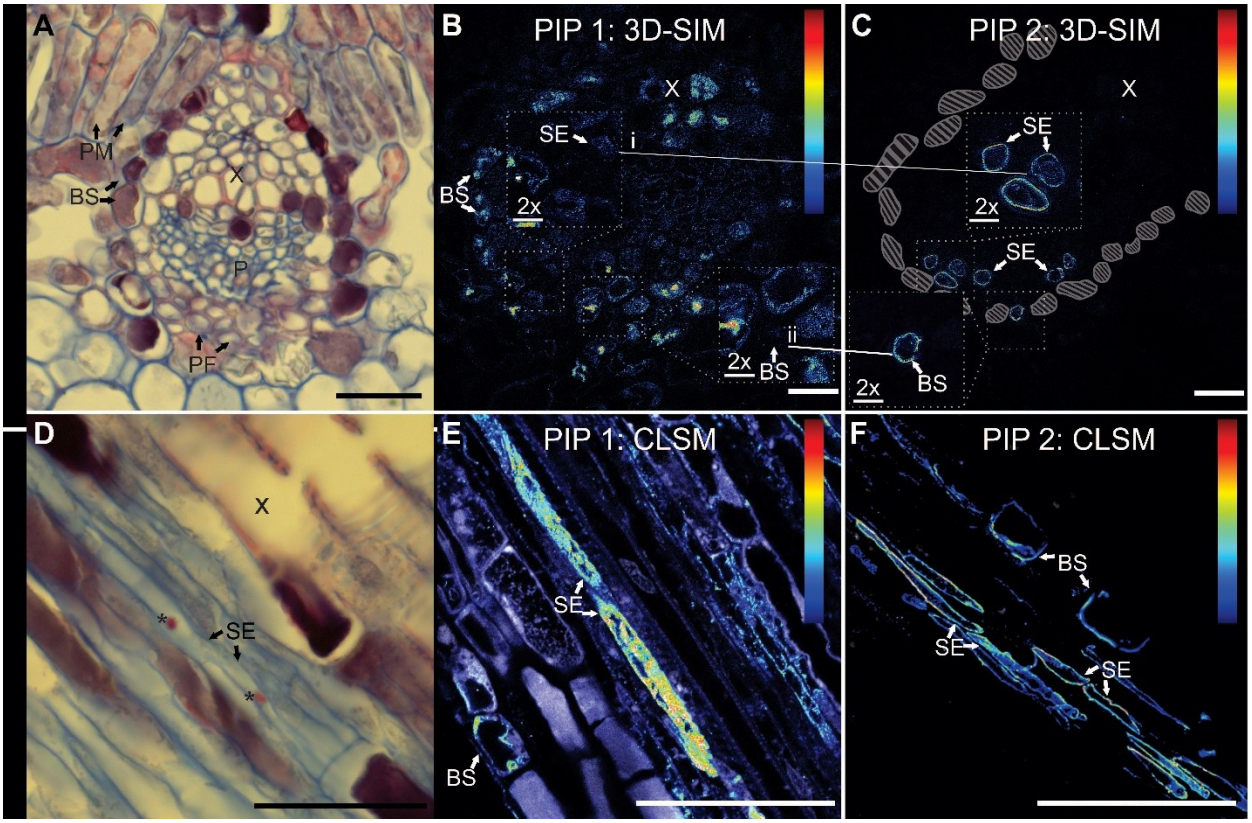

Appendix 2-6: Minor leaf veins of balsam poplar. (A) Micrograph showing aniline blue-stained phloem and safranin-stained xylem in brightfield. (B) Micrograph using 3D-Structured Illumination Microscopy (3D-SIM) showing PIP1 antibody labeling. (C) Same section as (B) but with PIP2 labeling in six sieve elements and a single bundle sheath cell membrane; lines point to the same exact cell and shaded cell outlines correspond to the bundle sheath visible in (B). (D) Micrograph of aniline blue-stained phloem in brightfield. (E) Micrograph using confocal laser scanning microscopy (CLSM) with PIP1 labeling in the lumen of two sieve elements. (F) Section using CLSM showing PIP2 labeling predominantly in plasma membranes of sieve elements and bundle sheath cells. Asterisks correspond to safranin-stained sieve element agglomerations. For florescent images, colors closer to red on the scale represent greater fluorescent intensity. Symbols: BS = bundle sheath, P = phloem, PM = palisade mesophyll, PF = phloem fibers, SE = sieve element, X = xylem. Bar = (A) 25µm, (B, C) 10µm, (D) 30µm, (E, F) 25µm. Square boxes in (B - C) represent 100% enlargements, with an inset scale bar = 3µm

Appendix 2-7: Contingency table showing the raw counts of sieve elements of balsam poplar with PIP1 in internalized membrane (IM) or plasma membrane (PM) distribution for different petioles sampled in each time period. In addition, the ratio of IM:PM labeling is included for each time period.

	Petiole ID				Total
7:30h	Petiole 1	Petiole 16	Petiole 17	Petiole 21	
IM	49	68	91	51	259
PM	200	176	359	246	981
Ratio	0.25	0.39	0.25	0.21	$\bar{X} = 0.26$
15:30h	Petiole 2	Petiole 3	Petiole 4	Petiole 11	
IM	19	37	163	20	239
PM	66	256	306	174	802
Ratio	0.29	0.14	0.53	0.11	$\bar{X} = 0.30$
24:00h	Petiole 10	Petiole 14	Petiole 6	Petiole 20	
IM	48	31	39	40	158
PM	310	131	171	455	1067
Ratio	0.15	0.24	0.23	0.09	$\bar{X} = 0.15$

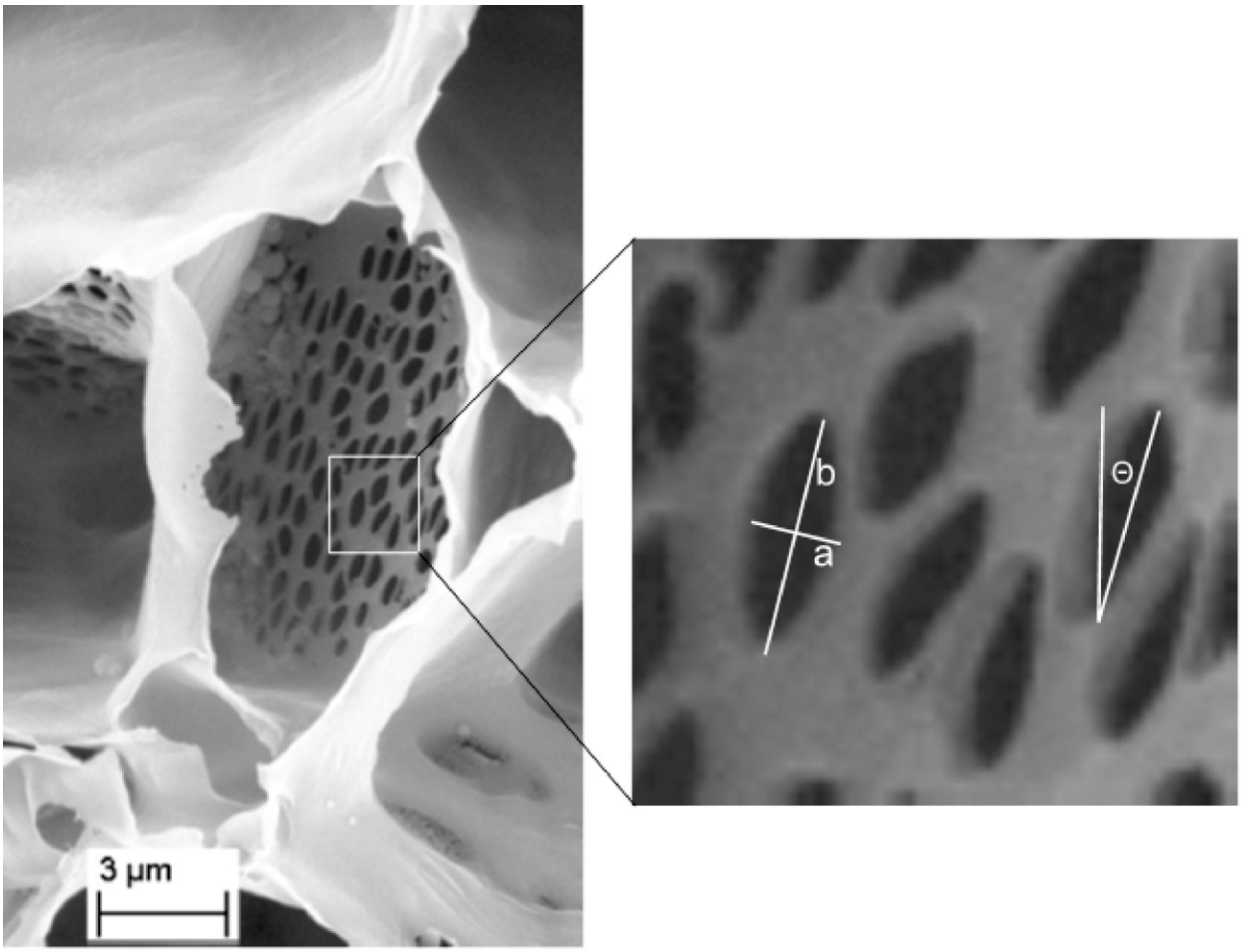

Appendix 4-1: The correction process used for sieve plates pores which occurred at angles in relation to sieve tube sieve walls. (a) Example of pores found at an angle relative to side walls, and the measurements taken to correct for this skew. From the pore dimensions a and b, ϕ is calculated which is the required angle of change needed for pores to appear face-on. (b) Once ϕ was calculated, the sieve plate was copied onto from the original to the corrected plane. This corrected plate and associated pores were then ready for fluid modeling.

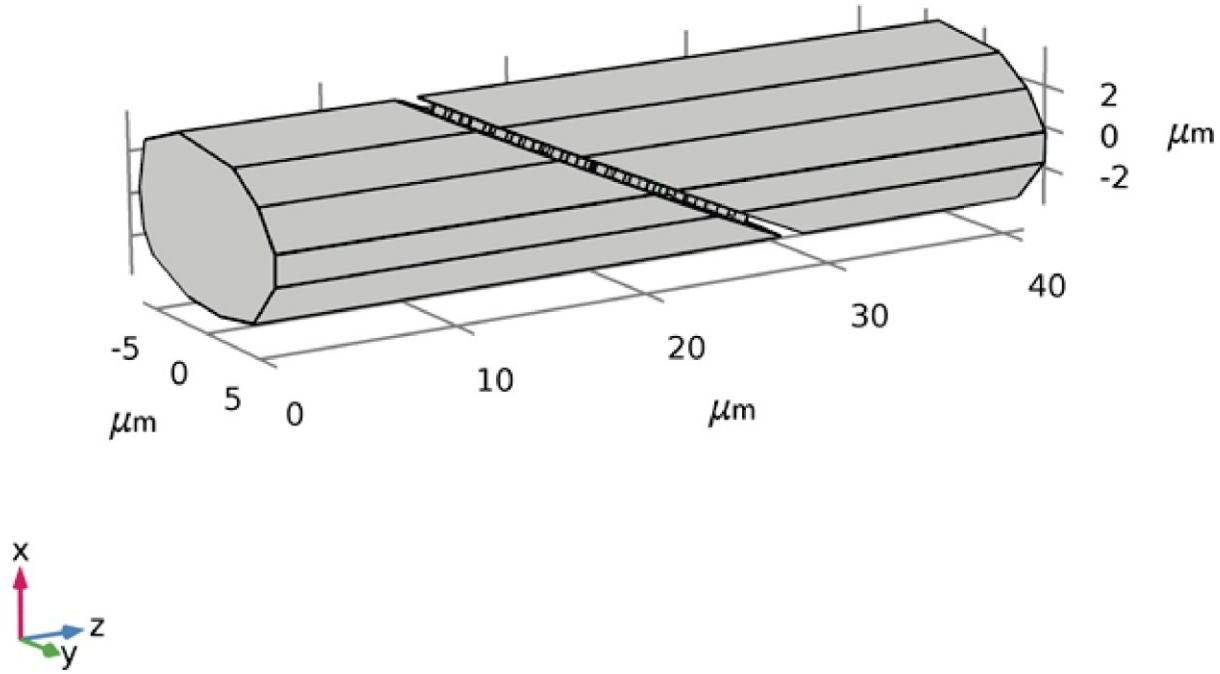

Appendix 4-2: Example of a sieve plate with pores corrected for angle and imported into the 3D model.

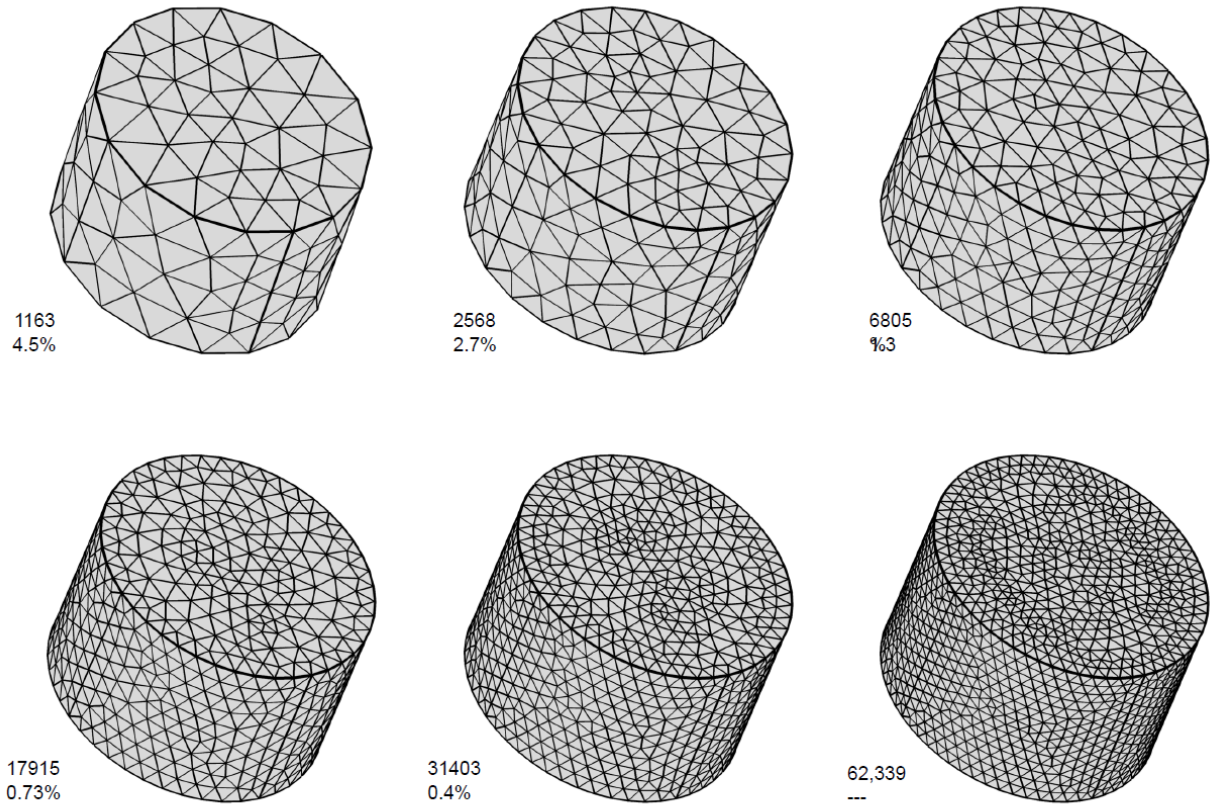

Appendix 4-3: Changes in the finite element mesh density (element sizes) were used to determine the adequacy of the mesh. Shown are the tetrahedral element meshes for one pore of the 93 present in the sieve plate of one particular model. Numbers to the lower left of each version show the total number of mesh elements for the pore pictured and the percent change in total model pressure drop (inlet pressure minus outlet pressure) as compared to the mesh with the finest elements at the lower right. The total number of elements for all of the sieve plate pores and the rest of the model ranged from about 2 – 13 million over the range of densities shown above. For scale, the above pore was 0.49 μm in height and elliptical in cross-section with a major axis of 0.8132 μm.

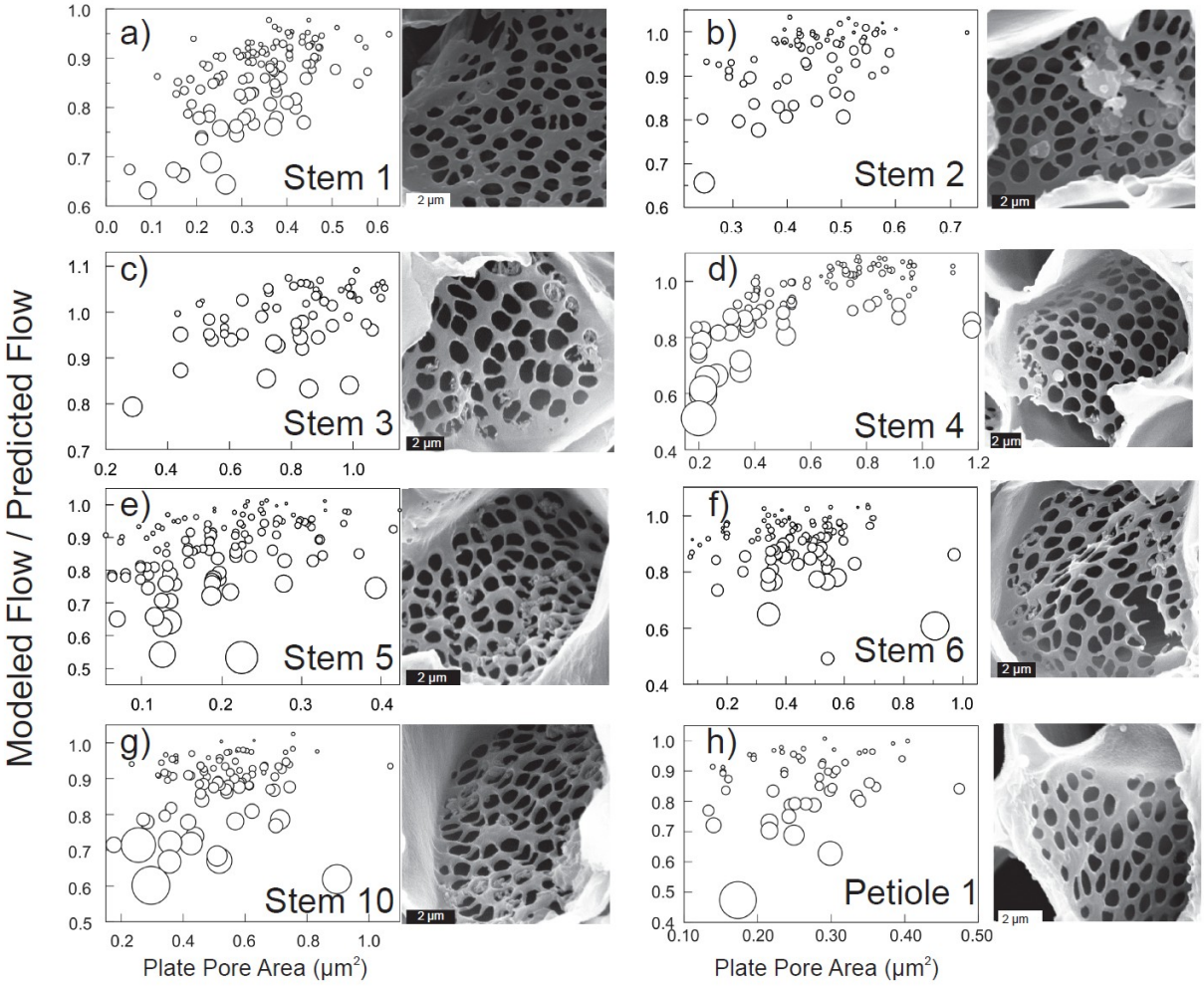

Appendix 4-4: Pore shape as a function of pore area for 8 examples of imaged sieve plates. Example plates are from stem (A-G) or petiole tissue (H). The x-axes shows individual pore area. The y-axes show the ratio between the modeled flow using the shape provided by the SEM image to the predicted flow assuming that pore were perfectly round. Larger circles on the graph represent pores with shapes that are more oblong. The label for each graph (e.g., Stem 1, Stem 2, Stem 3, etc.) correspond to the plate IDs shown in Table 2.

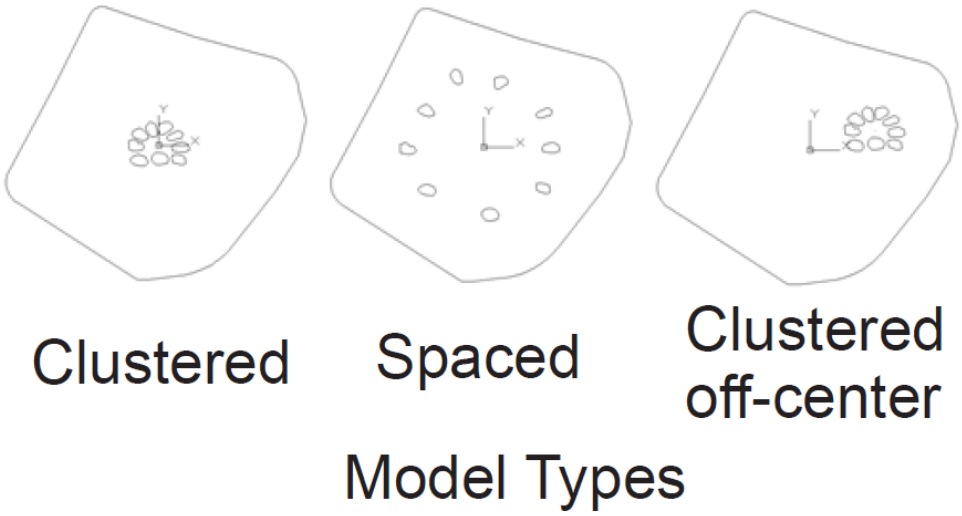

Appendix 4-5: Examples of three different sieve plates used in models to assess the impact of pore spacing on flow. In these models, representative pore shapes were used based upon SEM images.

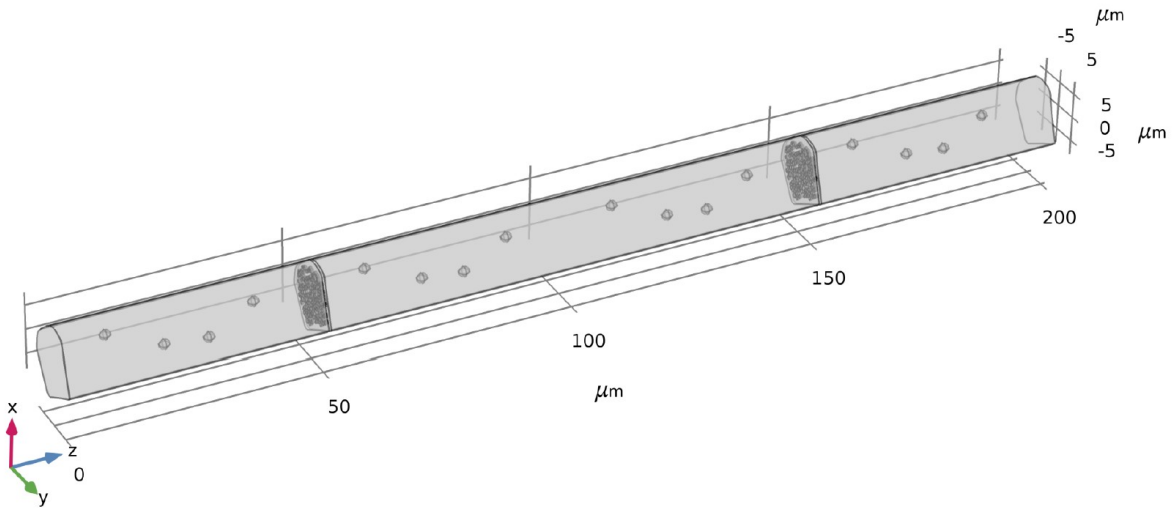

Appendix 4-6: A three cell model with 2 μm spherical obstructions within the lumen.